Electron Correlation Effects in Low Dimensional Periodic Systems

by

TOMOTOSHI NISHINO
DEPARTMENT OF PHYSICS
FACULTY OF SCIENCE
OSAKA UNIVERSITY
— — — — — —
TOYONAKA
OSAKA
560
JAPAN

— Abstract —

Short range electron correlation effects in one- and two-dimensional periodic systems are studied. The electronic structure of CuO_2 plane of the High-Tc compounds is chiefly examined by regarding the plane as a network of Cu-$3d$ orbitals via oxygen-$2p$ ones. The valence band structure of this network is outside the scope of the one-body theory because of the strong Coulomb interaction in Cu-$3d$; there is a competition between the band energy and the local Coulomb energy. The author has investigated many-body effects in the CuO_2 plane by reconstructing a finite size system into a computer, and by directly diagonalizing the Hamiltonian via the Lanczos method. Ground state properties, such as the hole/electron occupation and the spin correlation between atoms, are evaluated by using the ground state wave function that is obtained numerically. One particle excitation spectrum from the ground state is also examined through the recursion method. As a result, core and valence band X-ray photo excitation spectra are modified by the relaxation of the valence holes. Finally, the charge excitation gap, which is the opening between the one-particle removal and additional spectrum, is calculated by taking a derivative of the ground state energy with respect to the particle number in the system. Effects of inter-atomic Coulomb repulsion on the gap are mainly examined for the one-dimensional d-p and the extended Hubbard models. Details of the numerical methods and the systematic way of data analyses are also reported.

Contents

Chapter I
Introduction

§1.1 Historical Background of the Problems Discussed in the Present Thesis

In the present thesis the author discusses the electronic states of low dimensional periodic systems, focusing attention on the correlation effects. The author attacks the problems by numerical studies of the model Hamiltonians for systems consisting of finite lattice sites with the periodic boundary condition. The methods of the calculations are the exact diagonalization of the Hamiltonian matrix by use of the Lanczos method and the calculation of the Green function by the recursion method which are explained in detail in chapter II. The calculations carried out by the present author represent a frontier of the researches along the line mentioned above, promoting them to a feasibility limit and exploring new aspects of various problems. This section gives a brief discussion of the historical backgrounds of the problems discussed in the present thesis.

The conduction property of transition metal oxides, such as CuO, NiO, CoO, etc., has been a focal point in solid state physics during the past several decades.[1,2] A transition metal atom in these materials is surrounded by several oxygen atoms, and has an incomplete $3d$ shell. The network of these $3d$ orbitals via oxygen $2p$ orbitals makes a valence band, and it can carry current, while some of these materials have finite charge excitation gap and insulating at room temperature. The one-body theory has not been successful very much for these insulators. It failed to explain finite charge excitation gap in the middle of the valence band, since the $3d$ shell is open.[3,4] Thus, the insulating nature of these materials has been a riddle for long years. In fact, a precise treatment of the electron correlation, which comes from the strong intra-atomic Coulomb interaction in $3d$ orbitals, is indispensable to analyze these materials.

Mott[1,5] first discussed a non-perturbative effect of Coulomb interaction in narrow bands. He suggested that when the band width is sufficiently small, electrons and holes in the valence band bind each other, and they do not carry any current at all; a finite charge

excitation gap that originates the binding energy appears, and the system is insulating. Hubbard[6] reformulated the Mott's scheme by using the Green function technique,[7] which were originally introduced to explain ferromagnetism in $3d$ metals.[8-11] He considered the Coulomb repulsion U in Wannier functions that have $3d$ character, and its effect on the valence band. He showed that the half-filled band is insulating if the repulsion U exceeds the band width W. Today, the charge excitation gap in the highly correlated single band at half-filling is called the 'Mott-Hubbard gap' after them.

Relevance of oxygen $2p$ orbitals to the gap was first pointed out by Zaanen, Sawatzky and Allen.[12] They have calculated the charge excitation gap of transition metal oxides as a function of the intra-atomic Coulomb interaction U in the $3d$ orbitals and the energy difference Δ between the $3d$ orbitals and oxygen $2p$ orbitals. They also calculated the X-ray photo-electron spectra of these materials through the analyses on MO_n (M = Cu, Ni, Co, etc.) cluster,[13] and compared the theoretical result with their experimental results. They concluded that the charge excitation gap of the half-filled band is always smaller than both U and Δ. They divided the (insulating) transition metal oxides into two groups whether U or Δ is relevant to the gap: one is the traditional Mott-Hubbard insulator when $\Delta > U$, and the other is the so-called 'charge transfer (type) insulator' when $U > \Delta$.

The discovery of the high-Tc superconductors cast new lights upon the transition metal oxides. In 1986, Bednorz and Müller[14] found out a kind of copper oxide — $Ba_2La_{2-x}CuO_{4-y}$ — which shows the superconductivity at $x = 0.15$ below $Tc = 38K$. Many related materials have been found in the following several years. Some of them have the transition temperature higher than the boiling point of liquid nitrogen, such as $YBa_2Cu_3O_{7-\delta}$ and $Bi_2Sr_2Ca_nCu_{1+n}O_{6+2n}$.[15,16] These materials are different from the transition metal oxides thus far known at least in the following three points:

(i) They show superconductivity.

(ii) The valence band is two dimensional in atomic level. These materials have the two dimensional structure, the so called 'CuO_2 plane';[17] copper atoms make a square lattice approximately and oxygen atoms are at the mid-points of Cu-Cu lines.(Fig.1) The valence electrons itinerate among Cu-$3d$ orbitals via oxygen-$2p$ orbitals in the plane.

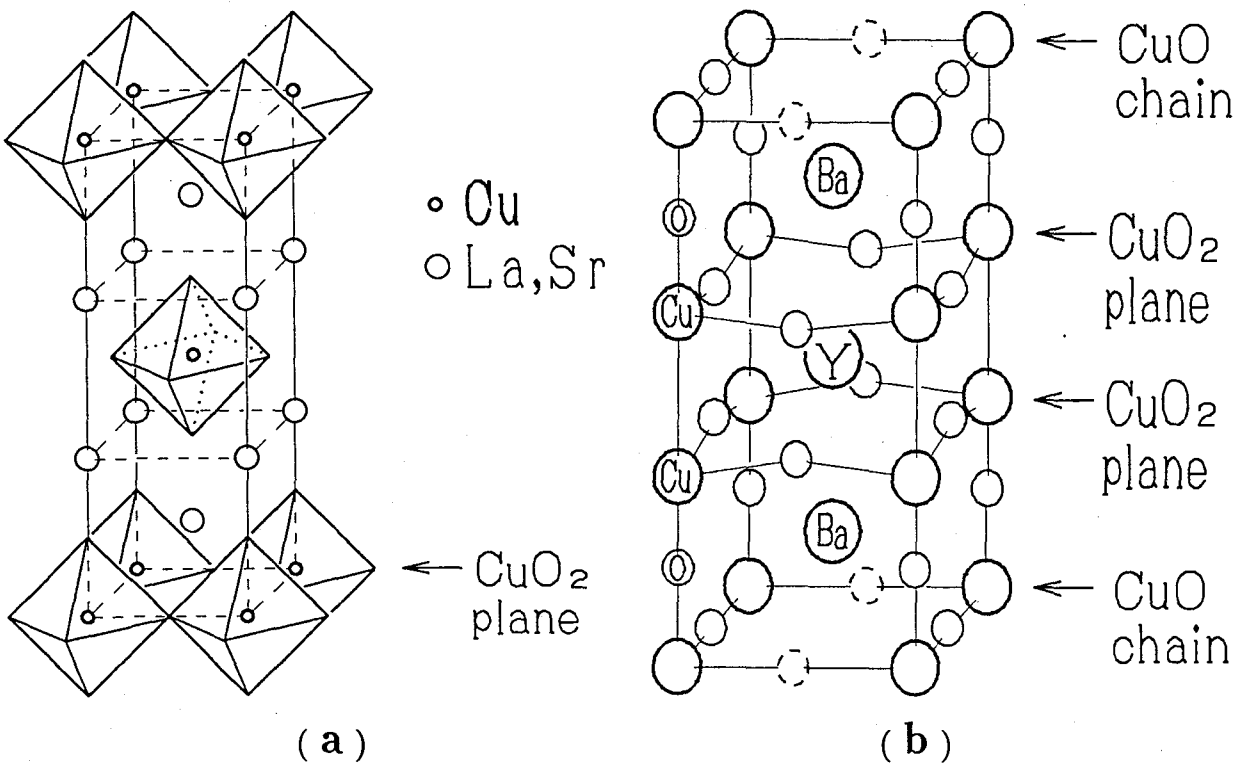

Fig. 1.1 Lattice structure of the high-Tc materials:
(**a**) Unit cell of the $Ba_2La_{2-x}CuO_{4-y}$. (**b**) That of the $YBa_2Cu_3O_{7-\delta}$.
Both of them have the characteristic structure, so called the 'CuO_2 plane'.

(iii) They are non-stoichiometric compounds. The number of carriers (holes) in their valence band is nothing to do with the number of Cu atoms on the plane. The carrier density can be changed in a wide range.

The transition temperature Tc is very sensitive to their composition. Thus, they started investigations on the electronic structure of the high-Tc materials and related transition metal oxides for various electron densities.

A number of theories have been proposed to explain the high-temperature superconductivity. Anderson[18,19] regarded the CuO_2 plane as the two dimensional Hubbard model and discussed the possibility of superconductivity away from half-filling. It was the first attempt to attribute the attractive interaction between carriers to the Coulomb repulsion in narrow band. On the other hand, Emery[20] proposed a more primitive conduction model comprized by $Cu-3d$ and in plane $O-2p$ orbitals. The model is known as the '*d-p* model' today. He insisted that the excess carriers (holes) mainly exist in oxygen $2p$ orbitals

and interact via local spin fluctuation on Cu site. The d-p model is now widely used as a starting point of many other conduction models.[21] Zhang and Rice[22] have obtained an effective Hamiltonian for CuO_2 plane on the basis of the d-p model. They suggested that the excess holes enter oxygen $2p$ orbitals to form local singlet with Cu spins, and moves through the lattice in a similar way as holes in strongly correlated Hubbard model. The present author in collaboration with Kikuchi and Kanamori proposed a model from a different point of view.[23] They assumed that the carriers for superconducting current are chiefly in apical oxygens, where the assumption was based on the experimental results by Bianconi et al.,[24] and that the carriers form local triplet with Cu spins. The model was not very successful, because sufficient attractive interaction was not obtained for moving holes. Now dozens of similar effective Hamiltonians to that of Zhan and Rice have been proposed. Most of these effective models have both the Heisenberg interaction between local spins at the Cu-site and effective hopping of excess holes in single band.[21-23, 25] They explain several experimental results, but no theories of the high-Tc super conductivity have been established.

On the other hand, more direct investigations on CuO_2 plane have been performed numerically by using the configuration interaction method; we can test the effective conduction models or restrict their extent by specifying orbitals in which the excess holes are. For example, Eskes and Sawatzky[26] have analyzed the role of apical oxygens — the off-plane oxygens — by using the Anderson impurity model, and showed that the apical oxygen is not relevant to the conduction via CuO_2 plane for realistic situations. The present author[27] in collaboration with Kanamori extends their consideration to a periodic system. They calculated ground state wave functions of Cu_4O_{12} cluster, which contains four CuO_5 clusters in it, and studied how the apical oxygens took their part in periodic circumstance. They showed that the off-plane oxygen-p_z orbitals worked as a short cut between in-plane oxygen-$p_{x(y)}$ orbitals, and about one tenth of the excess holes passed through the off-plane oxygens. They observe no ferromagnetic coupling between the excess holes in apical oxygens and Cu spins. The result placed a restriction on the effective Hamiltonians known so far; those which are based on the Hund rule coupling in Cu-$3d$ orbitals are denied.[23] Matsukawa and Fukuyama [28] have included the role of off-plane oxygens — as the short cut — into the d-p model through a perturbative consideration.

Electronic structure of the CuO_2 plane has also been studied in connection with core and valence band photo emission (or absorption) spectroscopies. Balseiro, Avignon and Gagliano[29] calculated the valence band XPS spectra of the d-p model by use of the 'modified Lanczos method' formulated by Gagliano and Balseiro[30], and discussed how the spectra near Fermi energy changed with both electron and hole doping. Kuramoto and Shmidt[31] calculated the angle resolved XPS and BIS spectra and indicated a narrowing of valence band. They pointed out that the structure of the $2p$ band is not changed so much by the intra-atomic Coulomb interaction in Cu-$3d$ orbitals. The present author extended their study to Cu-$2p$ core level XPS and XAS spectra, and discussed a role of periodicity of the d-p model.[32] It was the first attempt to calculate the core-level spectra for a highly correlated periodic system. He showed that small multiple peak appeared in the high-energy side of the main and the satellite peaks of core-level XPS spectra, in consequence of valence hole relaxation. The main-peak-shift with hole doping was also examined. Wagner, Hanke and Scalapino[33] calculated the optical conductivity of d-p and Hubbard model, and discussed the presence of the Zhang-Rice singlet state. Recently Eskes, Meinders and Sawatzky[34] have reported an anomalous transfer of spectral weight in doped correlated system. Now the central debates on the spectro-scopies are that whether there is a large Fermi surface in the valence band or not, and that what is the lowest excitation in charge degree of freedom. The study of one- and two-particle excitation spectra of the d-p model is still in progress to answer these questions.

The electron correlation effect in transition metal compounds has been carried out as we have reviewed above. The main problem comes from the competition between the band energy and the short range Coulomb interaction in $3d$; since the former is diagonal in the momentum space and the latter is diagonal in the real space, we cannot treat them exactly at the same time. Generally speaking, the correlation effect is important in low dimensional systems. A number of solids, in addition to the transition metal compounds, reflect the correlation effect. For example, quasi one-dimensional organic crystals, such as tetracyanoquinodimethan(TCNQ)[35,36] and related materials, have a very narrow band, thereby a weak Coulomb interaction greatly changes their conduction properties;[37] some of them show the superconductivity. Beni and Pincus[38] assumed a modified Hubbard model for TCNQ and discussed its thermodynamic properties by using a classical approximation. Their model is called the 'extended Hubbard model' today. Recently, many

theoretical methods, that are obtained through the study of high-Tc materials, have been applied to the one-dimensional extended Hubbard model.[39,40] Cannon, Scalettar and Fradkin have studied the ground state phase diagram of the model.[41] They confirm the presence of tricritical point. The present author have calculated the charge excitation gap of the model at half-filling by the exact diagonalization of the model Hamiltonian for a finite system.[42] Compared with the mean field theory, the calculated gap was considerablly reduced by the electron itinerancy throughout the parameter space, especially near the phase boundary.

§1.2 Scope of Each Chapter

The purpose of this thesis is to investigate non-perturbative effects of electron correlations and itinerancy in the valence band of low dimensional systems, especially the High-Tc compounds. We reproduce these systems into a computer, and calculate their ground state wave functions to obtain physical observables, such as magnetic correlations, electron densities, charge excitation gap, etc., under various circumstances. The periodic clusters, that have several transition metal atoms in them, are employed. Since we duplicated the system into a computer, we can impose any perturbations on each atom to get the response of the system. In other word, all that we will see in the following are experiments on the objects — the reproduction of real materials — in a computer.

Throughout in this thesis, we study periodic models written by a general Hamiltonian

$$H = \sum_{i,j\sigma} \varepsilon_{ij} c^{\dagger}_{i\sigma} c_{j\sigma} + \sum_{\substack{<i,j> \\ \sigma,\sigma'}} U_{ij} n_{i\sigma} n_{j\sigma'} , \tag{1.1}$$

where the first term contains both on-site energy and inter-site hopping amplitude of valence holes or electrons; the coefficients ε_{ij} determines the dispersion of the valence band. The second term represents on-site and inter-site Coulomb repulsions. Ratio of these ε_{ij}'s and U_{ij}'s determines the conduction and the magnetic properties of the system. In the following, we directly diagonalize the Hamiltonian by use of the Lanczos method[43] and study ground state properties and charge excitation gap of the periodic system.

We review the details of the numerical method in the next chapter, the method which is used for the analyses in chapters III~VI. A specific procedure to represent the Hamiltonian of a finite size cluster is shown with several cording techniques for computation. The algorithms of the Lanczos method and the recursion method are also shown.†

In chapter III, we investigate the electronic structure of the CuO_2 plane with apex oxygens by use of the Cu_4O_{12} cluster with the periodic boundary condition for two in-plane directions. The cluster is the smallest replica among those taking account of the electron transfer between CuO_5 units with the translational invariance of the CuO_2 plane. We substitute realistic parameters into the Hamiltonian(eq.1.1) and calculate the ground state wave function. The role of apex oxygens is chiefly examined. When extra holes are introduced, they have amplitudes on all the atoms including the apex oxygens unlike the case of the single CuO_5 cluster. The result agrees with the experimental result by Bianconi et al.[24] that there is finite hole occupancy in the apical oxygens. No appreciable spin correlation between the apex oxygen-p_z orbital and Cu-$d(x^2-y^2)$ is found, even though there is a strong Hund rule coupling in Cu-$3d$. We also examine spin correlations between other pairs of orbitals and spin and charge fluctuations of a CuO_5 cluster.

We then calculate one-hole excitation spectra of one- and two-dimensional d-p model in chapter IV. The d-p Hamiltonian — a special case of the Hamiltonian in eq. 1.1 — is written by creation and annihilation operators for both p and d orbitals in CuO_2 plane:

$$\begin{aligned} H_{d-p} = \epsilon_p \sum_{i\sigma} p^\dagger_{i\sigma} p_{i\sigma} + \epsilon_d \sum_{j\sigma} d^\dagger_{j\sigma} d_{j\sigma} - t_{pd} \sum_{<i,j>\sigma} (p^\dagger_{i\sigma} d_{j\sigma} + d^\dagger_{j\sigma} p_{i\sigma}) \\ - t_{pp} \sum_{<i,l>\sigma} (p^\dagger_{i\sigma} p_{l\sigma} + p^\dagger_{l\sigma} p_{i\sigma}) + U_p \sum_i p^\dagger_{i\uparrow} p_{i\uparrow} p^\dagger_{i\downarrow} p_{i\downarrow} \\ + U_d \sum_j d^\dagger_{j\uparrow} d_{j\uparrow} d^\dagger_{j\downarrow} d_{j\downarrow} . \end{aligned} \tag{1.2}$$

The difference of on-site energies $\epsilon_p - \epsilon_d$ is the so called 'charge transfer energy',[12] which is usually denoted as Δ. The nearest neighbor hopping between $2p$ and $3d$ orbitals, and in between $2p$ orbitals are t_{pd} and t_{pp}, respectively. The last two terms in the r. h. s are interaction parts due to the on-site Coulomb repulsion in $2p$ orbitals (U_p) and in $3d$ orbitals.(U_d) We mainly investigate the realistic cases where $U_d > U_p > \Delta \sim t_{pd} > t_{pp}$.

† Those who are not interested in computation shall pass the second chapter.

We calculate ground state wave functions for various hole densities, and obtain the Cu-$2p$ XPS, Cu-$2p$ XAS, BIS and valence band XPS spectra by use of the modified Lanczos method. Size dependence of the spectra including the valence band XPS and BIS as well is examined by extending the calculation to linear clusters containing up to seven d-orbitals. We chiefly study effects of the hole itinerancy as well as those of the hole correlation on these spectra. It is shown that the Cu $2p$ XPS spectra consist generally of three groups of peaks which are assigned to $|\underline{c}d^{10}\underline{L}\rangle$, $|\underline{c}d^{9}\rangle$ and $|\underline{c}d^{10}\underline{L}^{2}\rangle$ final states. The last one which was not obtained by use of either a single Cu atom cluster or the impurity Anderson model appears in between the first two in energy. The main peak corresponding to the $|\underline{c}d^{10}\underline{L}\rangle$ state shifts with concentration of additional holes consistently with experimental data on Y-Ba-Cu oxides.

In chapter V, the charge transfer gap of the one-dimensional d-p model is calculated as a function of intra- and inter-atmic Coulomb repulsion and the charge transfer energy. We evaluate the gap by use of a 'two dimensional filter'* in particle number space. The inter-atomic Coulomb repulsion enhances the charge transfer gap, but it cannot be the origin of the gap; the gap is nearly zero when $\Delta = 0$ even if there is finite inter-atomic Coulomb repulsion. The strong intra-atomic Coulomb energy case is also discussed.

In chapter VI, we study the charge excitation gap of the one-dimensional extended Hubbard model, whose Hamiltonian has the form

$$H = -t \sum_{<i,j>\sigma} (c^{\dagger}_{i\sigma} c_{j\sigma} + c^{\dagger}_{j\sigma} c_{i\sigma}) + U \sum_{i} n_{i\uparrow} n_{i\downarrow} + V \sum_{<i,j>} (n_{i\uparrow} + n_{i\downarrow})(n_{j\uparrow} + n_{j\downarrow}) - \mu \sum_{i} (n_{i\uparrow} + n_{i\downarrow}). \tag{1.3}$$

The first two terms in the right hand side represent the Hubbard Hamiltonian. The third term is the Coulomb repulsion between neighboring sites. The chemical potential $\mu = 2V + U/2$ corresponds to the half-filled band. The charge excitation gap at half-filling is obtained via the finite size scaling method. Compared with the Hartree-Fock solution, the gap is reduced by the itinerancy of electrons throughout the $U - V$ plane, especially near the boundary of the Mott-Hubbard and the CDW phases.

In the last chapter, we summarize the conclusions on the electron correlation effect in the periodic finite size systems.

* The definition of the filter is discussed in the Appendix.

References

1. N. F. Mott: *Metal-Insulator Transisions.* (Taylor & Francis, 1974).
2. O. Madelung: *Introduction to Solid-State Theory.* (Springer, 1978) p. 356.
3. J. C. Slater: Phys. Rev. **82** (1951) 538.
4. K. Terakura, T. Oguchi, A.R.Williams, and J.Kübler: Phys. Rev. **30** (1984) 4734.
5. N. F. Mott: Proc. Phys. Soc. **A62** (1949) 416; Can. J. Phys. **34** (1956) 1356; Phil. Mag. **6** (1961) 287.
6. J. Hubbard: Proc. Roy. Soc. **A276** (1963) 238; **A281** (1964) 401.
7. D. N. Zubarev, Usp. Fiz. Nauk. **71** (1960) 71. *Translation*: Soviet Physics Uspekhi **3**, 320.
8. J. H. Van Vleck: Rev. Mod. Phys. **25** (1953) 220.
9. J. Slater, H. Statz, and G. F. Koster: Phys. Rev. **91** (1953) 1323.
10. J. Kanamori: J. Phys. Soc. Jpn. **30** (1963) 275.
11. M. C. Gutzwiller: Phys. Rev. **137** (1965) A1726.
12. J. Zaanen, G. A. Sawatzky, and J. W. Allen: Phys. Rev. Lett. **55** (1985) 418.
13. J. Zaanen, C. Westra, and G. A. Sawatzky: Phys. Rev. **B33** (1986) 8060.
14. J. G. Bednorz and K. A. Muller: Z. Phys. **B64** (1986) 189.
15. M. K. Wu, J. R. Ashburn, C. J. Torng, P. H. Hor, R. L. Meng, L. Gao, Z. J. Haang, Y. Q. Wang, and C. W. Chu: Phys. Rev. Lett. **58** (1987) 908.
16. H. Maeda, Y. Tanaka, M. Fukutomi, and T. Asano, Jpn. J. Appl. Phys. **27** (1988) L209.
17. T. Siegrist, S. Sunsine, D. W. Murphy, R. I. Cave, and S. M. Zahurak: Phys. Rev. **B35** (1987) 7137.
18. P. W. Anderson: Science **235** (1987) 1196.
19. P. W. Anderson, G. Baskaran, Z. Zou, and T. Hsu: Phys. Rev. Lett. **58** (1987) 2790; G. Baskaran and P. W. Anderson: Phys. Rev. **B37** (1988) 580.
20. V. J. Emery: Phys. Rev. Lett. **58** (1987) 2794.
21. M. Imada: *Mechanism of High Temperature Superconductivity,* eds. H. Kamimura and A. Oshiyama (Springer, Berlin, 1988) p. 53.
22. F. C. Zhang and T. M. Rice: Phys. Rev. **B37** (1988) 3759.
23. T. Nishino, M. Kikuchi, and J. Kanamori: Solid State commun. **68** (1988) 455.

24. A. Bianconi, M. De Santis, A. Di Cicco, A. M. Flank, A. Fontaine, P. Lagarde, H. Katayama-Yoshida, A. Kotani, and A. Marcelli: Phys. Rev. **B38** (1988) 7196.
25. M. Ogata and H. Shiba: *Mechanism of High Temperature Superconductivity,* eds. H. Kamimura and A. Oshiyama (Springer, Berlin, 1988) p. 44.
26. H. Eskes and G. A.Sawatzky: Phys. Rev. **B61** (1988) 1415.
27. T. Nishino and J. Kanamori: J. Phys. Soc. Jpn. **59** (1990) 253.
28. H. Matsukawa and H. Fukuyama: J. Phys. Soc. Jpn. **59** (1990) 1723.
29. C. A. Balseiro, M. Avignon and E. R. Gagliano: Solid State Commun. **72** (1989) 763.
30. E. R. Gagliano and C. A. Balseiro: Phys. Rev. Lett. **59** (1987) 2999; Phys. Rev. **B38** (1988) 11766.
31. Y. Kuramoto and H. J.Schmidt: *Strong Correlation and Superconductivity,* eds. H. Fukuyama, S. Maekawa, and A.P.Malozemoff (Springer, Berlin, 1989) p. 88.
32. T. Nishino: J. Phys. Soc. Jpn. **59** (1990) 4376.
33. J. Wagner, W. Hanke and D. J. Scalapino: Phys. Rev. **B43** (1991) 10517.
34. H. Eskes, M. B. J. Meinders, and G. A.Sawatzky: Phys. Rev. Lett. **67** (1991) 1035.
35. A. J. Epstein, S. Etemad, A. F. Garito, and A. J. Heeger: Phys. Rev. **B5** (1972) 952.
36. R. A. Bari and T. A. Kaplan: Phys. Rev. **B6** (1972) 4623; D. Cabib and D. A. Kaplan, Phys. Rev. **B7** (1973) 2199.
37. S. Kagoshima, T. Sambongi and H. Nagasawa: *One-Dimensional Conductors* (Syokabo, Tokyo, 1982). (In Japanese)
38. G. Beni and P. Pincus: Phys. Rev. **B9** (1973) 2963.
39. A. E. Ruckenstein, P. J. Hirschfeld, and J. Appel: Phys. Rev. **B36** (1987) 857.
40. P. G. J. van Dongen: Phys. Rev. Lett. **67** (1991) 757.
41. J. W. Cannon, R. T. Scalettar, and E. Fradkin: Phys. Rev. **B44** (1991) 5995.
42. T. Nishino: unpublished. (See Chap. VI.)
43. C. Lanczos: J. Res. Nat. Bur. Std. **45** (1950) 255.

Chapter II
Numerical Methods

§2.1 Introduction

A numerical technique is nothing but a step to get physical information from quantum or classical systems, and is never our final object. A limited capacity of avaliable computers, however, requires us to develop efficient methods of calculation without which we cannot draw meaningful conclusions from numerical computation. Thus, in this chapter we review and discuss the detail of each specific numerical method that is used in the following chapters, and that has impruved features compared with methods known so far.

As was mentioned in Chapter I, we investigate finite size systems described by the Hamiltonian

$$H = \sum_{i,j\sigma} \varepsilon_{ij} c^{\dagger}_{i\sigma} c_{j\sigma} + \sum_{\substack{<i,j> \\ \sigma,\sigma'}} U_{ij} n_{i\sigma} n_{j\sigma'}, \tag{2.1}$$

which includes both the d-p and the Hubbard Hamiltonian. The ϵ_{ij}'s and U_{ij}'s are of the order of electron volt.(eV) We take the electron picture — the $c^{\dagger}_{i\sigma}$ and $c_{i\sigma}$ represent creation and annihilation operators of electrons, respectively — throughout this chapter for convenience. We represent the Hamiltonian by a large scale Hermite or real-symmetric matrix and diagonalize it numerically in order to get physical observables.

We first study a way of representing the Hamiltonian by a Hermite matrix: we count electron configurations in a finite size system,(§2.2) and then calculate the matrix elements of H in the configuration space.(§2.3) Sometimes the matrix is too large to diagonaize; in the case we reduce the matrix size by use of a symmetry of the system.(§2.4) We next discuss how to diagonalize the Hamiltonian matrix, and how to obtain physical observables. As far as our system is concerned, the matrix is much larger than that we can diagonalize by usual methods, such as the *QR method* or the *House Holder method.*[1] In §2.5, we therefore introduce the Lanczos method[2] to diagonalize the large scale matrix, and to obtain the low-lying eigenvalues including the ground state energy. Once we succeed in obtaining the ground state energy and the corresponding wave function, we can calculate any observables as we please. One particle excitation spectrum is also obtained by

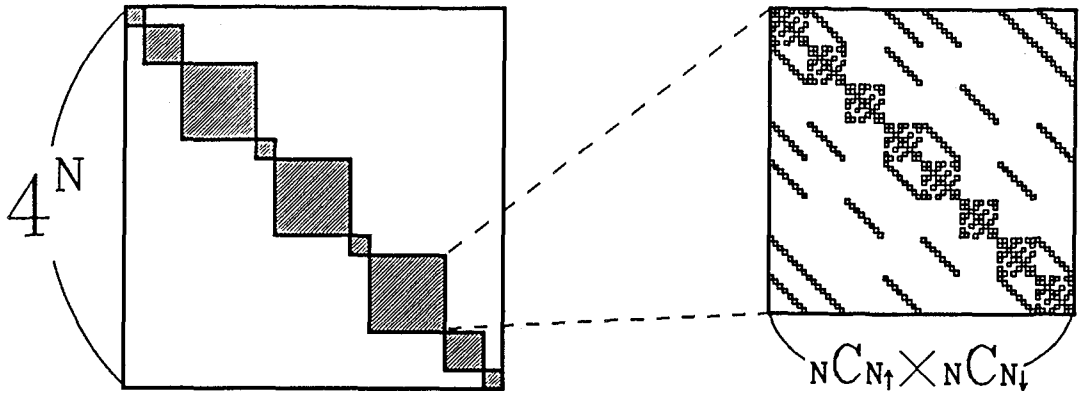

Fig. 2.1. Distribution of non-zero elements in the Hamiltonian. The matrix element is finite only in the shaded region, since the Hamiltonian conserves the particle number. Each shaded region is a ${}_NC_{N\uparrow} * {}_NC_{N\downarrow}$ by ${}_NC_{N\uparrow} * {}_NC_{N\downarrow}$ square matrix.

Haydock's recursion formula,[3] which is an extension of the Lanczos method.(§2.6) We briefly discuss applicability of the numerical method in the last section.(§2.7)

The following numerical methods prove their real worth when we perform the computations on super computers. We should design the structure of variables in programs so that the parallel computation will be smoothly performed in actual computations; the variable structures are briefly discussed at the end of each section.

§2.2 Basis Set in Real Space

When there are N atomic orbitals in a system, the Hamiltonian in eq. 2.1 is 4^N by 4^N Hermite matrix, because four electron configurations $0, \uparrow, \downarrow$ and $\uparrow\downarrow$ are possible for each orbital. One does not, however, have to diagonalize such a large matrix directly, since the Hamiltonian conserves the number of up- and down-spin electrons, $N_\uparrow$ and $N_\downarrow$, respectively; the Hamiltonian is represented by a direct product of smaller matrices.(Fig. 2.1) One may as well diagonalize each sub-matrix. (Shaded squares in Fig. 2.1) The dimension of each sub-matrix is ${}_NC_{N\uparrow} * {}_NC_{N\downarrow}$, since there are ${}_NC_{N\sigma}$ configurations for spin-σ electrons. *From now on, we confine ourselves to discuss a subspace specified by $N_\uparrow$ and $N_\downarrow$.*

Let us use γ_i^σ $(i = 1, 2, ..., {}_N C_{N\sigma})$ to denote electron configurations in the sub-space, and Γ^σ to the set of these configurations $\{\gamma_1^\sigma, ..., \gamma_i^\sigma, ...\}$. The set of all electron configurations Γ in the subspace is thus given by

$$\Gamma \equiv \Gamma^\uparrow \oplus \Gamma^\downarrow = \{\gamma_1^\uparrow \gamma_1^\downarrow, ..., \gamma_i^\uparrow \gamma_j^\downarrow, ...\}. \tag{2.2}$$

We align these electron configurations $\gamma_i^\uparrow \gamma_j^\downarrow \in \Gamma$ in order of the integer

$$(ij) \equiv i * {}_N C_{N\downarrow} + j, \tag{2.3}$$

since this order is convenient to the numerical calculation. We define each real-space basis state that has the configuration $\gamma_{i\uparrow}\gamma_{j\downarrow}$ as

$$\begin{aligned} |\gamma_{i\uparrow}\gamma_{j\downarrow}\rangle &= \tilde{c}_{N\uparrow}\tilde{c}_{N-1\uparrow}, ..., \tilde{c}_{1\uparrow}\ \tilde{c}_{N\downarrow}\tilde{c}_{N-1\downarrow}, ..., \tilde{c}_{1\downarrow}|0\rangle \\ &= |\gamma_i^\uparrow\rangle|\gamma_j^\downarrow\rangle, \end{aligned} \tag{2.4}$$

where the operator $\tilde{c}_{n\sigma}$ is $c_{n\sigma}^\dagger$ if there is a spin-σ electron at n-site in the configuration $\gamma_{i\uparrow}\gamma_{j\downarrow}$, and is $\mathbf{1}$ (=identity operator) otherwise. All of these $|\gamma_{i\uparrow}\gamma_{j\downarrow}\rangle$'s span the Hilbert space of the sub-space.

In the computation, each configuration γ_i^σ is represented by a binary number

$$\texttt{GAMMA}(i, \sigma) = \sum_{j=1}^{N} 2^{j-1} \langle \gamma_i^\sigma | c_{j\sigma}^\dagger c_{j\sigma} | \gamma_i^\sigma \rangle, \tag{2.5}$$

and is stored into an integer valued array-variable.† It is well known that another integer array that is closely related to the GAMMA as

$$\texttt{INVERS}(\texttt{l}, \sigma) = \begin{cases} i, & \text{if } {}^\exists\texttt{GAMMA}(i, \sigma) = \texttt{l} \\ 0, & \text{otherwise,} \end{cases} \qquad (0 \le \texttt{l} \le 2^N - 1) \tag{2.6}$$

is worth storing for two reasons.[4,5]

(i) We can judge whether a certain binary number b represents a configuration in Γ_σ or not; if $\texttt{INVERS}(b, \sigma) \neq 0$, then there is a configuration that satisfies $b = \texttt{GAMMA}(i, \sigma)$.

(ii) When $i = \texttt{INVERS}(b, \sigma) \neq 0$, the array gives the position of γ_i^σ in the set Γ^σ.

These integer variables, GAMMA and INVERS, are frequently referenced at every step in the following computations.

† Names written in CAPITAL TYPE FACED CHARACTERS always denote variables for actual FORTRAN programs which were coded by the author.

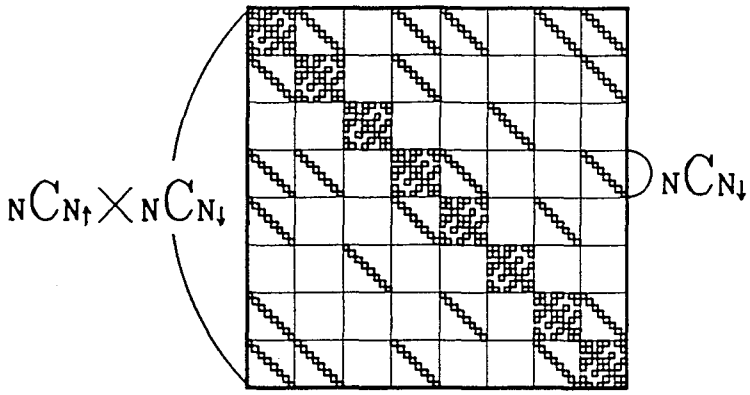

Fig. 2.2. Distribution of non-zero elements in the Hamiltonian matrix $[H\ ] = [\hat{T}^{\uparrow}] + [\hat{T}^{\downarrow}] + [\hat{D}]$. The matrix element is finite only in the shaded regions and on the dotted positions.

§2.3 Non-Zero Elements in the Hamiltonian Matrix

Having obtained the basis set $\{|\gamma_1^{\uparrow}\gamma_1^{\downarrow}\rangle, ..., |\gamma_i^{\uparrow}\gamma_j^{\downarrow}\rangle, ...\}$, we calculate the matrix element

$$H_{(ij)(kl)} = \langle\gamma_i^{\uparrow}\gamma_j^{\downarrow}|H|\gamma_k^{\uparrow}\gamma_l^{\downarrow}\rangle, \tag{2.7}$$

where (ij) and (kl) are the integers defined by eq. 2.3. If we write down the matrix elements explicitly, we will find out that the matrix is sparse and non-zero elements appear regularly. (Fig. 2.2) The diagonal part of the Hamiltonian matrix $[H_{(ij)(kl)}]$* comes from the on-site energy and the Coulomb energy:

$$D_{(ij)(kl)} \equiv \langle\gamma_i^{\uparrow}\gamma_j^{\downarrow}|\hat{D}|\gamma_k^{\uparrow}\gamma_l^{\downarrow}\rangle = \delta_i^k\delta_j^l\langle\gamma_i^{\uparrow}\gamma_j^{\downarrow}|\hat{D}|\gamma_i^{\uparrow}\gamma_j^{\downarrow}\rangle, \tag{2.8}$$

$$\hat{D} = \sum_{i,\sigma}\varepsilon_{ii}n_{i\sigma} + \sum_{\substack{<i,j> \\ \sigma,\sigma'}} U_{ij}n_{i\sigma}n_{j\sigma'}\,. \tag{2.9}$$

The block diagonal parts are kinetic energies of down-spin electrons:

$$T^{\downarrow}_{(ij)(kl)} \equiv \langle\gamma_i^{\uparrow}\gamma_j^{\downarrow}|\hat{T}^{\downarrow}|\gamma_k^{\uparrow}\gamma_l^{\downarrow}\rangle = \delta_i^k\langle\gamma_j^{\downarrow}|\hat{T}^{\downarrow}|\gamma_l^{\downarrow}\rangle, \tag{2.10}$$

$$\hat{T}^{\downarrow} = \sum_{i\neq j}\varepsilon_{ij}(c^{\dagger}_{i\downarrow}c_{j\downarrow} + c^{\dagger}_{j\downarrow}c_{i\downarrow})\,. \tag{2.11}$$

The off diagonal parts are kinetic energies of up-spin electrons:

$$T^{\uparrow}_{(ij)(kl)} \equiv \langle\gamma_i^{\uparrow}\gamma_j^{\downarrow}|\hat{T}^{\uparrow}|\gamma_k^{\uparrow}\gamma_l^{\downarrow}\rangle = \delta_j^l\langle\gamma_i^{\uparrow}|\hat{T}^{\uparrow}|\gamma_k^{\uparrow}\rangle, \tag{2.12}$$

$$\hat{T}^{\uparrow} = \sum_{i\neq j}\varepsilon_{ij}(c^{\dagger}_{i\uparrow}c_{j\uparrow} + c^{\dagger}_{j\uparrow}c_{i\uparrow})\,. \tag{2.13}$$

* A square bracket [ ] denotes a matrix.

Thus, the Hamiltonian matrix $[H]$ is the sum of $[D]$, $[T^{\uparrow}] = [\tau^{\uparrow}] \otimes I^{\downarrow}$ and $[T^{\downarrow}] = I^{\uparrow} \otimes [\tau^{\downarrow}]$, where I^{σ} is the identity operator for spin-σ electrons and $[\tau^{\sigma}_{ij}]$ is the tiny matrix $[\langle \gamma^{\sigma}_{i} | T^{\sigma} | \gamma^{\sigma}_{j} \rangle]$. The $[H_{(ij)(kl)}]$ is a real-symmetric matrix if all ε_{ij}'s are real; otherwise, it is a Hermite matrix.

In actual computation, we store the diagonal elements $D_{(ij)(ij)}$ into a real valued array $\mathtt{DIAG}(\mathtt{M} = (ij))$. The tiny matrices, $[\tau^{\sigma}_{ij}] \equiv [\langle \gamma^{\sigma}_{i} | T^{\sigma} | \gamma^{\sigma}_{j} \rangle]$ in eq. 2.9 and 2.12, are also sparse; we should store only non-zero elements in $[\tau^{\sigma}_{ij}]$ and their positions. Three array variables are employed:

$$\begin{cases} \mathtt{FTAU}(\mathtt{I}, \sigma) = \langle \gamma^{\sigma}_{i} | T^{\sigma} | \gamma^{\sigma}_{j} \rangle \\ \mathtt{ITAU}(\mathtt{I}, \sigma) = \quad i \\ \mathtt{JTAU}(\mathtt{I}, \sigma) = \quad j \qquad , \quad (i < j), \end{cases} \tag{2.14}$$

where the index I runs from 1 to the total number of non-zero elements in the upper triangular part of $[\tau^{\sigma}_{ij}]$. We can quickly find out the non-zero elements by using the variable $\mathtt{INVERS}(1, \sigma)$. For example, the value $\langle \gamma^{\sigma}_{j} | c^{\dagger}_{l\sigma} c_{m\sigma} | \gamma^{\sigma}_{i} \rangle$ is finite ($= \pm 1$) only when j is equal to $\mathtt{INVERS}(\mathtt{XOR}(2^{l-1} + 2^{m-1}, \mathtt{GAMMA}(i, \sigma)), \sigma) \neq 0$, where XOR represents the 'exclusive-or' between two binary numbers.

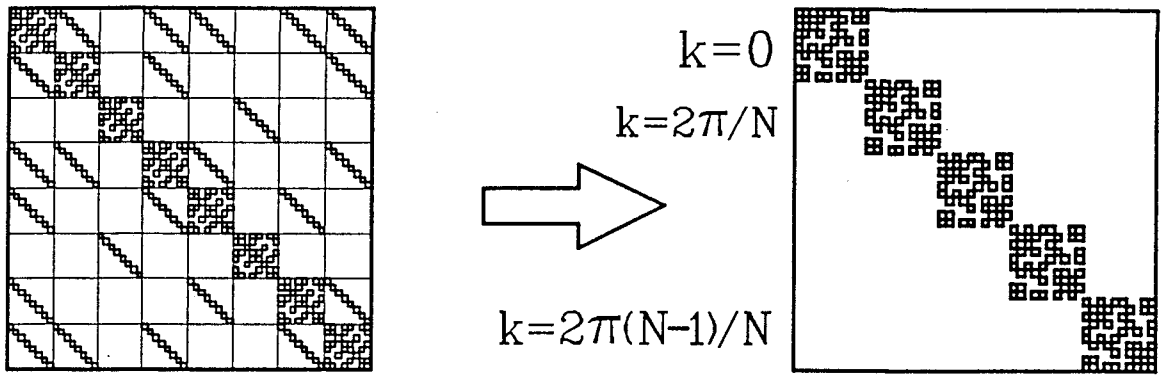

Fig. 2.3. Block diagonalization of the Hamiltonian by use of rotational (or translational) invariance of one-dimensional systems. The dimension of each sub-matrx is about ${}_NC_{N\uparrow} * {}_NC_{N\downarrow}$ / N.

§2.4 Reduction of Matrix Size by Use of a Symmetry†

The dimension of the matrix $\left[H_{(ij)(kl)}\right]$ grows very rapidly with the system size N. For example, when $(N, N_\uparrow, N_\downarrow)$ is $(14, 7, 7)$, the matrix size is $({}_{14}C_7)^2 = 11,778,624$; computation for such a large matrix requires considerable memories. If our computer does not have enough memory to treat such a large matrix, we have to reduce the matrix size by using some symmetries of the system. In this section, we discuss a method of the matrix-size-reduction for one-dimensional systems. The rotational symmetry is most efficient for any one-dimensional system with periodic boundary condition; one can block diagonalize the matrix $\left[H_{(ij)(kl)}\right]$ according to the total momentum k.[5,6](Fig. 2.3) In fact, it is worth using the rotational symmetry even if one has enough memory, because we can follow the dispersion relation of elementary excitations, such as the spin wave excitation, by use of the symmetry.

Let's modify the formula in §2.2 and §2.3 in order to reduce the matrix size. First we count the number of independent electron configurations again,(§2.4.1) and create ortho-normal basis vectors.(§2.4.2) We then store minimum information to reproduce the matrix elements, (§2.4.3) and transform the Hamiltonian matrix into a real-symmetric one.(§2.4.4) The formalism shown in the following sub-sections is also applicable for other symmetries of the system, with a slight modification.(§2.4.5)

† Those who have enough storage region in their computer might as well skip this section.

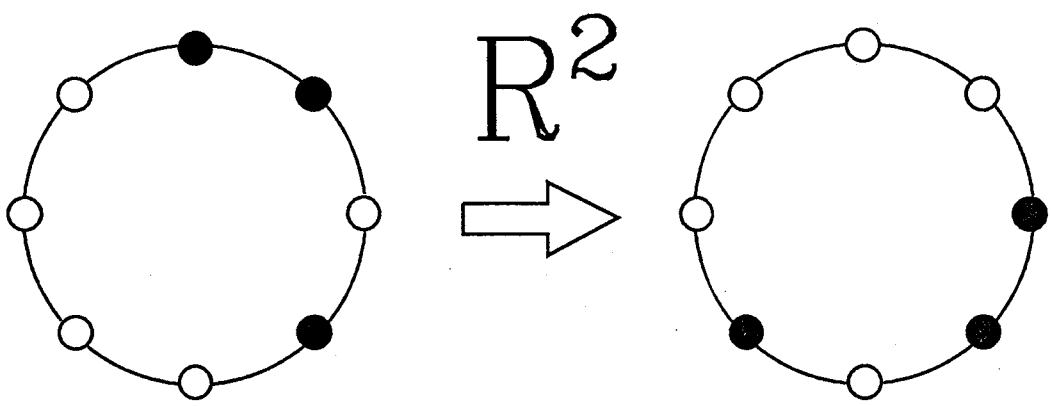

Fig. 2.4. Equivalent electron configurations; two electron configurations are equivalent if one is obtained by rotating another.

§2.4.1 *Reduction of the Electron Configurations*

Suppose there is a N-site one-dimensional system with periodic boundary condition — a N-site ring which is invariant under lattice rotation. We first introduce an equivalence relation between electron configurations on the lattice in order to reduce the number of bases: the γ_i^σ and the γ_j^σ are equivalent if we can transform the former into the latter by the lattice rotation

$$\gamma_i^\sigma \sim \gamma_j^\sigma, \quad {}^\exists n \;\; \gamma_i^\sigma = R^n \gamma_j^\sigma \,, \tag{2.15}$$

where R represents the rotation of the system by a lattice constant.(Fig. 2.4) We can naturally extend the relation to the elements in Γ:

$$\gamma_i^\uparrow \gamma_j^\downarrow \sim \gamma_k^\uparrow \gamma_l^\downarrow, \quad {}^\exists n \quad \gamma_i^\uparrow \gamma_j^\downarrow = R^n(\gamma_k^\uparrow \gamma_l^\downarrow) \equiv (R^n \gamma_k^\uparrow)(R^n \gamma_l^\downarrow). \tag{2.16}$$

By using this relation, we specify the smallest subset $\Gamma_R^\sigma \subset \Gamma^\sigma$ which satisfies the condition

$$\Gamma^\sigma = \sum_{n=0}^{N-1} \Re^n \Gamma_R^\sigma, \qquad (\Re : \gamma_i^\sigma \in \Gamma^\sigma \to R\gamma_i^\sigma \in \Gamma^\sigma), \tag{2.17}$$

and also introduce a subset $\Gamma_R \subset \Gamma$ in the same manner,

$$\Gamma = \sum_{n=0}^{N-1} \Re^n \Gamma_R, \qquad \left(\Re : \gamma_i^\uparrow \gamma_j^\downarrow \in \Gamma \to (R\gamma_i^\uparrow)(R\gamma_j^\downarrow) \in \Gamma\right). \tag{2.18}$$

The Γ_R contains all of the electron configurations that are necessary to represent the bases that have a momentum k.(See §2.4.2.) One might infer that Γ_R is the same as $\Gamma_R^{\uparrow} \oplus \Gamma^{\downarrow}$, since Γ is represented by

$$\begin{aligned}\Gamma &= \left(\sum_{l=0}^{N-1} \Re^l \Gamma_R^{\uparrow}\right) \oplus \left(\sum_{n=0}^{N-1} \Re^n \Gamma_R^{\downarrow}\right) \\ &= \sum_{l=0}^{N-1} \Re^l \left\{\Gamma_R^{\uparrow} \oplus \left(\sum_{m=0}^{N-1} \Re^m \Gamma_R^{\downarrow}\right)\right\} \\ &= \sum_{l=0}^{N-1} \Re^l \left(\Gamma_R^{\uparrow} \oplus \Gamma^{\downarrow}\right), \end{aligned} \tag{2.19}$$

but it is not always true. Actually Γ_R is a subset of $\Gamma_R^{\uparrow} \oplus \Gamma^{\downarrow}$; a few $\gamma_i^{\uparrow}$'s in $\Gamma_R^{\uparrow}$ satisfy the relation $\gamma_i^{\uparrow} \sim R^n \gamma_i^{\uparrow}$ for non-zero $n < N$, thereby some of the elements in $\Gamma_R^{\uparrow} \oplus \Gamma^{\downarrow}$ satisfy

$$\gamma_i^{\uparrow} \gamma_j^{\downarrow} = R^n (\gamma_i^{\uparrow} R^{-n} \gamma_j^{\downarrow}) \sim \gamma_i^{\uparrow} \gamma_k^{\downarrow}, \tag{2.20}$$

where $\gamma_j^{\downarrow} = R^n \gamma_k^{\downarrow}$ belongs to $\Gamma^{\downarrow}$. Thus we obtain Γ_R by projecting out such redundant elements from $\Gamma_R^{\uparrow} \oplus \Gamma^{\downarrow}$.

In the actual computation, we store the configurations $\gamma_i^{\uparrow} \in \Gamma_R^{\uparrow}$ and $\gamma_j^{\downarrow} \in \Gamma^{\downarrow}$ instead of $\gamma_i^{\uparrow} \gamma_j^{\downarrow} \in \Gamma_R$. We project out the redundant bases in $\Gamma_R^{\uparrow} \oplus \Gamma^{\downarrow}$ to get Γ_R when we create the basis vector in the next subsection.

§2.4.2 *Representation of the Basis states*

The total momentum $k(= 2l\pi/N,\ 0 \le l \le N-1)$ of the system is a well-defined quantity. We create an ortho-normal basis set for the subspace specified by k. A basis state that have the momentum k is given by

$$|\gamma_i^{\uparrow} \gamma_j^{\downarrow}; k\rangle \equiv \frac{1}{\sqrt{N}} \sum_{l=0}^{N-1} e^{ikl} |R^l(\gamma_i^{\uparrow} \gamma_j^{\downarrow})\rangle = \frac{1}{\sqrt{N}} \sum_{l=0}^{N-1} e^{ikl} |R^l \gamma_i^{\uparrow}\rangle |R^l \gamma_j^{\downarrow}\rangle, \tag{2.21}$$

where $\gamma_i^{\uparrow}\gamma_j^{\downarrow}$ is $(ij) \equiv (i * {}_N C_{N\downarrow} + j)$'th element in $\Gamma_R^{\uparrow} \oplus \Gamma^{\downarrow}$. Most of the bases given by eq. 2.21 are already normalized, but there are some exceptions. The norm of each base is

$$\begin{aligned} w(\gamma_i^{\uparrow}\gamma_j^{\downarrow}; k) &\equiv \langle \gamma_i^{\uparrow}\gamma_j^{\downarrow}; k | \gamma_i^{\uparrow}\gamma_j^{\downarrow}; k \rangle \\ &= \frac{1}{N} \sum_{l,m=0}^{N-1} e^{i(-l+m)k} \langle R^l \gamma_i^{\uparrow} | R^m \gamma_i^{\uparrow} \rangle \langle R^l \gamma_j^{\downarrow} | R^m \gamma_j^{\downarrow} \rangle \\ &= \sum_{n=0}^{N-1} e^{ink} \langle \gamma_i^{\uparrow} | R^n \gamma_i^{\uparrow} \rangle \langle \gamma_j^{\downarrow} | R^n \gamma_j^{\downarrow} \rangle, \end{aligned} \tag{2.22}$$

and is not always unity. Now, we introduce several notations for convenience:

$$s(\gamma_i^{\sigma}; n) \equiv \langle \gamma_i^{\sigma} | R^n \gamma_i^{\sigma} \rangle = \langle R^{-n} \gamma_i^{\sigma} | \gamma_i^{\sigma} \rangle = 0, \pm 1, \tag{2.23}$$

$$g(\ \gamma_i^{\sigma}\ ) = \sum_{n=0}^{N-1} \{ s(\gamma_i^{\sigma}; n) \}^2, \tag{2.24}$$

$$c^{\sigma}(i; n) = j, \tag{2.25}$$

where j in the r.h.s. of eq. 2.25 is the integer which satisfies $R^n \gamma_i^{\sigma} = \gamma_j^{\sigma}$. The $\gamma_i^{\uparrow}$'s and the $\gamma_i^{\downarrow}$'s here belong to the sets $\Gamma_R^{\uparrow}$ and $\Gamma^{\downarrow}$, respectively. The $g(\gamma_i^{\sigma})$ is either unity or a measure of N. If $g(\gamma_i^{\sigma})$ is unity then $s(\gamma_i^{\sigma}; n)$ is the same as δ_n^0. The norm $w(\gamma_i^{\uparrow}\gamma_j^{\downarrow}; k)$ is then written by $s(\gamma_i^{\sigma}; n)$ as

$$w(\gamma_i^{\uparrow}\gamma_j^{\downarrow}; k) = \sum_{n=0}^{N-1} e^{ink} s(\gamma_i^{\uparrow}; n) s(\gamma_j^{\downarrow}; n), \tag{2.26}$$

and is unity as far as $g(\gamma_i^{\uparrow})$ or $g(\gamma_j^{\downarrow})$ is unity. Let us introduce one more notation for the normalization constant:

$$n(\gamma_i^{\uparrow}\gamma_j^{\downarrow}; k) = \begin{cases} 0 & , \quad \text{if } w(\gamma_i^{\uparrow}\gamma_j^{\downarrow}; k) = 0; \\ \{ w(\gamma_i^{\uparrow}\gamma_j^{\downarrow}; k) \}^{-1/2}, & \text{otherwise.} \end{cases} \tag{2.27}$$

The normalized basis state that has momentum k is then expressed as

$$| \gamma_i^{\uparrow}\gamma_j^{\downarrow}; k \rangle_N = n(\gamma_i^{\uparrow}\gamma_j^{\downarrow}; k) | \gamma_i^{\uparrow}\gamma_j^{\downarrow}; k \rangle. \tag{2.28}$$

The normalization constant $n(\gamma_i^{\uparrow}\gamma_j^{\downarrow}; k)$ automatically projects out a base in eq. 2.21 whose norm is zero. Remember that we have to project out some more bases, since we use $\gamma_i^{\uparrow}\gamma_j^{\downarrow} \in \Gamma_R^{\uparrow} \oplus \Gamma^{\downarrow}$ instead of $\gamma_i^{\uparrow}\gamma_j^{\downarrow} \in \Gamma_R$. When $g(\gamma_i^{\uparrow} \in \Gamma_R^{\uparrow})$ is not unity, the $\gamma_i^{\uparrow}\gamma_l^{\downarrow}$ is

the same as $R^m(\gamma_i^\uparrow\gamma_j^\downarrow)$ for integers m and l that satisfy $s(\gamma_i^\uparrow;m)\neq 0$ and $l=c^\downarrow(j;m)$, respectively; the state $|\gamma_i^\uparrow\gamma_l^\downarrow;k\rangle$ is proportional to $|\gamma_i^\uparrow\gamma_j^\downarrow;k\rangle$. To avoid the duplication of bases, we must choose one out of these redundant bases. The rest of the redundant bases are rejected by changing the normalization factor $n(\gamma_i^\uparrow\gamma_l^\downarrow;k)$ into zero. Thus, one might as well store the configurations $\gamma_i^\uparrow\in\Gamma_R^\uparrow$, $\gamma_j^\downarrow\in\Gamma^\downarrow$, the factors $s(\gamma_i^\sigma)$, $g(\gamma_i^\sigma)$, $c^\sigma(i;n)$, $n(\gamma_i^\uparrow\gamma_j^\downarrow;k)$ and the complex numbers $\{1,e^{ik},e^{2ik},...,e^{(N-1)ik}\}$ in order to represent the orth-normalized basis set.

§2.4.3 *Matrix Elements*

We calculate matrix elements $H^k_{(ij)(lm)}\equiv_N\langle\gamma_i^\uparrow\gamma_j^\downarrow;k|(H=\hat{D}+\hat{T}^\uparrow+\hat{T}^\downarrow)|\gamma_l^\uparrow\gamma_m^\downarrow;k\rangle_N$ as follows. Since the on-site term $\hat{D}$ does not change the electron configuration, the matrix elements for $\hat{D}$ appear only in the diagonal part, as eq. 2.8:

$$\begin{aligned}D^k_{(ij)(lm)}&=_N\langle\gamma_i^\uparrow\gamma_j^\downarrow;k|\hat{D}|\gamma_l^\uparrow\gamma_m^\downarrow;k\rangle_N\\&=n(\gamma_i^\uparrow\gamma_j^\downarrow;k)^2\delta_i^l\delta_j^m\langle\gamma_i^\uparrow\gamma_j^\downarrow;k|\hat{D}|\gamma_i^\uparrow\gamma_j^\downarrow;k\rangle.\end{aligned}\tag{2.29}$$

Since the expectation value of $\hat{D}$ for the un-normalized base $|\gamma_i^\uparrow\gamma_j^\downarrow;k\rangle$ is

$$\begin{aligned}\langle\gamma_i^\uparrow\gamma_j^\downarrow;k|\hat{D}|\gamma_i^\uparrow\gamma_j^\downarrow;k\rangle&=\frac{1}{N}\sum_{l,m=0}^{N-1}e^{i(-l+m)k}\langle R^l\gamma_j^\downarrow|\langle R^l\gamma_i^\uparrow|\hat{D}|R^m\gamma_i^\uparrow\rangle|R^m\gamma_j^\downarrow\rangle\\&=\sum_{n=0}^{N-1}e^{ink}s(\gamma_i^\uparrow;n)s(\gamma_j^\downarrow;n)\langle\gamma_i^\uparrow\gamma_j^\downarrow|\hat{D}|\gamma_i^\uparrow\gamma_j^\downarrow\rangle\\&=w(\gamma_i^\uparrow\gamma_j^\downarrow;k)\langle\gamma_i^\uparrow\gamma_j^\downarrow|\hat{D}|\gamma_i^\uparrow\gamma_j^\downarrow\rangle,\end{aligned}\tag{2.30}$$

the diagonal part $D^k_{(ij)(lm)}$ is the same as the $D_{(ij)(lm)}$ in eq. 2.8:

$${}_N\langle\gamma_i^\uparrow\gamma_j^\downarrow;k|\hat{D}|\gamma_i^\uparrow\gamma_j^\downarrow;k\rangle_N=\langle\gamma_i^\uparrow\gamma_j^\downarrow|\hat{D}|\gamma_i^\uparrow\gamma_j^\downarrow\rangle.\tag{2.31}$$

Expressions of the off-diagonal elements are rather complicated. The expectation value of $\hat{T}^\uparrow$ for the un-normalized state is

$$\begin{aligned}\langle\gamma_i^\uparrow\gamma_j^\downarrow;k|\hat{T}^\uparrow|\gamma_l^\uparrow\gamma_m^\downarrow;k\rangle&=\frac{1}{N}\sum_{p,q=0}^{N-1}e^{i(-p+q)k}\langle R^p\gamma_j^\downarrow|\langle R^p\gamma_i^\uparrow|\hat{T}^\uparrow|R^q\gamma_l^\uparrow\rangle|R^q\gamma_m^\downarrow\rangle\\&=\sum_{n=0}^{N-1}e^{ink}\langle\gamma_i^\uparrow|\hat{T}^\uparrow|R^n\gamma_k^\uparrow\rangle\langle\gamma_j^\downarrow|R^n\gamma_l^\downarrow\rangle,\end{aligned}\tag{2.32}$$

where each factor can be further factorized by the known variables as

$$\begin{aligned}\langle\gamma_i^\uparrow|\hat{T}^\uparrow|R^n\gamma_k^\uparrow\rangle &= \sum_l \langle\gamma_i^\uparrow|\hat{T}^\uparrow|\gamma_l^\uparrow\rangle\langle\gamma_l^\uparrow|R^n\gamma_k^\uparrow\rangle \\ &= \langle\gamma_i^\uparrow|\hat{T}^\uparrow|\gamma_k^\uparrow\rangle\langle\gamma_k^\uparrow|R^n\gamma_k^\uparrow\rangle \\ &= \langle\gamma_i^\uparrow|\hat{T}^\uparrow|\gamma_k^\uparrow\rangle s(\gamma_k^\uparrow;n) \end{aligned} \tag{2.33}$$

and

$$\langle\gamma_j^\downarrow|R^n\gamma_l^\downarrow\rangle = \delta^j_{c^\downarrow(l;n)} f(l;n). \tag{2.34}$$

The new factor $f(l;n) = \pm 1$ is the sign which comes from the ordering of Fermion operators. The matrix elements $T^k_{(ij)(lm)} \equiv {}_N\langle\gamma_i^\uparrow\gamma_j^\downarrow;k|\hat{T}^\uparrow|\gamma_l^\uparrow\gamma_m^\downarrow;k\rangle_N$ are then obtained by multiplying the normalization constant $n(\gamma_i^\uparrow\gamma_j^\downarrow;k)n(\gamma_l^\uparrow\gamma_m^\downarrow;k)$ to $\langle\gamma_i^\uparrow\gamma_j^\downarrow;k|\hat{T}^\uparrow|\gamma_l^\uparrow\gamma_m^\downarrow;k\rangle$. The $g(\gamma_i^\uparrow)$ is unity and $s(\gamma_i^\uparrow;n)$ is the same as δ^0_n for most of the $\gamma_i^\uparrow$'s. Therefore there are only a few non-zero elements for $n \neq 0$ in eq. 2.33. The matrix elements for $\hat{T}^\downarrow$ is given as we have done for $\hat{T}^\uparrow$:

$$\langle\gamma_i^\uparrow\gamma_j^\downarrow;k|\hat{T}^\downarrow|\gamma_l^\uparrow\gamma_m^\downarrow;k\rangle = \sum_{n=0}^{N-1} e^{ink}\langle\gamma_i^\uparrow|R^n\gamma_l^\uparrow\rangle\langle\gamma_j^\downarrow|\hat{T}^\downarrow|R^n\gamma_m^\downarrow\rangle, \tag{2.35}$$

where

$$\langle\gamma_i^\uparrow|R^n\gamma_l^\uparrow\rangle = \delta^i_l s(\gamma_l^\uparrow;n), \tag{2.36}$$

$$\langle\gamma_j^\downarrow|\hat{T}^\downarrow|R^n\gamma_m^\downarrow\rangle = \langle\gamma_j^\downarrow|\hat{T}^\downarrow|\gamma^\downarrow_{c^\downarrow(m;n)}\rangle f(m;n). \tag{2.37}$$

All that we have to store in order to express the matrix is thus the diagonal elements $D_{(ij)(ij)}$, the sign $f(l;n)$ and the tiny matrix $[\tau^\sigma_{ij}] = \left[\langle\gamma_i^\sigma|\hat{T}^\sigma|\gamma_j^\sigma\rangle\right]$ in addition to the factors $s(\gamma_i^\sigma)$, $g(\gamma_i^\sigma)$, $c^\sigma(i;n)$ and $n(\gamma_i^\uparrow\gamma_j^\downarrow;k)$. Most of these quantities should be stored into integer arrays to save the memory space. If one has enough memory, one would better directly store the off-diagonal elements $\langle\gamma_i^\sigma|\hat{T}^\sigma|R^n\gamma_j^\sigma\rangle$ instead of dividing it into three factors $\langle\gamma_i^\sigma|\hat{T}^\sigma|\gamma_l^\sigma\rangle$, $f(j;n)$ and $c(j:n)$ so that the computation speeds up.

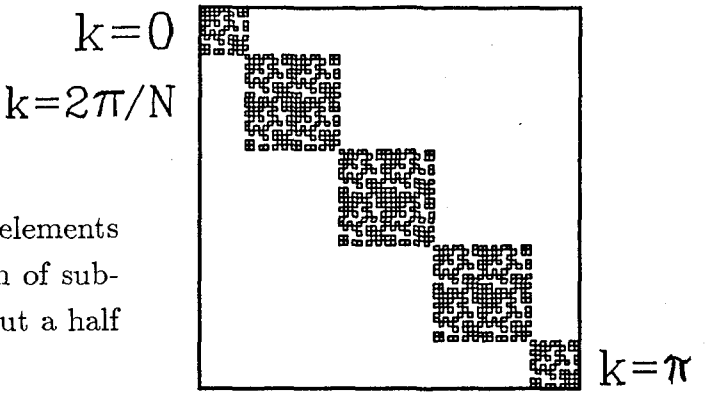

Fig. 2.5. Map of non-zero elements in $\left[H^k_{(ij)(lm)}\right]$. The dimension of subspaces for $k = 0$ and π is about a half of those of other subspaces.

§2.4.4 *Real-Symmetric Representation of the Hamiltonian*

The matrix $\left[H^k_{(ij)(lm)}\right]$ is Hermite, and is real-symmetric only if $k = 0$ or π. Since a real-symmetric matrix is more preferable in numerical calculation than a Hermite one, we transform $\left[H^k_{(ij)(lm)}\right]$ into a real symmetric matrix. Let us introduce new basis states

$$|\gamma_i^{\uparrow}\gamma_j^{\downarrow};k\rangle^{(+)} \equiv \frac{1}{\sqrt{2}}\left(|\gamma_i^{\uparrow}\gamma_j^{\downarrow};k\rangle + |\gamma_i^{\uparrow}\gamma_j^{\downarrow};-k\rangle\right)$$
$$= \sqrt{\frac{2}{N}}\sum_{l=0}^{N-1} cos(kl)|R^l(\gamma_i^{\uparrow}\gamma_j^{\downarrow})\rangle, \tag{2.38}$$

$$|\gamma_i^{\uparrow}\gamma_j^{\downarrow};k\rangle^{(-)} \equiv \frac{1}{\sqrt{2}i}\left(|\gamma_i^{\uparrow}\gamma_j^{\downarrow};k\rangle - |\gamma_i^{\uparrow}\gamma_j^{\downarrow};-k\rangle\right)$$
$$= \sqrt{\frac{2}{N}}\sum_{l=0}^{N-1} sin(kl)|R^l(\gamma_i^{\uparrow}\gamma_j^{\downarrow})\rangle, \tag{2.39}$$

so that the Hamiltonian matrix always be real-symmetric. The bases $|\gamma_i^{\uparrow}\gamma_j^{\downarrow};k\rangle^{(+)}$ and $|\gamma_i^{\uparrow}\gamma_j^{\downarrow};k\rangle^{(-)}$ are defined in the regions $0 \leq k \leq \pi$ and $2\pi/N \leq k \leq (N-2)\pi/N$, respectively.

If we represent H by use of the new basis set, the size of each block diagonal matrix becomes twice as large as that of the $\left[H^k_{(ij)(lm)}\right]$ for each k, except for $k = 0$ and π, since the ${}^{(+)}\langle\gamma_i^{\uparrow}\gamma_j^{\downarrow};k|H|\gamma_l^{\uparrow}\gamma_m^{\downarrow};k\rangle^{(-)}$ is not always zero.(Fig. 2.5) Most of the procedures to calculate matrix elements through eq. 2.21 $\sim$ eq. 2.37 are of use; we might as well avoid repeating here the lengthy calculation.

§2.4.5 *Reduction by Other Symmetries*

We have reduced the size of the Hamiltonian matrix by a factor of N by use of the rotational invariance of N-site ring. The reduction is, however, not sufficient if one tries the calculations on large N systems, such as the Hubbard model at half-filling for $N > 14$. One inevitably use other symmetries in addition to the rotational symmetry in order to further reduce the matrix size.[5,6]

Most of the technique shown above are of use to other symmetries, such as inversion, mirror, charge conjugation, etc., with slight modification. Usually, not all of the symmetries are independent, and therefore one should make a group table and clarify the relation between the elements in each group. The most dangerous step where one would easily make a mistake is the step to find out the reduced set Γ_R in eq. 2.18. A combination of several symmetries unexpectedly makes two configurations be equivalent. One should carefully make Γ_R before creating basis set and calculating the matrix elements.

§2.5 Lanczos Method

Today the maximum size of the matrix which we can diagonalize by usual direct methods — the **Householder method** or the **QR method**[1] — is of the order of 10^4, since modern super computers have a few giga-bytes of main memories at most. However, the matrix $\left[H_{(ij)(kl)}\right]$ or $\left[H^k_{(ij)(lm)}\right]$ immediately exceeds the limit with increasing N. For example, the size of the $\left[H_{(ij)(kl)}\right]$ is 63504 for 10-site Hubbard model at Half-filling. We have to adopt other diagonalization method. Remember that the parameters ε_{ij} and U_{ij} in the Hamiltonian (eq. 2.1) are of the order of eV, and that we are studying properties of the system at low- or at most room-temperature; only the low-lying eigenvalues of H are necessary for our study. The **Lanczos method**[2] is appropriate for such a requirement.

The Lanczos method is a diagonalization algorithm for a large scale real-symmetric matrix; we can obtain the first several lowest (and highest) eigenvalues of a matrix up to 10^7 dimension. The method has one more advantage: *if the matrix is sparse, one can get the largest and the smallest eigenvalues fairly faster than other diagonalizaton methods.* Now let us review the algorithm of the Lanczos method and its property.

§2.5.1 *Algorithm of the Lanczos Method*

Suppose there is a M by M real-symmetric matrix A whose eigenvalues and ortho-normalized eigenvectors are $\lambda_1 \leq \lambda_2 \leq ... \leq \lambda_M$ and $\mathbf{V}_1, \mathbf{V}_2, ..., \mathbf{V}_M$,respectively. Any M dimensional real vector $\mathbf{q}$ can be written by a linear combination of $\mathbf{V}_\mu$'s,

$$\mathbf{q} = \sum_{\mu=1}^{M} a_\mu \mathbf{V}_\mu. \tag{2.40}$$

If we multiply A to an arbitrary vector $\mathbf{q}$ for number of times, the vector $A^n\mathbf{q}/|A^n\mathbf{q}|$ will approach a certain eigenvector of A; it is the **power method**, so called.[1] The method is not realistic in two points: **(a)** One can get only one eigenvalue λ_μ whose absolute value is the largest, and the eigenvector which corresponds to λ_μ. **(b)** If there are some eigenvalues that are very close to λ_μ, the convergence of the series $\{\mathbf{q}, A\mathbf{q}/|A\mathbf{q}|, A^2\mathbf{q}/|A^2\mathbf{q}|, ...\}$ will be worse.

We can overcome these two problems by representing the matrix A in the sub-space spanned by the vectors $\{\mathbf{q}, A\mathbf{q}, ..., A^m\mathbf{q}\}$, where $m << N$. Let $\{\mathbf{q}_1, \mathbf{q}_2, ..., \mathbf{q}_m\}$ be an ortho-normal set obtained through the **Gram-Schimidt orthogonalization** on $\{\mathbf{q}, A\mathbf{q}, ..., A^m\mathbf{q}\}$. An eigenvector $\mathbf{V}_\mu$ that corresponds to a large eigenvalue λ_μ would be well approximated by a linear combination of $\mathbf{q}_1, \mathbf{q}_2, ...,$ and $\mathbf{q}_m$. Conversely, several eigenvalues of the m by m matrix B defined by

$$B_{ij} = (\mathbf{q}_i, A\mathbf{q}_j) = (A\mathbf{q}_i, \mathbf{q}_j) = B_{ji} \tag{2.41}$$

are good approximation of those of A. If λ is a such eigenvalue of B and $\mathbf{a} =^t (a^1, a^2, ..., a^m)$ is an eigenvector of B that corresponds to λ, then a vector

$$\mathbf{R} = \sum_{i=1}^{m} a^i \mathbf{q}_i \tag{2.42}$$

will be a good approximation of an eigenvector of A.

The Lanczos Method *performs the re-orthogonalization of the vectors* $\{\mathbf{q}, A\mathbf{q}, ..., A^m\mathbf{q}\}$ *by using a kind of conjugate gradient (CG) method.*[1] The ortho-normal set $\{\mathbf{q}_1, \mathbf{q}_2, ..., \mathbf{q}_m\}$ is obtained by the recursive operations, the so called '**Lanczos**

step':

$$\begin{aligned}
\mathbf{q}_1 &= \mathbf{q} \\
\beta_1 \mathbf{q}_2 &= A\mathbf{q}_1 - (\mathbf{q}_1, A\mathbf{q}_1)\mathbf{q}_1 \\
\beta_2 \mathbf{q}_3 &= A\mathbf{q}_2 - (\mathbf{q}_2, A\mathbf{q}_2)\mathbf{q}_2 - (\mathbf{q}_1, A\mathbf{q}_2)\mathbf{q}_1 \\
\beta_3 \mathbf{q}_4 &= A\mathbf{q}_3 - (\mathbf{q}_3, A\mathbf{q}_3)\mathbf{q}_3 - (\mathbf{q}_2, A\mathbf{q}_3)\mathbf{q}_2 \\
&\vdots \\
\beta_m \mathbf{q}_{m+1} &= A\mathbf{q}_m - (\mathbf{q}_m, A\mathbf{q}_m)\mathbf{q}_m - (\mathbf{q}_{m-1}, A\mathbf{q}_m)\mathbf{q}_{m-1} \,. \qquad (2.43)
\end{aligned}$$

At every step, a new normalized vector $\mathbf{q}_l$ is obtained by orthogonalizing $A\mathbf{q}_{l-1}$ to the previous two vectors $\mathbf{q}_{l-1}$ and $\mathbf{q}_{l-2}$. The inner product $(\mathbf{q}_l, A\mathbf{q}_l)$ is conventionally written as α_l. The β_l's are normalization constants so that $|\mathbf{q}_l|$ is unity. In fact, $\mathbf{q}_l$ is already orthogonal to all of its previous vectors $\mathbf{q}_1, \mathbf{q}_2, ..., \mathbf{q}_{l-1}$, where the orthogonality among $\mathbf{q}_l$'s is justified through the relation[2,3]

$$\beta_l = (\mathbf{q}_l, A\mathbf{q}_{l-1}) = (\mathbf{q}_{l-1}, A\mathbf{q}_l). \qquad (2.44)$$

Thus, the matrix $B = [(\mathbf{q}_i, A\mathbf{q}_j)]$ in eq. 2.41 is tridiagonal as far as we use the $\mathbf{q}_l$'s obtained through the Lanczos step, and the matrix is written by α_l's and β_l's

$$B = \begin{bmatrix}
\alpha_1 & \beta_1 & 0 & \cdots & \cdots & \cdots & 0 \\
\beta_1 & \alpha_2 & \beta_2 & 0 & & & \vdots \\
0 & \beta_2 & \alpha_3 & \beta_3 & 0 & & \vdots \\
\vdots & 0 & \beta_3 & \ddots & \ddots & & \vdots \\
\vdots & & 0 & \ddots & \ddots & \ddots & 0 \\
\vdots & & & & \ddots & \alpha_{m-1} & \beta_{m-1} \\
0 & \cdots & \cdots & \cdots & 0 & \beta_{m-1} & \alpha_m
\end{bmatrix}. \qquad (2.45)$$

Since B is tridiagonal, we can quickly diagonalize it by the **bi-section method**.[1] It is known that when m is sufficiently large, ($\approx$ several hundreds) the largest and the smallest eigenvalues of B are the same as those of A within the numerical accuracy.

An eigenvector of the matrix A is also obtained approximately by substituting elements of an eigenvector of B into eq. 2.41. The vector $\mathbf{R}$ is called 'the Lanczos vector'. Since the vector $\mathbf{R}$ is not always a good approximation of a true eigenvector of A, we would better

apply the **inverse iteration method** [1] combined with the **conjugate gradient (CG) method**[1] to the Lanczos vector $\mathbf{R}$ in order to reduce the numerical error.

§2.5.2 *Computation in the Lanczos Step*

The Lanczos method is practical in deed when the Lanczos step is performed by using the smallest storage region. We study here a specific way for the Lanczos step, the way which use only main-memory of a computer. †

Consider a virtual processor that has three vector registers, V_1, V_2 and V_3 say, where their vector length is M. We use the boxes $\boxed{\mathbf{V_3}}\boxed{\mathbf{V_2}}\boxed{\mathbf{V_1}}$ to denote these registers. We can work out the computation in eq. 2.43 by storing vectors into the register as follows:

#	Procedure	Register After the Proc.			Comment/Kind of Proc.
		V_3	V_2	V_1	
(i)	Choose $\lvert\mathbf{q}_1\rvert = 1$			$\mathbf{q}_1$	Initialization
(ii)	$\mathbf{p}_1 = A\mathbf{q}_1$		$\mathbf{p}_1$	$\mathbf{q}_1$	Multiplication
(iii)	$\alpha_1 = \mathbf{q}_1 \cdot \mathbf{p}_1$		$\mathbf{p}_1$	$\mathbf{q}_1$	Inner Product
(iv)	$\mathbf{r}_1 = \mathbf{p}_1 - \alpha_1\mathbf{q}_1$	$\mathbf{r}_1$	$\mathbf{p}_1$	$\mathbf{q}_1$	Orthogonalization
(v)	$\beta_1 = \sqrt{\mathbf{r}_1 \cdot \mathbf{r}_1}$	$\mathbf{r}_1$	$\mathbf{p}_1$	$\mathbf{q}_1$	Inner Product
(vi)	$\mathbf{q}_2 = \mathbf{r}_1/\beta_1$	$\mathbf{q}_2$	$\mathbf{p}_1$	$\mathbf{q}_1$	Normalization
(vii)	$\mathbf{p}_2^* = A\mathbf{q}_2$	$\mathbf{q}_2$	$\mathbf{p}_2^*$	$\mathbf{q}_1$	Multiplication
(viii)	$\mathbf{p}_2 = \mathbf{p}_2^* - \beta_1\mathbf{q}_1$	$\mathbf{q}_2$	$\mathbf{p}_2$	$\mathbf{q}_1$	Orthogonalization
(ix)	Move $\mathbf{q}_2$ to $\mathbf{V}_1$		$\mathbf{p}_2$	$\mathbf{q}_2$	Copy
(x)	Go to (iii)		$\mathbf{p}_2$	$\mathbf{q}_2$	Repeat (iii)–(ix)

† We do not use any file space here. If we use the space, we can treat a huge scale matrix, but the computation requires much time to access the file space through very slow I/O interface.

Every time we pass through the steps (iii)–(ix) we obtain a set of coefficients (α_i, β_i). We then diagonalize the tri-diagonal matrix B every five or ten Lanczos steps until the lowest eigenvalue or the second lowest eigenvalue converges.†

The registers $\boxed{\mathbf{V_3}}\boxed{\mathbf{V_2}}\boxed{\mathbf{V_1}}$ are realized as a real-valued array `VECTOR(0:M-1, 0:2)` in actual programs. One would better declare them as 64-bit floating number to get a fast convergence of the lowest eigenvalue; you should use 32-bit floating number only when you don't have enough memory space to store the array.

In conclusion, the Lanczos method is appropriate for a large scale sparse matrix because of these two convenient properties:

(a) The matrix A is not changed at all during the computation. All one have to do about A at each Lanczos step is to multiply A to a unit vector $\mathbf{q}_i$. Thus, one can pass through the Lanczos step without possessing all of the elements in A; one might as well have only non-zero elements.

(b) We have to store only three vectors, in addition to the non-zero elements in A in order to perform the Lanczos method, since one can get the new basis vector $\mathbf{q}_l$ from the previous two vectors.

§2.5.3 *Application to the Lattice Fermion System*

The application of the Lanczos method to our system is straightforward, since we have already obtained the non-zero matrix elements $H_{(ij)(kl)}$ (or $H^k_{(ij)(lm)}$). We prepare an arbitrary state vector

$$|Initial\rangle \equiv \sum_{(ij)} q_{(ij)} |\gamma_i^{\uparrow} \gamma_j^{\downarrow}\rangle \tag{2.46}$$

as the trial vector $\mathbf{q}_1$ in eq. 2.43, where the $q_{(ij)}$'s satisfy the condition

$$\sum_{(ij)} \{q_{(ij)}\}^2 = 1. \tag{2.47}$$

We store the coefficients somewhere — memory spaces or file spaces, for they are of use when we create the Lanczos vector. We then repeat the Lanczos step by successively

† Sometimes one encounters a trouble, where the lowest eigenvalue of B falls down on and on, and never converges. In that case, there is a bug in his program, especially in the steps (i) and (ii). If A was not real-symmetric by a mistake, one would face the trouble.

multiplying the Hamiltonian matrix into a unit vector $\mathbf{q}_l$ in order to get the tri-diagonal matrix B. The lowest eigenvalue of B becomes a good approximation of the ground state energy E_0 for H after about one-hundred steps. The matrix multiplication is performed in four steps as far as the $\left[H_{(ij)(kl)}\right]$ is concerned; we multyply $[H] = [D] + [T^{\uparrow}] + [T^{\downarrow}]$ to an unit vector $\mathbf{q} = {}^t(q_{(11)}, ..., q_{(ij)}, ...)$ to obtain $\mathbf{p}$:

1) Set $p_{(ij)} = 0$ for all i and j.
2) Multiply $[D]$ to $\mathbf{q}$ as $p_{(ij)} = D_{(ij)}q_{(ij)}$.
3) Multiply $[T^{\uparrow}] = [\tau^{\uparrow}] \otimes I^{\downarrow}$ to $\mathbf{q}$ as $p_{(ij)} = p_{(ij)} + \tau^{\uparrow}_{ik}q_{(kj)}$.
4) Multiply $[T^{\downarrow}] = I^{\uparrow} \otimes [\tau^{\downarrow}]$ to $\mathbf{q}$ as $p_{(ij)} = p_{(ij)} + \tau^{\downarrow}_{jk}q_{(ik)}$.

The matrix multiplication procedure for $\left[H^k_{(ij)(kl)}\right]$ is complicated a little bit, since we have to multiply the normalization constant $n(\gamma^{\uparrow}_i\gamma^{\downarrow}_j; k)$ to $q_{(ij)}$ after the step 2) and to $p_{(ij)}$ after 4).

How about the ground state wave function? It is represented by the Lanczos vector $\mathbf{R}$ in eq. 2.42. It seems that one have to store all the $\mathbf{q}_i$'s into memory in order to obtain $\mathbf{R}$. It is, however, not true. We can create $\mathbf{q}_l$'s at any time as far as we have only $\mathbf{q}_1$; all that we have to store in order to get $\mathbf{R}$ are $\mathbf{q}_1$ and an eigenvector $\mathbf{a}$ that satisfies $B\mathbf{a} = \lambda_0\mathbf{a}$. The right hand side of eq. 2.42 is calculated successively by performing the Lanczos step again from the beginning. The procedure here is called 'the two pass method'[7] since we perform the Lanczos method twice. One would better integrate $\mathbf{q}_i$'s with the weight a_i after the step (iii) shown in the prevous subsection, because the vector $\mathbf{V_3}$ is empty there and we can use it as a work space.

Once we obtain the ground state wave function $|g\rangle$, we can evaluate any observables of the form

$$\langle\hat{O}\rangle \equiv \langle g|\hat{O}|g\rangle \tag{2.48}$$

as we please. If $\hat{O}$ is diagonal in configuration space, we can calculate the r.h.s. as the diagonal part $[D]$ in the Hamiltonian matrix $[H]$. If $\hat{O}$ consists of a linear combination of the bond-order $c^{\dagger}_{i\sigma}c_{j\sigma}$, we can calculate $\langle g|\hat{O}|g\rangle$ or $\langle g|c^{\dagger}_{i\sigma}c_{j\sigma}|g\rangle$ as we did for $\hat{T}^{\sigma}$. The integer variable `INVERS` defined by eq. 2.6 is greatly of use in the computation of $\langle\hat{O}\rangle$ for any $\hat{O}$.

§2.5.4 *Lanczos Method as a Perturbation Expansion*

The Lanczos method is usually nothing but a numerical technique for a large scale sparse matrix. A special choice of the initial vector $|0\rangle \equiv |Initial\rangle$ (or $\mathbf{q_1}$) for the Lanczos step, however, gives a physical character to the method as a perturbation expansion which is closely related with the cummulant expansion; the α_l's and the β_l's in the tri-diagonal matrix in eq. 2.45 give l-th order cummulant for the kinetic energy and the Coulomb interaction as follows.

Remember that our Hamiltonian is consists of two parts

$$H = H_0 + V, \tag{2.49}$$

where H_0 and V are one-body energies and Coulomb interactions, respectively. If we adopt a ground state of H_0 as the initial state $|0\rangle$, then the α_1 is the energy expectation value

$$\alpha_1 = \langle H_0 + V \rangle_0 \equiv \langle 0|(H_0 + V)|0\rangle = E_0^0 + \langle V \rangle_0, \tag{2.50}$$

where the $\langle V \rangle_0$ is the first order energy correction in stationary perturbation theory. (The angular bracket $\langle\ \rangle_0$ denotes the expectation value with respect to $|0\rangle$.) The first Lanczos step gives a new state $|1>$ defined by

$$\beta_1|1\rangle = (V - \langle V \rangle_0)|0\rangle, \tag{2.51}$$

where the normalization constant β_1 is

$$\beta_1 = \sqrt{\langle V^2 \rangle_0 - \langle V \rangle_0^2}, \tag{2.52}$$

that is the fluctuation of V in the initial state.The α_2 is the energy expectation for the new state $|1\rangle$, which is written by

$$\begin{aligned} \alpha_2 = \langle 1|H|1\rangle &= \frac{1}{\beta_1^2}\langle 0|(V - \langle V \rangle_0)(H_0 + V)(V - \langle V \rangle_0)|0\rangle \\ &= \frac{\langle V H_0 V \rangle_0 + \langle V^3 \rangle_0 - 2\langle V \rangle_0 \langle V^2 \rangle_0 - E_0 \langle V \rangle_0^2 + \langle V \rangle_0^3}{\langle V^2 \rangle_0 - \langle V \rangle_0^2} \end{aligned} \tag{2.53}$$

and is the third order cummulant in energy. In the same manner, we will get higher order cummulant successively as α_l's and β_l's. After m Lanczos steps, we get a m by m tri-diagonal matrix M_m. The lowest eigenvalue of M_m monotonously decreases with m and

is always the upper limit of the true ground state energy of H. For example, the matrix for $m = 2$ is

$$M_2 = \begin{bmatrix} \alpha_1 & \beta_1 \\ \beta_1 & \alpha_2 \end{bmatrix} \tag{2.54}$$

and its lowest eigenvalue is $\{ \alpha_1 + \alpha_2 - \sqrt{(\alpha_1 - \alpha_2)^2 + 4\beta^2} \}/2$, that is always smaller than α_1, the eigenvalue of $M_1 = [\alpha_1]$. Thus, if only we calculate the expectation values $\langle V \rangle_0$, $\langle V^2 \rangle_0$, $\langle H_0 V \rangle_0$, $\langle V H_0 V \rangle_0$, etc., by numerical or analytical technique, we can obtain the upper limit of the true ground state energy E_0. The Lanczos vector $\mathbf{R}$ in eq. 2.42 is, in reality, the corresponding variational-wave function. *Thus, the Lanczos method is a variational, and also a perturbative, method which is based on the cummulant expansion.*

The division of the Hamiltonian in eq. 2.49, is essential to the variational interpretation of the Lanczos method. For example, if we chose the Hartree-Fock Hamiltonian as the H_0, then the α_1 is the HF energy; the following α_l's and β_l's gives a systematic correction to the HF energy. If we would choose the true ground state $|\psi\rangle$ as the initial vector, then α_1 is the true ground state energy E_0 and all of the following α_l's and β_l's are zero. This means that a good choice of the initial state $|0\rangle$ (or $\mathbf{q_1}$) leads the result $\alpha_l >> \alpha_1$ or $\beta_l \sim 0$ for a small l. By using this property, *we would be able to look for a good analytical expression of the variational wave function Ψ, by substituting several trial wave functions into $|0\rangle$.*

§2.6 Recursion Method

We can obtain all of the 'static' properties of the finite size systems via eq. 2.48, while we cannot get the 'dynamical' character of them directly since we don't have all of the excited states. For example, intensities of photo-electron excitation spectra, inverse photo-electron excitation spectra and optical conductivity are expressed by

$$\begin{aligned} I(\omega) &= \sum_f |\langle f|\hat{A}|g\rangle|^2 \delta(\omega - E_f + E_0) \\ &= -\frac{1}{\pi}\mathrm{Im}\left\langle g\middle|\hat{A}^\dagger \frac{1}{\omega - H + E_0}\hat{A}\middle|g\right\rangle, \end{aligned} \tag{2.55}$$

where $\hat{A}$ represents a perturbation on the ground state, and the $|f\rangle$'s are excited states. If $\hat{A}$ is $c^\dagger_{i\sigma}$ or $c_{i\sigma}$, the $I(\omega)$ gives the density of states for occupied or un-occupied band, respectively. Gagliano and Balseiro[8] have shown that such a $I(\omega)$ can be given by a generalization of the Lanczos method, that originates from the **Heydock's recursion formula**.[3] (There is not a definite name of their method; it is occasionally called the Lanczos method, the modified Lanczos method,† the continued fraction method, or the recursion method.)

The algorithm of the recursion method is essentially the same as that of the Lanczos method. Suppose the (normalized) perturbed state is expressed by a linear combination of the real-space bases

$$\frac{\hat{A}|g\rangle}{\sqrt{\langle g|\hat{A}^\dagger\hat{A}|g\rangle}} = \sum_{(ij)} q_{(ij)}|\gamma_i^\uparrow \gamma_j^\downarrow\rangle. \tag{2.56}$$

We take the state as the initial vector $\mathbf{q}_1$ of the Lanczos method,* and repeat the Lanczos step (eq. 2.42) to get the tri-diagonal matrix B.(eq. 2.44) The (relative) spectral intensity is then given by a continued fraction written by α_l's and β_l's

$$I(\omega + i\epsilon) = -\frac{1}{\pi}\mathrm{Im}\cfrac{1}{\omega + i\epsilon - \alpha_1 - \cfrac{\beta_1^2}{\omega + i\epsilon - \alpha_2 - \cfrac{\beta_2^2}{\omega + i\epsilon - \alpha_3 - \cfrac{\beta_3^2}{\ddots}}}}, \tag{2.57}$$

† It would not be better to use the name 'modified Lanczos method' since it also stands for some other modifications of the Lanczos method. In this article we refer to the method as the 'recursion method', for the name is widely known

* One sometimes forgets to normalize the initial vector $\hat{A}|g\rangle$. Such a mistake is too trivial to find out, so one should code a program for the recursion method very carefully.

where the small imaginary term $i\epsilon$ gives a finite width to each peak. The total spectral weight is given by $\langle g|\hat{A}^\dagger\hat{A}|g\rangle$ in eq. 2.56. We don't have to calculate the r.h.s. exactly; a cut off via putting $\beta_m = 0$ at $m \sim 100$ for modest ϵ does not affect $I(\omega)$ at all. Thus, we can obtain excitation spectrum of a finite size system without calculating the factor $\langle f|\hat{A}|g\rangle$ explicitly. It should be noted that the recursion method is also efficient for a small sparse matrix; it gives $I(\omega)$ much faster than usual diagonalization methods.

§2.6.1 *Choice of the Operator $\hat{A}$*

A choice of the operator $\hat{A}$ in eq. 2.49 is essential in actual applications of the recursion method. If we intend to analyze the $I(\omega)$, which is obtained experimentally, via the numerical study on the finite size systems, the choice of $\hat{A}$ is unique; we should use $\hat{A}$ that represents the true excitation process in each experiment.[9] If we use the recursion method just in order to analyze the many body wave function $\Psi(x_{1\uparrow},...,x_{N_\uparrow\uparrow};x_{1\downarrow},...,x_{N_\downarrow\downarrow})$ obtained by the Lanczos method, the choice is arbitrary. In the latter case, we have to find out $\hat{A}$ that draws physical information from Ψ. We discuss here about examples of $\hat{A}$ which are bi-linear or bi-quadratic in Fermion operators.

We first see two basic examples. The total spectral weight $\int I(\omega)d\omega = \langle g|\hat{A}^\dagger\hat{A}|g\rangle$ for $\hat{A} = c_{i\sigma}$ or $\hat{A} = c_{k\sigma}$ represent the occupation number in real-space $\langle n_{i\sigma}\rangle$ or that in momentum-space $\langle n_{k\sigma}\rangle$, respectively. Both of them are special cases of $\hat{A}$'s which are bi-linear in $c_{i\sigma}$:

$$\hat{A} = \sum_i \phi_i c_{i\sigma}, \qquad \sum_i |\phi_i|^2 = 1. \tag{2.58}$$

The spectral weight $\langle\hat{A}^\dagger\hat{A}\rangle$ gives the occupation number of the one-body state ϕ. When there is no interaction between electrons or holes, the many-body wave function Ψ is just the Slater determinant

$$\Psi(x_{1\uparrow},...,x_{m\uparrow};x_{1\downarrow},...,x_n) = \begin{vmatrix} \varphi_1(x_{1\uparrow}) & \cdots & \varphi_m(x_{1\uparrow}) \\ \vdots & \ddots & \vdots \\ \varphi_1(x_{m\uparrow}) & \cdots & \varphi_m(x_{m\uparrow}) \end{vmatrix} \begin{vmatrix} \varphi_1(x_{1\downarrow}) & \cdots & \varphi_n(x_{1\downarrow}) \\ \vdots & \ddots & \vdots \\ \varphi_1(x_{n\downarrow}) & \cdots & \varphi_n(x_{n\downarrow}) \end{vmatrix}, \tag{2.59}$$

and the $\langle\hat{A}^\dagger\hat{A}\rangle$ has its maximum value (= unity) if the coefficient ϕ_i is the same as the $\varphi_l(x = i)$, i.e., the wave function of an occupied state. If finite Coulomb repulsion

is present, the Ψ is not the Slater determinant any more. Nevertheless, the so called 'one-body theory', such as Hartree-Fock approximation and many other band theories, assumes that quasi one-particle levels are still present. *If such a one-body level is present, the* $\langle \hat{A}^\dagger \hat{A} \rangle$ *that corresponds to the one-particle level should be nearly equal to unity, and there is only one dominant peak in* $I(E) = \langle \Psi | \hat{A}^\dagger \frac{1}{E-H} \hat{A} | \Psi \rangle$. *Conversely, we can find out such one-body states by finding out the operator* $\hat{A}$ *(or the set of coefficients* $\{\phi_1, \phi_2, ..., \phi_i, ...\}$*) which satisfies* $\langle \hat{A}^\dagger \hat{A} \rangle \sim 1$ *and gives the single peak structure to* $I(\omega)$. We can also find out empty levels in the same way, by exchanging the order of $\hat{A}^\dagger$ and $\hat{A}$. Generally speaking, one-body wave functions (φ_i) obtained by the Hartree-Fock (HF) approximation are good candidates of ϕ_i in eq. 2.58, while the one-body level position specified by the recursion method does not agree with that of the HF results.

Let us see typical candidates for $\{\phi_i\}$ for the d-p model, as an example. A present debate on the model is the character of one-particle levels near the Fermi energy, so far as we believe the presence of the Fermi surface. We can obtain the (most probable) occupied level, that has the momentum k,* by adjusting a parameter $0 \leq \theta < 2\pi$ so that the expectation value

$$\langle \hat{A}^\dagger \hat{A} \rangle = \langle \Psi | (cos\theta \; d^\dagger_{k\sigma} + sin\theta \; p^\dagger_{k\sigma})(h.\ c.) | \Psi \rangle \tag{2.60}$$

be maximum.† If there is the so called 'Zhang-Rice singlet state', the θ should be nearly equal to $\pi/2$ at the Fermi-surface. A preliminaly calculation of the spectral intensity $I(\omega)$ for $\theta = 0$ and π will be discussed in chapter IV. It will be shown there that free-Fermionic levels are still present even when there is a strong intra-atomic Coulomb interaction. Another debate on the d-p model is the locality of the valence holes. They frequently calculate (angle integrated) valence band photo-emission spectra of high-Tc materials by

* The lattice momentum depends on the definition of the d-p model; the k is different from the lattice momentum for the usual band theory.

† In actual calculation, we would better use operators $d^\dagger_k \pm d^\dagger_{-k}$ and $p^\dagger_k \pm p^\dagger_{-k}$ instead of $d^\dagger_k$ and $p^\dagger_k$ so that all of the numerical calculations shall be done without using any complex number.

use of a local $CuO_{n=4,5,6}$ cluster, assuming that the valence holes are localized to the cluster. If the holes are truly localized, the expectation value

$$\langle \hat{A}^\dagger \hat{A} \rangle = \langle \Psi | (cos\theta \; d^\dagger_{i\sigma} + sin\theta \frac{1}{\sqrt{n}} \sum_j p^\dagger_{j\sigma})(h.\; c.) | \Psi \rangle \tag{2.61}$$

should be of the order of unity for a certain θ, where j points the ligand sites around the i-site, and n is the coordination number of ligands.

We can also find out a local two-particle state as we have done for one-body states. Consider an operator $\hat{B}$ defined by

$$\hat{B}^\dagger | d^{10} \rangle \equiv \alpha | d^8 \rangle + \beta | d^9 \underline{L} \rangle + \gamma | d^{10} \underline{L}^2 \rangle \,, \tag{2.62}.$$

where the r.h.s. is the well-known local two-body state that have been studied by Sawatzky et. al.[10] We can specify the most realistic two-body state by finding out the operator $\hat{B}$ which gives the largest $\langle \Psi | \hat{B}^\dagger \hat{B} | \Psi \rangle$. If there would be a local Zhang-Rice singlet, the operator $\hat{B}$ of the form

$$\begin{aligned} \hat{B}_i &= \frac{1}{\sqrt{2}} (d_{i\uparrow} f_\downarrow - d_{i\downarrow} f_\uparrow) \\ f_\sigma &= \frac{1}{\sqrt{n}} \sum_j p_{j\sigma} \end{aligned} \tag{2.63}$$

should be selected through the search of the maximum $\langle \hat{B}^\dagger_i \hat{B}_i \rangle$ that gives a single peak structure to $I(\omega)$. Note that we can also catch a moving singlet state by use of the Foulier component $\hat{B}_k = \frac{1}{\sqrt{N}} \sum_l e^{ikl} \hat{B}_l$. The extension of the above formula to a local M-body state is straightforward. However, number of adjustable parameters as θ, α, β, and γ increases very rapidly with M; the upper limit of M shall be three or four.

§2.7 Discussion

We have studied the way of numerical calculation in diagonalization study for finite size lattice Fermion system. Once we had made up a program for the system described by the Hamiltonian, (eq. 2.1) we can apply the program to various electron conduction models by changing ε_{ij}'s and U_{ij}'s. All that we have to do in the following is to analyze the ground state wave function of the system. Specific methods for each observables shall be explained in the following chapters.

Those who try the diagonalization study should always pay their attention to the ability of their computers. Generally speaking, applications of the Lanczos method are limited by its memory requirement. In the following studies, all of the large-scale numerical calculations are performed by the *NEC SX-2N* super-computer which have 224M-byte main memory and a file space of the same order with rather slow I/O. The author code programs and perform trial calculations on *NEC ACOS-S2020* main frame computer which provides 128M-byte real memory.† Now both of these processors are not the largest and the fastest machine any more. We shall expand applicability of the diagonalization method in solid state physics by use of new super computers, such as *SX-3*, *VP2500* and the 'Connection Machine' *CM-2*.[9]

The numerical methods shown above are applicable to a system which contains more complicated interaction than that in eq. 2.1. For example, we can handle the Kondo interaction, the off-diagonal intra-atomic Coulomb interaction, spin-orbit interaction, etc., within our framework. (A special intra-atomic Coulomb interaction in Cu-$3d$ is treated in the next chapter.) The methods are also applicable to quantum spin systems. The most general program package for the system has been coded by Nishimori.[4] Kaburagi, Tonegawa and the present author modified Nishimori's program in order to study $S = 1$ spin chain, and also improved its speed.[10]†

† All of the programs for the diagonalization study are stored into *ACOS* in Computation Center, Osaka University, with read permission; one can use it any time as he pleases, as long as he keeps the *GNU* spirit.

† Now both Nishimori's and Kaburagi's programs for spin systems are opened to the public.[4,10]

References

1. for exaple, J. H. Wilkinson: *The Algebraic Eigenvalue Problem,* (Oxford Univ. Press, 1965).
2. C. Lanczos: J. Res. Nat. Bur. Std. **45** (1950) 255.
3. V. Heine: *Solid State Physics,* ed. H. Ehrenreich, F. Seitz and D. Turnbull (Academic Press, New York, 1980) Vol. **35**, p. 87.
4. H. Nishimori: Bussei Kenkyu **56** (1991) 494.(in Japanese); see also the *Reference Manual of* **TITPACK Ver.2**.
5. H. Q. Lin: Phys. Rev. **B42** (1990) 6561.
6. J. B. Parkinson and J. C. Bonner: Phys. Rev. **B32** 4703.
7. E. R. Gagliano, E. Dagotto, A. Morero and F. C. Alcaraz, Phys. Rev. **B34** (1986) 1677.
8. E. R. Gagliano and C. A. Balseiro: Phys. Rev. Lett. **28** (1989) 2999.
9. G. A. Sawatzky: private communication.
10. J. Zaanen, C. Westra, and G. A. Sawatzky: Phys. Rev. **B33**(1986) 8060; H. Eskes and G. A. Sawatzky: Phys. Rev. Lett. **61** (1988) 1415.
11. *Connection Machine CM-200 Series Technical Summary* (Thinking Machine Corporation, 1991).
12. M. Kaburagi, T. Tonegawa and T. Nishino: to be published; see also the *Reference Manual of* **OKTITPACK**.

Chapter III
Electronic Structure of CuO_3 Pyramidal Plane
— Role of Apical Oxygens —

§3.1 Introduction

The p-type oxide high-T_c superconductors so far known possess the CuO_2 planes on which each Cu atom is surrounded pyramidally by four in-plane oxygen atoms and an extra one at the apex site; in the case of the prototype of them, Ba-La-Cu-O system, they are surrounded octahedrally. The Tl-Ba-Ca-Cu-O and Bi-Sr-Ca-Cu-O systems possess another kind of the CuO_2 planes with Cu atoms surrounded only by four in-plane oxygen atoms without the apex ones. Since T_c as a function of the number of the latter kind of the CuO_2 planes decreases after passing a maximum, we may assume that the pyramidal planes are primarily responsible for the superconductivity.

The electronic structure of the pyramidal plane has been investigated using the impurity Anderson model or a CuO_5 cluster model.[1,2] The XPS and XAS experimental data have been analyzed also by use of these models.[3,4] Similar calculations have been done also in the case of n-type superconductors.[5] In these models, where the number of holes in the system is fixed, the charge fluctuation arising from the itinerancy of holes is not fully taken into account. If the holes in the system are not localized to a single CuO_5 cluster, representations of the point group of each CuO_5 cluster cease to be 'good quantum numbers'. For example, the sharp ground state transition of the cluster model from the $^1A_1$ state to the $^3B_1$ state with decreasing the Madelung energy of the apex oxygens shall not take place under periodic circumstance.

The author reports in this chapter a calculation of the ground electronic state of a model of the CuO_3 pyramidal plane. The model is consists of four CuO_5 pyramids sharing the in-plane oxygens. We substitute a realistic parameter set into our Hamiltonian,(eq.1.1) and calculate ground states of the system with and whithout extra holes. In the next section (§3.2) we give details of our model. In §3.3 we discuss the hole distribution. Section 3.4 deals with the spin and number correlations among various pairs of the orbitals. In §3.5 conclusions are summarized.

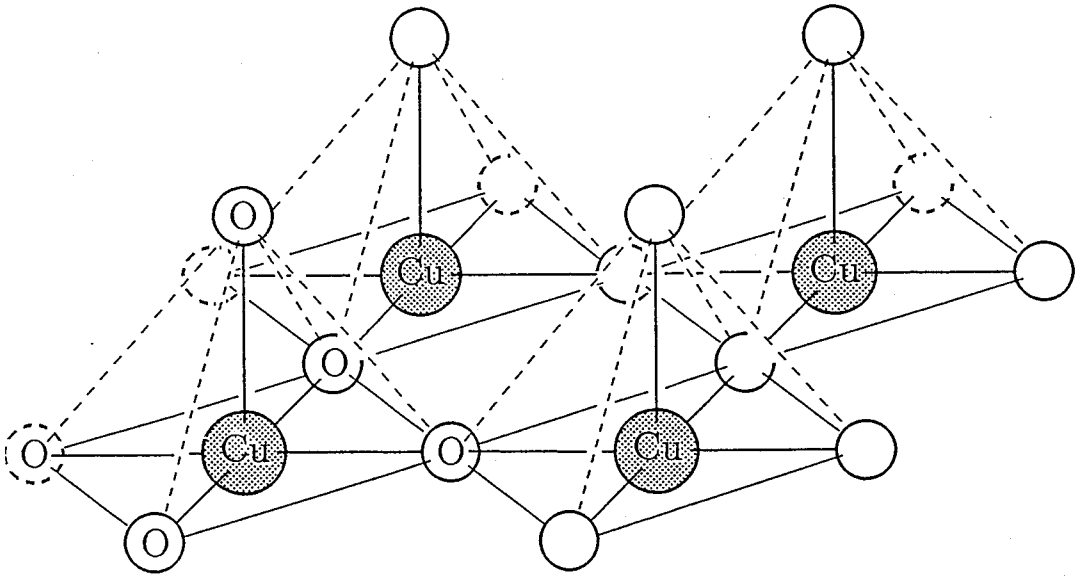

Fig. 3.1. A Cu_4O_{12} cluster used in the calculation. Large and small spheres denote Cu and oxygen atoms respectively. Periodic boundary conditions are imposed for both directions in the a-b plane.

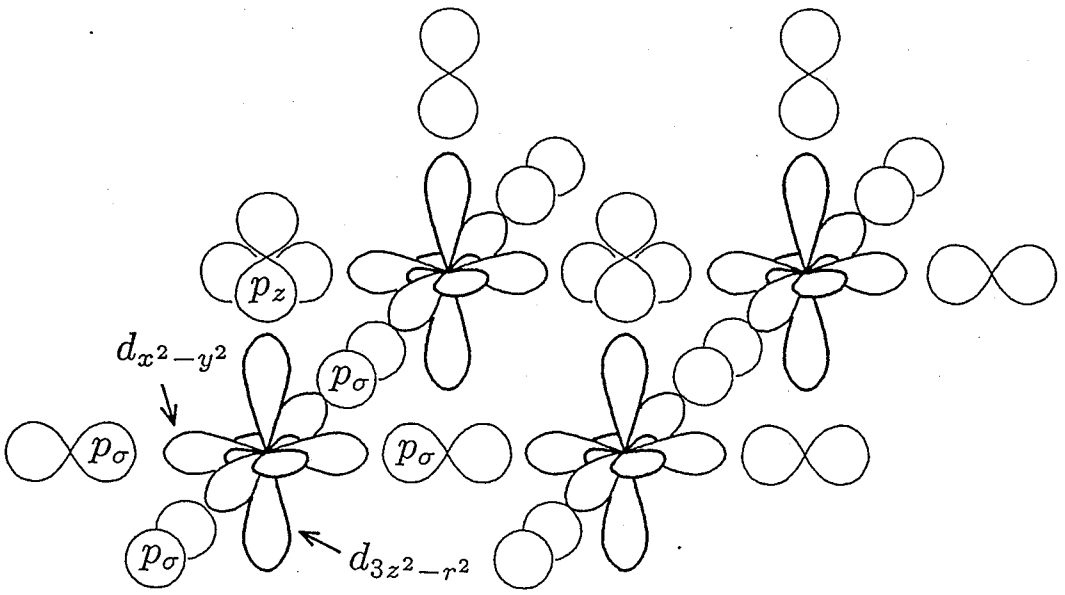

Fig. 3.2. The atomic orbitals in the Cu_4O_{12} cluster. We treat only the oxygen p orbitals that are σ bonded to the Cu $d\gamma$ orbitals.

§3.2 Model of the Pyramidal Plane

In this chapter we have employed a Cu_4O_{12} cluster, which may contain 4 or 6 holes, to study the effect of the intercluster itinerancy on the ground state.(Fig. 3.1) Although this is the smallest cluster allowing the itinerancy with the translational invariance of the CuO_2 plane, there are still too many atomic orbitals to calculate the ground state wave function with an exact treatment of the Coulomb interaction between holes. We confine ourselves, therefore, to twenty atomic orbitals shown in Fig. 3.2, that is, eight Cu $d\gamma$ orbitals, eight p_σ orbitals of in-plane oxygen atoms and four p_z orbitals of apex oxygen atoms. We take into account the electron (hole) transfer among Cu $d\gamma$ and oxygen p orbitals in the LCAO scheme,[6] assuming the same transfer parameters as in Fujimori's single cluster calculation, in-plane $(pp\sigma) = 0.5\text{eV}$, $(pd\sigma) = -1.35\text{eV}$, and $(pdm) \propto R^{-3.5}$, $(ppm) \propto R^{-2}$ with 1.23 for the ratio between the off-plane and in-plane Cu-O distances.[2] Coulomb and exchange interactions between Cu $d(x^2-y^2)$ and $d(3z^2-r^2)$ orbitals are treated exactly; $J = 5.3\text{eV}$ and $K = 0.8\text{eV}$ are assumed. The Coulomb self-energy of the oxygen p orbitals U_p and that of Cu d orbitals U_d are taken to be 3.0eV and 6.0eV, respectively. There are two remaining parameters $\Delta_{p\sigma}$ and Δ_{pz} which are the charge transfer energies defined by the difference of the one-hole energies between the in-plane or apex oxygen p orbitals and the Cu $d\gamma$ orbitals. The value of $\Delta_{p\sigma}$ is not well established yet.[7,8] Thus we vary it from 0.5eV to 2.5eV. Since no conspicuous change of the ground state is observed in this parameter range, we report here only the calculations for $\Delta_{p\sigma} = 1.5\text{eV}$ and 2.5eV. The parameter Δ_{pz} is varied within the range $0.0\text{eV} < \Delta_{pz} \leq \Delta_{p\sigma}$. Since the Hamiltonian conserves the total spin of the system, we investigate the ground state with zero total S^z.

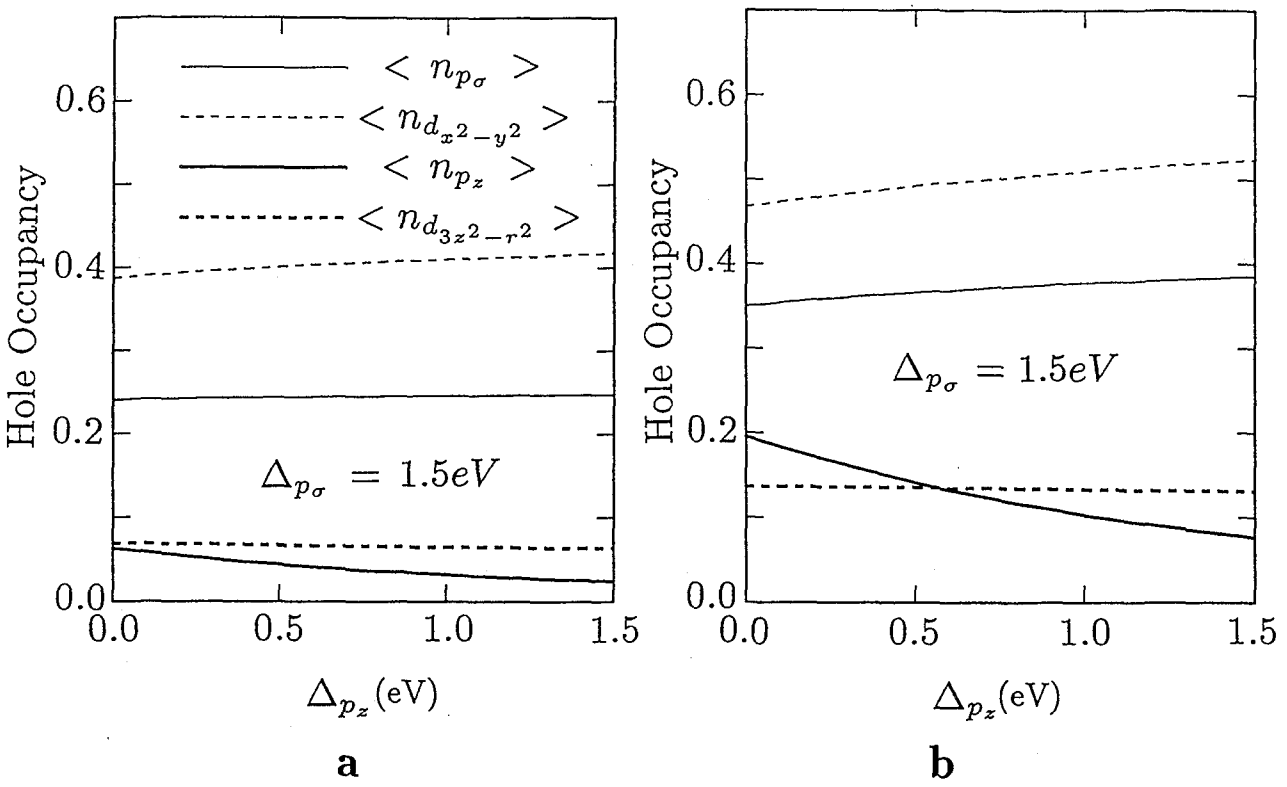

Fig. 3.3. The hole occupancy of each orbital in the Cu_4O_{12} cluster vs. Δ_{pz} when $\Delta_{p\sigma} = 1.5$eV. (**a**) The case of 4 holes. (**b**) The case of 6 holes.

§3.3 The Hole Occupancy

Figure 3.3a plots the hole occupancy of each orbital as a function of Δ_{pz} when there are 4 holes in the Cu_4O_{12} cluster; the charge transfer energy $\Delta_{p\sigma}$ is taken to be 1.5eV. The average hole density of the whole system, a hole per a Cu atom, corresponds to the high-T_C compounds without doping. The holes are mainly in oxygen p_σ and Cu $d(x^2-y^2)$ orbitals. The hole occupancy is not sensitive to Δ_{pz}, since $\langle n_{pz} \rangle$, the hole occupancy of the apex oxygen, remains small. We present in Fig. 3.3b the result for the case of 6 holes in the cluster with $\Delta_{p\sigma} = 1.5$eV, where the average hole density corresponds to 50% doped high-T_C compounds. The occupancies $\langle n_{pz} \rangle$ and $\langle n_{d(3z^2-r^2)} \rangle$ are more than 6/4 times as large as those of the 4 hole case.(Fig. 3.3b) This behavior of the hole occupancy seems to reflect the effect of the intra-atomic Coulomb energy of p_σ and $d(x^2-y^2)$ orbitals.

We plot the difference between the hole occupancies shown in Figs. 3.3a and 3.3b against Δ_{pz} in Fig. 3.4a, regarding the difference as the additional hole occupancies in the system with 6 holes. About 60% of the additional holes enter the oxygen p orbitals

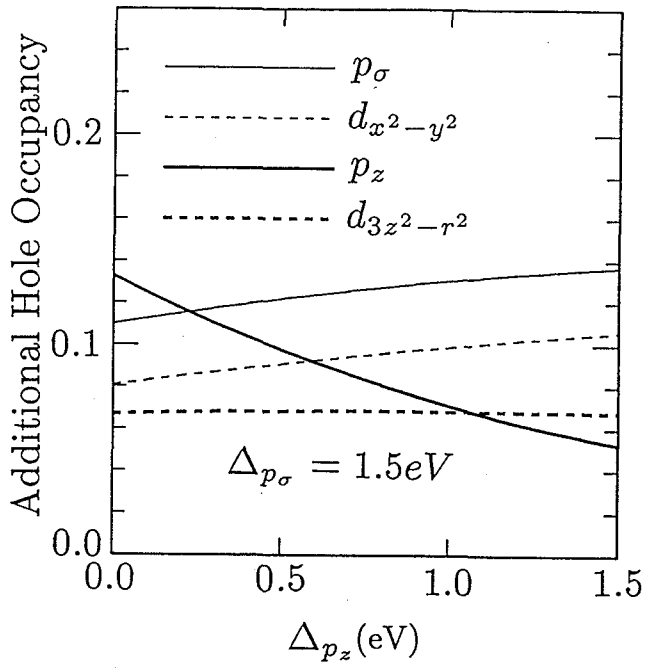

Fig. 3.4. The difference of the hole occupancy between the 6 hole and the 4 hole cases. (**a**) $\Delta_{p\sigma} = 1.5$eV. (**b**) $\Delta_{p\sigma} = 2.5$eV.

↑
a

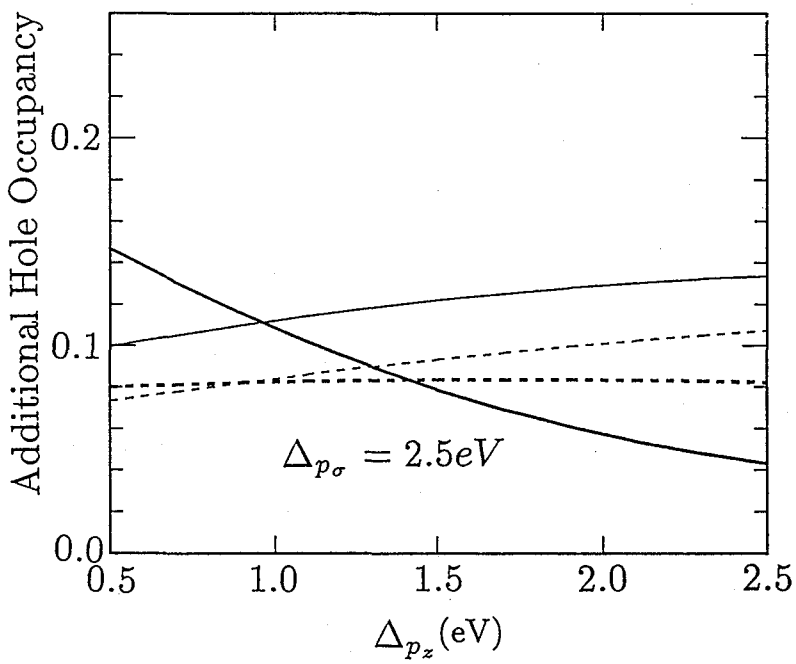

← **b**

throughout the parameter range whereas the additional hole occupancy in p_z orbital decreases with Δ_{pz}. (Note that p_σ orbitals are twice as many as p_z orbitals. The sum of additional hole occupancies in p_σ orbitals is always greater than that of p_z orbitals.) Figure 3.4(b) shows the additional hole occupancies with $\Delta_{p\sigma} = 2.5$eV. The effect of

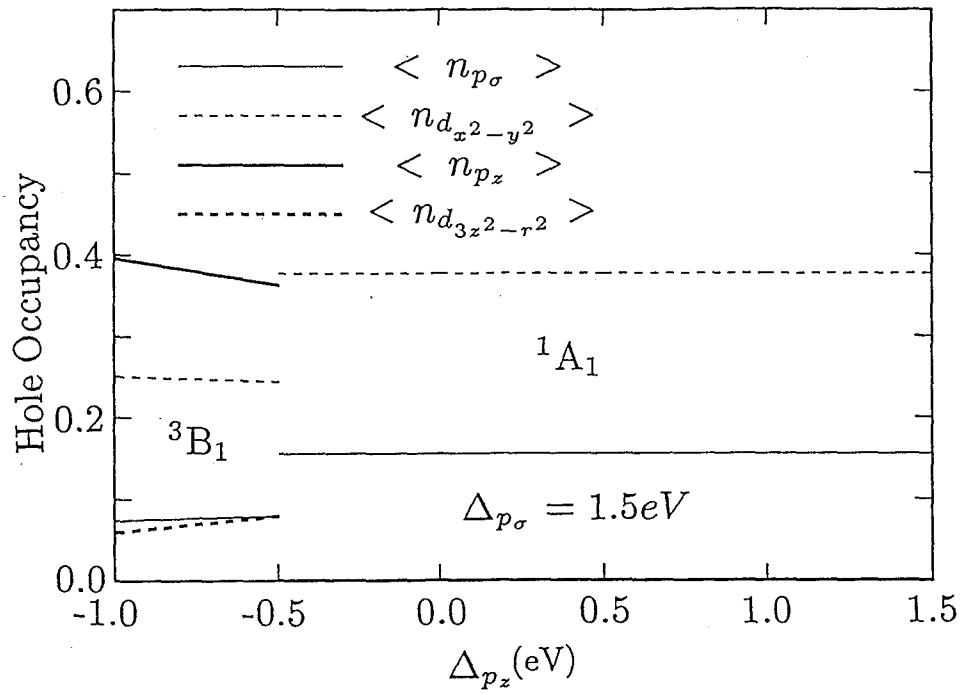

Fig. 3.5. The hole occupancies in the single CuO_5 cluster when $\Delta_{p\sigma} = 1.5$eV. The symmetry of the ground state wave function changes from $^1A_1$ to $^3B_1$ at $\Delta_{pz} = -0.5$eV.

Δ_{pz} on the additional hole occupancy in p_z orbitals appears more clearly than in the case of Fig. 3.4(a), but no qualitative change is apparent.

We also calculate the ground state of a CuO_5 cluster with 2 holes for comparison with the Cu_4O_{12} cluster.(Fig. 3.5) Although Cu $d\varepsilon$ orbitals are neglected, the behavior of the hole occupancy and the total spin of the cluster agree with those obtained by Fujimori who treats all Cu d orbitals.[2] The ground state changes from the $^1A_1$ state to the $^3B_1$ one at $\Delta_{pz} = -0.5$eV and the hole occupancies are discontinuous there. This transition is due to the geometry or the point group symmetry of the CuO_5 cluster; the ground state changes continuously in our Cu_4O_{12} model. As will be shown in Table III.I, however, no indication of the appearance of the $^3B_1$ is found in the present calculation of the Cu_4O_{12} cluster even with $\Delta_{pz} = -0.5$eV.

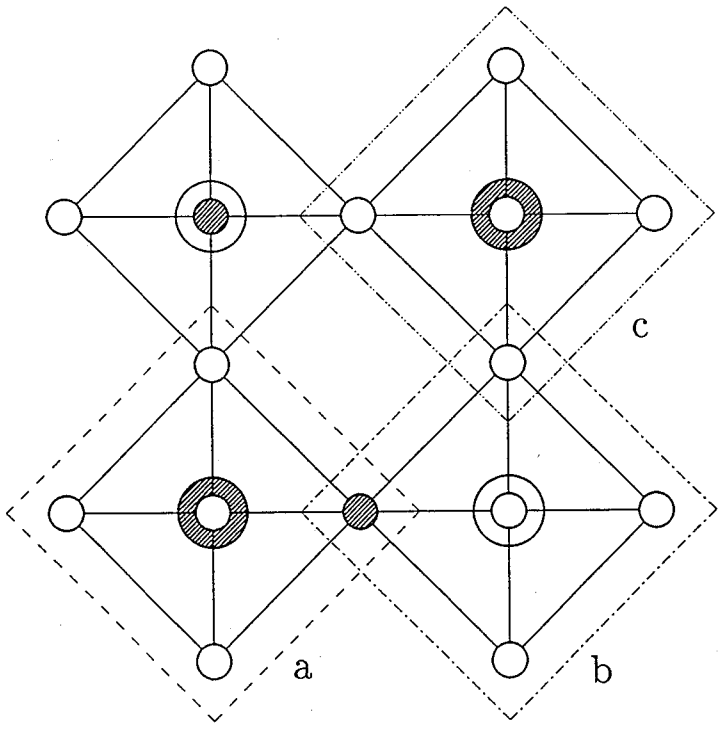

Fig. 3.6. A bird's-eye view of figure 1 and an example of the hole distribution. In the examples, each atom occupied by a hole is shaded; Therefore the a, b and c CuO_5 sub-cluster contains 2, 1 and 1 holes, respectively.

§3.4 Hole Number and Spin of a CuO_5 cluster in the Cu_4O_{12} Cluster

We can take the Cu_4O_{12} cluster for a superposition of four CuO_5 clusters as far as the atomic arrangement of the cluster is concerned. (Fig. 3.6) It is not easy, however, to pinpoint the difference of the electronic states between the Cu_4O_{12} cluster and the CuO_5 one. Thus we focus our attention on a CuO_5 unit in the Cu_4O_{12} cluster which we call 'a CuO_5 sub-cluster' to avoid a confusion with the isolated CuO_5 cluster assumed in the previous calculations. Then we calculate several quantities pertaining to the sub-cluster with the ground state wave function of the Cu_4O_{12} cluster.

We obtain the spin expectation value $\langle \mathbf{S}^2 \rangle = \langle (\sum_i \mathbf{S}_i)^2 \rangle$ of a CuO_5 sub-cluster where $\mathbf{S}_i$ is a spin operator on site i,(fine dotted line in Fig. 3.7) and probabilities $P(n,m)$ of finding n holes in the same cluster with total spin m where $0 < n < 3$ and $0 < m < n/2$. When there are 4 holes in the Cu_4O_{12} cluster and $\Delta_{p\sigma} = 1.5\text{eV}$, the spin expectation value $\langle \mathbf{S}^2 \rangle$ is approximately equal to 3/4 which is the value if the hole number in the CuO_5 sub-cluster is strictly kept to be one. However, the probability of finding a hole in the cluster, P(1,1/2) is less than 1/2.(thin solid line in Fig. 3.7a) This apparent discrepancy is due to the fact that the states of two holes in the sub-cluster appear easily since an

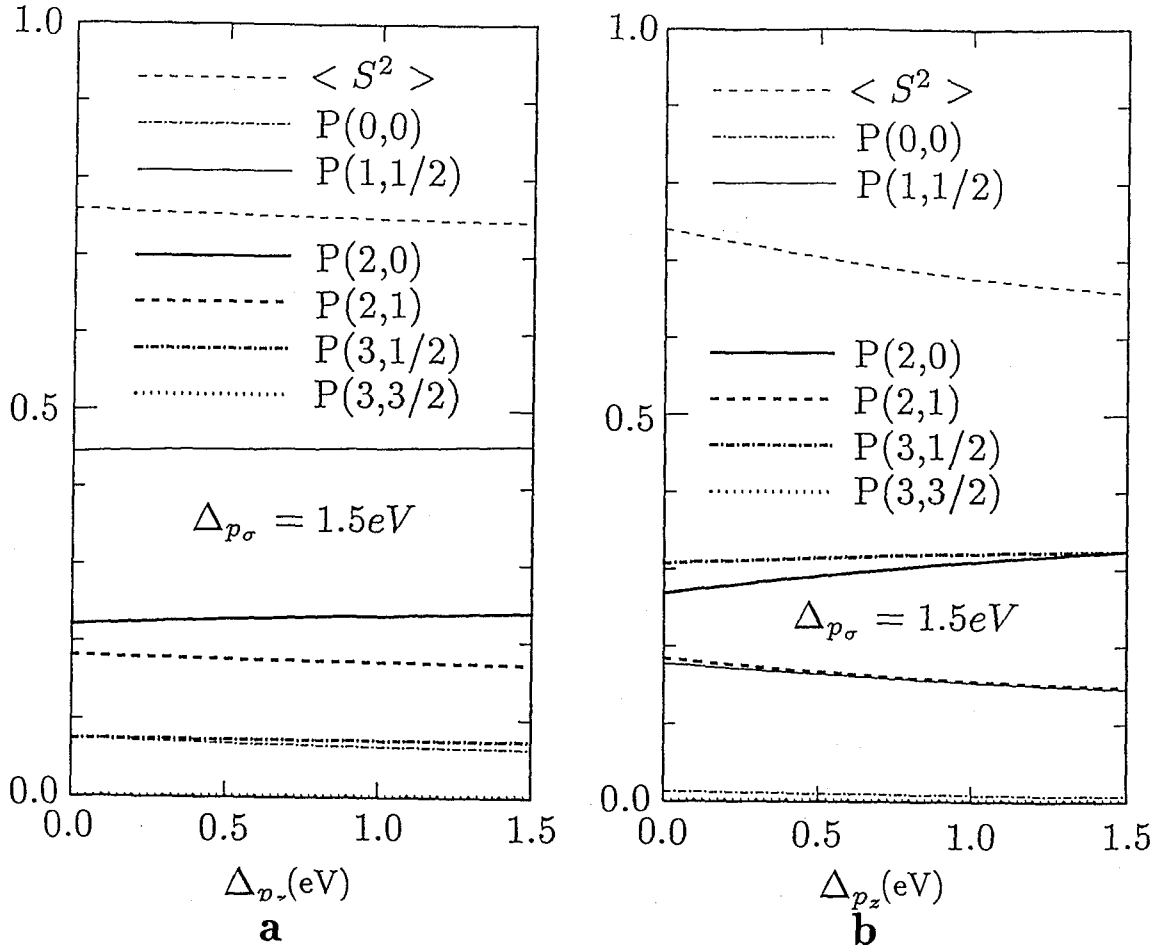

Fig. 3.7. The expectation value of the total spin of a sub-cluster, $\langle \mathbf{S}^2 \rangle$ and the probability of finding n holes in the cluster with total spin m, P(n,m). (a) The 4 hole case. (b) The 6 hole case.

in-plane oxygen is shared by two CuO_5 clusters.(see the cluster a in Fig. 3.6) When there are two holes in the sub-cluster, the probability P(2,0) is greater than the probability P(2,1), reflecting the singlet correlation between the Cu and in-plane oxygen atoms, and the super-exchange interaction between neighboring Cu atoms. Note that the appearance of the triplet state is an effect of the intercluster transfer which is not taken into account in the treatment assuming an isolated CuO_5 cluster.

Figure 3.7**b** shows the total spin $\langle \mathbf{S}^2 \rangle$ and the probability P(n,m) for the case of 6 holes in the Cu_4O_{12} cluster. The increase of the total spin $\langle \mathbf{S}^2 \rangle$ and the probability P(2,1) with decreasing Δ_{pz} might look a precursor to the change of the total spin of the ordinary CuO_5 cluster from the $^1A_1$ to the $^3B_1$. The increasing rate of these quantities is, however, rather small compared with that of the additional hole occupancy in p_z orbitals,

Table III.I.

The spin correlations among Cu and oxygen atoms when $\Delta_{p\sigma} = 1.5$eV. $\mathbf{S}_{\mathrm{Cu}}$ is the total spin of a Cu atom defined by $\mathbf{S}_{\mathrm{Cu}} = \mathbf{S}_{d(3z^2-r^2)} + \mathbf{S}_{d(x^2-y^2)}$; n_{Cu} is the total number of holes of a Cu atom defined by $n_{\mathrm{Cu}} = n_{d(3z^2-r^2)} + n_{d(x^2-y^2)}$. The expectation value $\langle \mathbf{S}_{\mathrm{Cu}} \cdot \mathbf{S}_{\mathrm{Cu}'} \rangle$ is a spin correlation function between nearest neighboring Cu atoms.

	CuO_5 Cluster (2 holes)		Cu_4O_{12} Cluster (6 holes)		
Δ_{pz}	-1.0eV ($^3B_1$)	0.5eV ($^1A_1$)	-0.5eV	0.0eV	0.5eV
$\frac{\langle \boldsymbol{S}_{\mathrm{Cu}} \cdot \boldsymbol{S}_{\mathrm{Cu}} \rangle}{\langle n_{\mathrm{Cu}} \rangle}$	0.713	0.594	0.629	0.632	0.633
$\frac{\langle \boldsymbol{S}_{\mathrm{Cu}} \cdot \boldsymbol{S}_{p_\sigma} \rangle}{\langle n_{\mathrm{Cu}} \rangle}$	0.013	-0.148	-0.080	-0.086	-0.091
$\frac{\langle \boldsymbol{S}_{\mathrm{Cu}} \cdot \boldsymbol{S}_{p_z} \rangle}{\langle n_{\mathrm{Cu}} \rangle}$	0.1693	0.0000	-0.011	-0.0080	-0.0055
$\frac{\langle \boldsymbol{S}_{\mathrm{Cu}} \cdot \boldsymbol{S}_{\mathrm{Cu}'} \rangle}{\langle n_{\mathrm{Cu}'} \rangle}$	—	—	-0.095	-0.098	-0.100

indicating that the holes in the latter orbitals are not necessarily associated with the $^3B_1$ state of the CuO_5 cluster.

We calculate the spin correlations to check whether the probability P(2,1) represents the appearance of the local $^3B_1$ state or not.(Table III.I) Since the hole occupancy in p_z orbitals is equal to zero in the $^1A_1$ state of a single CuO_5 cluster calculation,(see Fig. 3.5) the hole in p_z orbital in that calculation is associated with the $^3B_1$ in which it has inevitably a strong ferromagnetic coupling with the Cu spin just below. In our calculation, however, the value of $\langle \mathbf{S}_{\mathrm{Cu}} \cdot \mathbf{S}_{p_z} \rangle / \langle n_{\mathrm{Cu}} \rangle$ which represents the spin correlation between a p_z orbital and a Cu atom just below is small and negative even with $\Delta_{pz} = -0.5$eV where the ordinary CuO_5 cluster changes its ground state symmetry. The behavior of this spin correlation means that the finite hole occupancy in p_z orbital is not associated with the local $^3B_1$ state. Thus a finite value of the probability P(2,1) arises from the holes in in-plane oxygens.

From the facts described above, we conclude that the ground state wave function of the ordinary CuO_5 is too severely restricted by the point group symmetry of the cluster.

§3.5 Conclusion

We have studied the Cu_4O_{12} cluster and compared it with the ordinary CuO_5 cluster to investigate the effect of the intercluster hole transfer. We conclude from the analysis of the hole distribution and spin correlations that the pyramidal plane cannot be treated as an assembly of independent CuO_5 clusters even when we discuss the electronic structure of a single unit of them. Since the intercluster hole transfer generates off-diagonal matrix elements between different representations of the point groups at neighboring CuO_5 clusters, we have to include excited states if we represent the ground state wave function of the pyramidal plane by use of the wave functions of the single CuO_5 cluster. In consequence the ground state changes gradually with the parameter Δ_{pz}.

The additional holes due to doping are not in a definite orbital but distributed in all orbitals rather evenly; two thirds of them enter the oxygen atoms. We may treat the pyramidal plane as a concentrated Kondo system,[10,11] but there are some points to be noticed:

(i) A part of the holes enter the p_z orbital of the apex oxygen, where practically no magnetic coupling with the Cu atoms appears.

(ii) The Coulomb repulsion energy between the additional holes is not the bare intra-atomic Coulomb energy of the oxygen p orbital, because there are some holes in p orbitals even in the undoped system.

We will discuss in the next chapter the XAS and XPS spectra on the basis of the present analysis of the ground state of the pyramidal plane. It will be interesting to see whether the intercluster transfer together with many body effects will modify the conclusions so far drawn from the analyses based on single $CuO_{5(6)}$ cluster or impurity Anderson models. Actually, the intercluster transfer can give rise to a new feature in the XAS and XPS spectra.

References

1) H. Eskes and G. A. Sawatzky: Phys. Rev. Lett. **61** (1988) 1415.
2) A. Fujimori: Phys. Rev. **B 39** (1988) 793.
3) A. Fujimori, E. Takayama-Muromachi, Y. Uchida and B. Okai: Phys. Rev. **B 35** (1988) 814.
4) K. Okada and A. Kotani: J. Phys. Soc. Jpn. **58** (1989) 1095.
5) T. Tohyama, Y. Ohta and S. Maekawa: preprint.
6) W. A. Harrison: *Electronic Structure and the Properties of Solids* (Freeman, Sanfrancisco, 1980) p. 441.
7) A. K. McMahan, R. M. Martin and S. Satpathy: Phys. Rev. **B 38** (1988) 6650.
8) F. Mila: Phys. Rev. **B 38** (1988) 11358.
9) C. Lanczos: J. Res. Nat. Bur. Standards **45** (1950) 255.
10) M. Imada, N. Nagaosa and Y. Hatsugai: J. Phys. Soc. Jpn. **57** (1988) 2901.
11) M. Ogata and H. Shiba: J. Phys. Soc. Jpn. **57** (1988) 3074.
12) Y. Kuramoto and H. J.Schmidt: *Strong Correlation and Superconductivity,* eds. H. Fukuyama, S. Maekawa and A. P. Malozemoff (springer, Berlin, 1989) p. 88.
13) V. Heine: *Solid State Physics* vol. **35**, eds. H. Ehrenreich, F. Seitz and D. Turnbull (Academic Press, New York, 1980) p. 87.

Chapter IV
Effect of Hole Itinerancy on XAS and XPS Spectra of the High-T_c Compounds

§4.1 Introduction

Since the discovery of the high-T_c superconductors, many X–ray emission and absorption spectroscopy measurements on these compounds and related metal oxides have been performed[1,2] to investigate the electronic structure of the CuO_2 plane. The XPS and XAS spectra of stoichiometric compounds which are insulating differ from those of non-stoiciometric ones which are metallic;[3] this phenomenon indicates that the presence of valence holes affects the spectra. It is obvious that we need to take into account the correlation among holes and their itinerancy in order to discuss such an effect.

In the last chapter we investigated the ground state wave function of the Cu_4O_{12} cluster with periodic boundary condition which is one of the smallest replicas of the CuO_2 pyramidal plane. We found that the ground state of this periodic cluster is different from that of a single Cu atom cluster (CuO_5) in many respects.[4] For example, the ground state wave function of the periodic cluster is not governed by the local point symmetry group of the configuration of oxygen atoms around a Cu atom, because the symmetry of the ground state wave function is violated by the inter-copper hole transfer through in-plane oxygen atoms.

Thus it is necessary for investigating the effects of the hole correlation and itinerancy to carry out calculations for extended clusters containing more-than-one Cu atoms. Such calculations for the valence band XPS and BIS spectra have been made so far by two groups. Balseiro, Avignon and Gagliano[5] calculated the valence band XPS spectra of a Cu_4O_8 cluster by use of the modified Lanczos method proposed by Gagliano and Balseiro[6] with the result that the stoichiometric system with one hole per Cu atom is the charge transfer insulator. They also calculated the spectra of hole or electron doped systems to discuss the difference of the spectra near the Fermi energy. On the other hand, Kuramoto and Schmidt[7] calculated the angle resolved XPS and BIS spectra of the same

stoichiometric and electron or hole doped Cu_4O_8 clusters, using also the modified Lanczos method; compared with the result of the tight binding band calculation, their result indicated a narrowing of the band width and the appearance of new peaks on the high energy side both due to the correlation.

In this chapter we extend the calculation by the modified Lanczos method to the Cu $2p$ core level XPS and XAS spectra which have been discussed so far by use of the impurity Anderson model[8] or single Cu cluster $CuO_n(n = 5, 6)$[9] models. The following clusters are assumed: two clusters in which Cu atoms are arrayed two dimensionally, Cu_4O_8 with periodic boundary condition and Cu_5O_{16} with open boundary condition, one-dimensional linear clusters with open ends Cu_nO_{n+1} with n ranging up to 7 and two linear chains with the periodic boundary condition, Cu_4O_4 and Cu_6O_6. The valence band XPS and BIS spectra of the one-dimensional clusters are also calculated to check the dependence on size and geometry.

In the next section (§4.2) the method of calculating the XAS and XPS spectra is explained. In §4.3,§4.4 and §4.5 the results are presented for the Cu $2p$ XPS, Cu $2p$ XAS and valence band XPS spectra, respectively. In §4.6 conclusions are summarized.

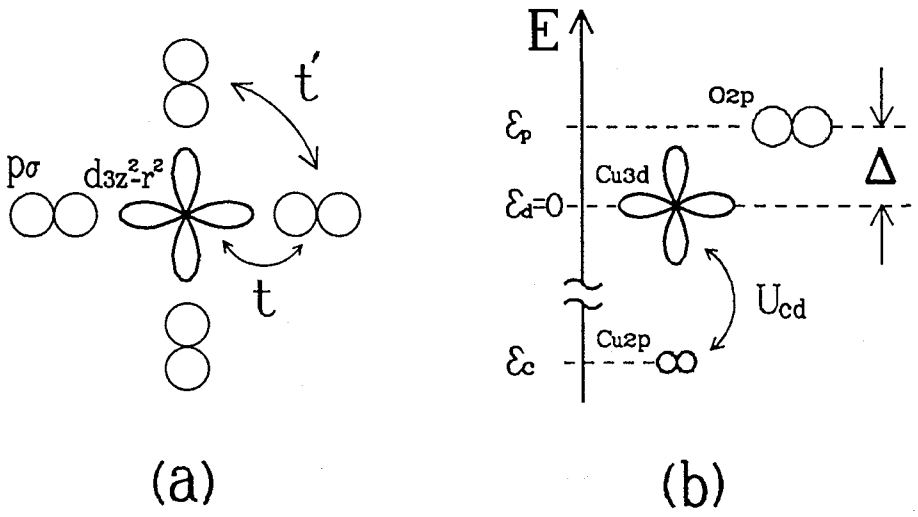

Fig. 4.1 Atomic orbitals and related parameters: (**a**) Configuration of atomic orbitals. (**b**) One hole energy levels. The parameters Δ and U_{cd} are the charge transfer energy and the Coulomb energy between a core and a valence hole, respectively.

§4.2 Method of Calculation on XAS and XPS Spectra

We adopt the d-p model[10] as the model for the CuO_2 plane in order to treat the hole itinerancy. The Hamiltonian of the d-p model written in the creation, annihilation and number operators of holes is given by

$$H_{d-p} = t \sum_{<pd>\sigma} (c^{\dagger}_{p\sigma} c_{d\sigma} + c^{\dagger}_{d\sigma} c_{p\sigma}) - t' \sum_{<pp'>\sigma} c^{\dagger}_{p\sigma} c_{p'\sigma}$$

$$+ \Delta \sum_{p\sigma} n_{p\sigma} + U_p \sum_{p} n_{p\uparrow} n_{p\downarrow} + U_d \sum_{d} n_{d\uparrow} n_{d\downarrow} , \qquad (4.1)$$

where the indices p (or p') and d are labels of oxygen $p\sigma$ orbitals and Cu $d(x^2 - y^2)$ orbitals, respectively. The first two terms of the right hand side of eq. 4.1 are valence band energies of holes, where t and t' are the hole transfer energy between Cu and oxygen atoms and that between oxygen atoms, respectively.(Fig. 4.1a) The charge transfer energy Δ is the one hole energy difference between Cu and oxygen atoms

$$\Delta = \varepsilon_p - \varepsilon_d \, . \qquad (4.2)$$

The one hole energy ε_d is taken to be zero, i.e., Δ is the same as ε_p. (See Fig. 4.1b.) The last two terms are the intra-atomic Coulomb energies between valence holes in Cu and O atoms, respectively, with U_p and U_d are representing the Coulomb integrals.

When we calculate the core level XPS or XAS spectra of the Cu atom, we have to add the core hole energy and the Coulomb energy between a core hole and the valence holes

$$H' = \varepsilon_c n_c + U_{cd} n_c n_d \tag{4.3}$$

to the Hamiltonian H_{d-p}, where the operators $n_c = n_{c\uparrow} + n_{c\downarrow}$ and $n_d = n_{d\uparrow} + n_{d\downarrow}$ are core and valence hole number operators of the photo-excited Cu atom, respectively. We neglect the spin orbit interaction for the core orbital and the orbital dependence of the Coulomb energy U_{cd}, because our aim is not to analyze these effects on the spectra but to discuss the effect of hole itinerancy and correlation on them. The number of basis states of the system is considerably reduced by this simplification.

The spectral intensity $I(\omega)$ of the Cu $2p$ XPS is expressed by use of the total Hamiltonian $H = H_{d-p} + H'$ as

$$I(\omega) = -\frac{1}{\pi} Im\langle g | c_c \frac{1}{\omega - H + E_g} c_c^\dagger | g \rangle \,, \tag{4.4}$$

where $c_c^\dagger$ is a core hole creation operator and ω is the binding energy. If an imaginary part $\Gamma = Im(\omega)$ is introduced in the denominator, then a convolution with the Lorenzian whose half width is Γ is obtained. The initial state $|g\rangle$ is the ground state of the Hamiltonian H with no core hole; it is, therefore, also the ground state of H_{d-p} where the ground state energy is E_g. If we replace the operator $c_c^\dagger$ by $c_d c_c^\dagger$ or $c_{d(p)}^\dagger$ or $c_{d(p)}$, then we obtain Cu $2p$ XAS or valence band XPS or BIS spectra, respectively. (Note that the physical interpretation of $I(\omega)$ and ω depends on the type of spectroscopy.) In every case, the inter-atomic transfers t and t' enable valence holes to escape from the photo-excited site so as to cause an energy relaxation, which results in a change in the spectrum $I(\omega)$.

We calculate the XPS and XAS spectra by use of relatively large Cu_nO_m clusters (Fig. 4.2a) with periodic or free boundary condition. The system size has to be larger than the relaxation range of the valence holes. In order to examine the size dependence of the results, we employ one-dimensional Cu_nO_{n+1} chains or Cu_nO_n rings (Fig. 4.2b) for which the calculation is feasible for larger linear dimension than for the two-dimensional

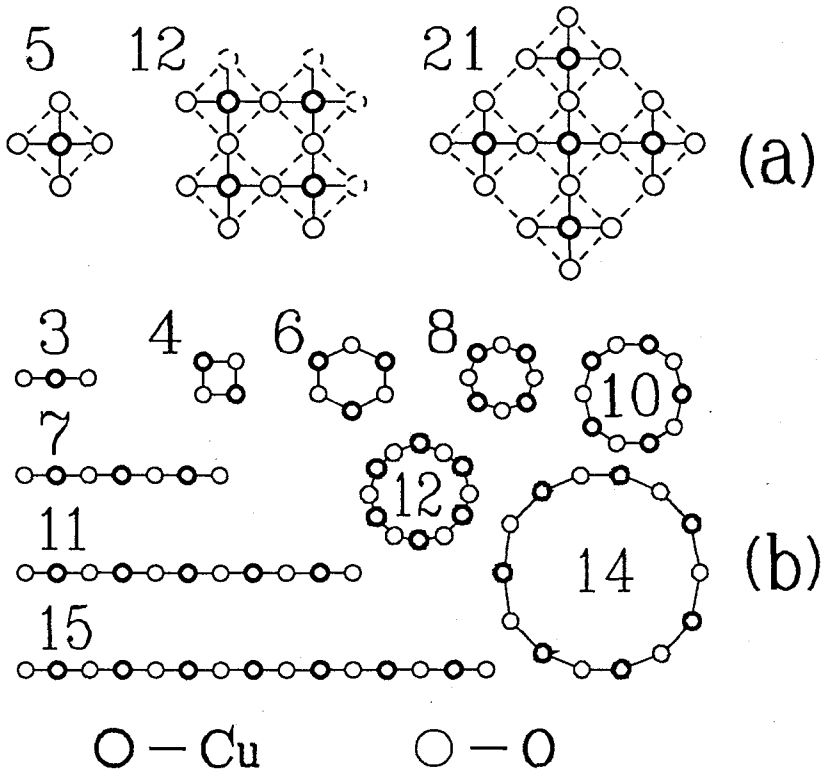

Fig. 4.2 The employed clusters:
(**a**) The two-dimensional clusters. The CuO_4 and Cu_5O_{16} clusters have open boundary, and the periodic boundary condition is imposed on the Cu_5O_{16} cluster.
(**b**) The one-dimensional clusters. For linear chains, the central Cu atom or the nearest neighboring oxygen atoms to this Cu atom are excited in the calculation of the XPS and XAS spectra to reduce the boundary effect.

clusters. In the following we label the clusters by the total number of the atoms in them, for example, the Cu_4O_8 cluster is called the '12-site system'. We obtain the initial state $|g\rangle$ by use of the Lanczos method[11] and calculate the spectral intensity $I(\omega)$ by use of the modified Lanczos method proposed by Gagliano and Balseiro[5]; the algorithm of this method is the same as that of the well known recursion method[12]. For small clusters, we also calculate the spectrum by the exact diagonalizaton of the Hamiltonian $H = H_{d-p} + H'$ to identify the final states. The convergence of the modified Lanczos method is checked also by this calculation.

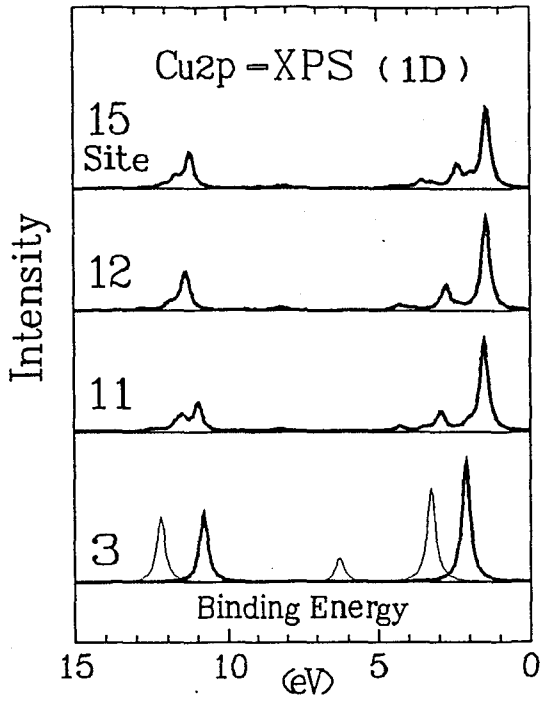

Fig. 4.3. The Cu $2p$ XPS spectra of the one-dimensional systems when there is one valence hole per Cu atom. For the 3-site system (CuO_2), the two-hole case is also shown by the fine line.

§4.3 Cu $2p$ XPS Spectra

Figure 4.3 shows Cu $2p$ core level XPS spectra of the one-dimensional clusters with the parameters $U_d = 6.0\text{eV}$, $U_p = 3.0\text{eV}$, $U_{cd} = U_d/0.7 = 8.6\text{eV}$, $t = 1.5\text{eV}$, and $\Delta = 1.0\text{eV}$[9,13] for the stoichiometric case where one hole per Cu atom is assumed. For the one-dimensional systems, the direct transfer between oxygen atoms t' is taken to be zero. The spectrum with two holes in it for the CuO_2 cluster is also shown by the fine line. Since the core hole energy ε_c is irrelevant to the shape of the spectra, only the relative binding energy defined by $Re(\omega) - \varepsilon_c$ is shown on the horizontal axis. We set the parameter Γ for 0.16eV; the value is selected to secure a rapid convergence in the modified Lanczos method.

The spectrum of the CuO_2 cluster with a valence hole has simple two peak structure. The main peak and the satellite one correspond to the final states whose electron configurations are represented mainly by $|\underline{c}d^{10}\underline{L}\rangle$ and $|\underline{c}d^{9}\rangle$, respectively. The interval between these peaks, 9eV is roughly given by the sum of the Coulomb and transfer energies $U_{cd} + c \cdot 2t$, where the constant c is of the order of unity. Note that the state $|\underline{c}d^{9}\rangle$ giving rise to the satellite peak corresponds to the bound state of two holes in which the transfer contributes to an increase of its energy. The peak interval of the CuO_2 cluster is smaller

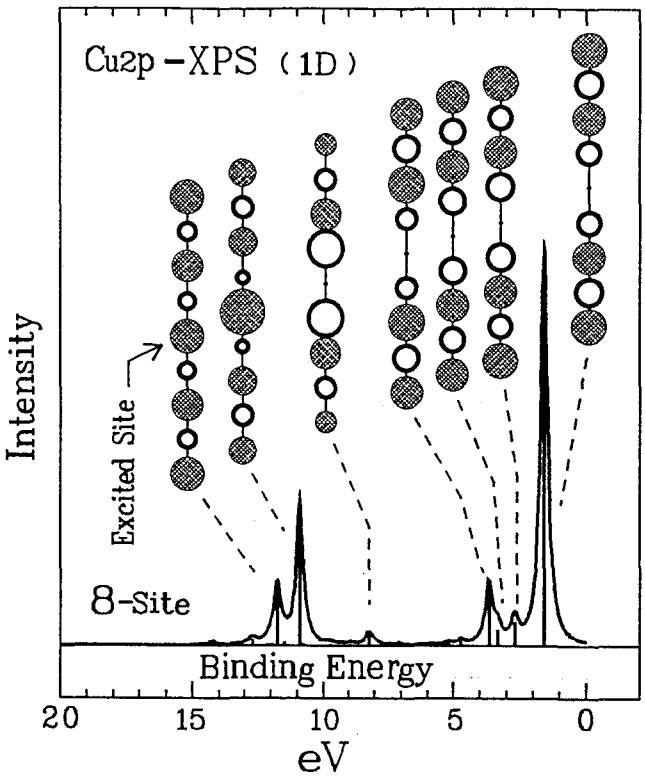

Fig. 4.4. The Cu $2p$ XPS spectra of the 8-site system. The vertical lines denote the spectrum $I(\omega)$ obtained by the exact diagonalization of the final state Hamiltonian. The radii of open and meshed circles represent the oxygen and Cu hole densities, respectively, for each final state. The central Cu atom corresponds to the excited site. The top and bottom meshed circles are the hole density of the same Cu atom.

than those of the larger clusters, since this contribution of the transfer is reduced by the smallness of the cluster size.

The main and satellite peaks of the spectra of the larger clusters show multiple peak structures on their high energy sides, which indicate the variety of the valence hole configurations in the final states. In other words, there are various ways of the valence hole relaxation in the final states. We note also the appearance of a group of small peaks within the range 8eV to 9eV in between the main peak and the satellite one. In order to make a quantitative check of the validity of the assignment of the main and satellite peaks to the $|\underline{c}d^{10}\underline{L}\rangle$ and $|\underline{c}d^{9}\rangle$ final states for larger clusters than CuO_2 and also to elucidate the origin of the new peak, we calculated the final state wave functions of the 8 site linear cluster by the exact diagonalization of the Hamiltonian $H = H_{d-p} + H'$. The computational difficulty forces us to adopt this size of the cluster in this analysis. In spite of the smallness of the size, the XPS spectrum of the 8-site system which is shown in Fig. 4.4 is similar to those of the 11-, 12- and 15-site systems shown in Fig. 4.3, showing the three group structure. Figure 4.4 shows the XPS spectra as well as the hole distribution in the final state of principal peaks, where the radii of open and meshed circles denote the

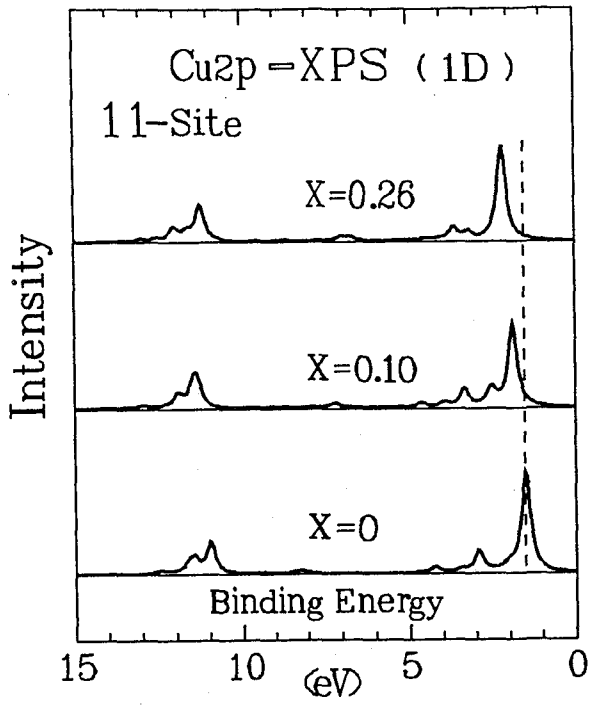

Fig. 4.5. The Cu $2p$ XPS spectra of 11-site system with 5,6, and 7 holes, where the additional hole densities are $X = 0$, 0.2 and 0.4, respectively.

hole densities of O and Cu atoms, respectively. The final states which are between 0 and 5eV have the $|\underline{c}d^{10}\underline{L}\rangle$ character. The hole distributions in them are quite similar to each other. The calculation shows clearly also that the satellite peaks on the left correspond to the $|\underline{c}d^{9}\rangle$ final state.

The hole distribution in the final states of the new peak in between the main peak and the satellite one is quite interesting, since the hole density of the oxygen atoms which are at the nearest neighboring sites of the excited Cu atom is the largest. The distribution indicates that the final state may be represented by the $|\underline{c}d^{10}\underline{L}^2\rangle$ configuration, though there are no extra holes in the system. The hole itinerancy gives rise to the $|d^{10}\underline{L}^2\rangle$ configuration in the initial state which amounts to 0.082. The relative intensity of the $|\underline{c}d^{10}\underline{L}^2\rangle$ peak is somewhat smaller than this ratio. It may arise from the fact that the differences in the hole configuration of the ligand states comprised by $\underline{L}^2$ between $|\underline{c}d^{10}\underline{L}^2\rangle$ and $|d^{10}\underline{L}^2\rangle$ states give rise to a reduction of the overlap integral.

In Fig. 4.5 we show a calculation which demonstrates the dependence on the concentration of additional holes. It gives the XPS spectra of the 11 site system containing five Cu atoms with 5, 6, and 7 holes which correspond to the additional hole density $X =$ 0, 0.2 and 0.4, respectively. The location of the main peak shifts towards higher binding

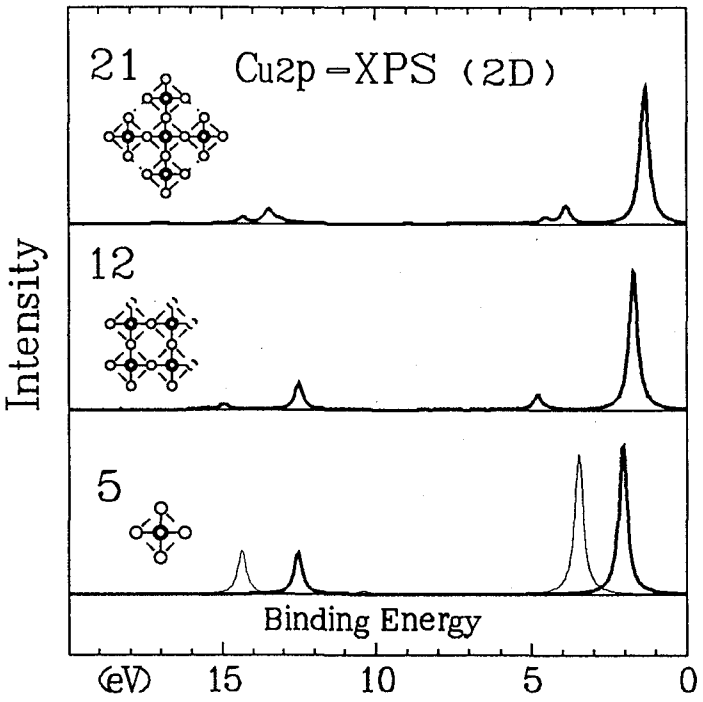

Fig. 4.6. The Cu $2p$ XPS spectra of the two dimensional clusters when there is one hole per Cu atom. For the CuO_4 cluster, the two holes case is also shown by the fine line.

energy with increasing X in agreement with the experimental data obtained by Flavell and Egdell.[3] Though it is difficult to make a quantitative comparison, the calculated shifts are of the same order of magnitude as the observed ones. This peak shift which we obtain for other clusters as well can be ascribed to an increase of the band energy cost required to exclude the valence holes from the excited Cu atom. Note also that the intensity of the $|\underline{c}d^{10}\underline{L}^2\rangle$ peak increases with the density X. Since the presence of the additional holes enhances the component of the $|d^{10}\underline{L}^2\rangle$ configuration in the initial state, the increase of the peak intensity can be expected.

Figure 4.6 shows the XPS spectra of the two-dimensional clusters when there is one hole per Cu atom. The parameters are the same as those of the one-dimensional clusters except that the additional parameter t' is taken to be 0.5eV.[9,13] The spectra are similar to those of the one-dimensional systems as a whole, but the structure of the spectra is rather simple. This difference may be due to smaller sizes of the two-dimensional clusters in linear dimension compared with those of the linear clusters. We note also that the intensity of the $|\underline{c}d^{10}\underline{L}^2\rangle$ peak is very weak and hard to see in this figure, though it is present.

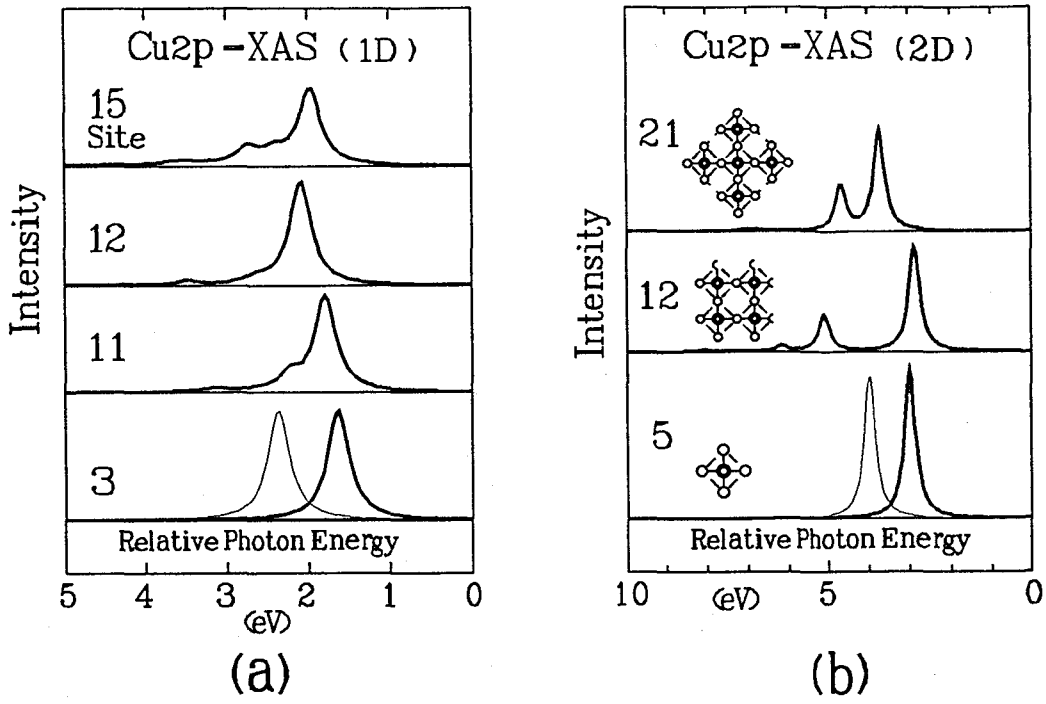

Fig. 4.7. The Cu $2p$ XAS spectra when there is a valence hole per Cu atom. For the CuO_2 and CuO_4 clusters, the two-hole case is also shown by the fine line. When an odd number of valence holes are present in the initial state, the calculation assumes that a hole of majority spin state is annihilated in the final state. (**a**) One-dimensional cases. (**b**) Two-dimensional cases.

§4.4 Cu $2p$ XAS Spectra

Let us glance over the process of Cu $2p$ XAS before analyzing the calculated spectra. A valence hole is annihilated by the excitation of a Cu $2p$ core electron. Then the valence hole configuration will be changed so as to relax this sudden change. The XAS spectrum should reflect this many body effect. The photon energy of a peak represents the difference between the final state energy and one hole energy of the annihilated hole. We cannot predict the direction of the peak shift with the concentration of the additional holes without detailed calculation, because both the final state energy and the energy of the valence hole in the initial state increase generally with additional holes to result in a partial cancellation.

Figure 4.7a shows Cu $2p$ XAS spectra of the one-dimensional clusters when there is one hole per Cu atom. For the CuO_2 cluster, the two hole case is also shown by a fine line. The parameters are the same as those of the XPS case. The tail of the main peak has a multiple peak structure, which looks like that of the XPS spectra. Existence

of the multiple peak structure is a common feature of the core level spectra of these large clusters. Experimentally, this structure is observed in several Cu oxides as a smooth tail of the peak on high energy side.[14] In the present calculation on the Cu $2p$ XAS spectra, the $|\underline{c}d^9\rangle$ and $|\underline{c}d^{10}\underline{L}^2\rangle$ peaks are not obtained. Figure 4.7b is the spectra of the two-dimensional CuO_4, Cu_4O_{12} and Cu_5O_{16} clusters when there is one hole per Cu atom. Compared with the cases of large linear clusters the number of peaks composing the tail part is small because of the smallness of the cluster in linear dimension.

The XAS spectra of one-dimensional systems with additional holes are also calculated. The direction of the peak shift, however, depends on the size of the clusters and the number of the valence holes. This uncertainty indicates the necessity of calculations with larger clusters.

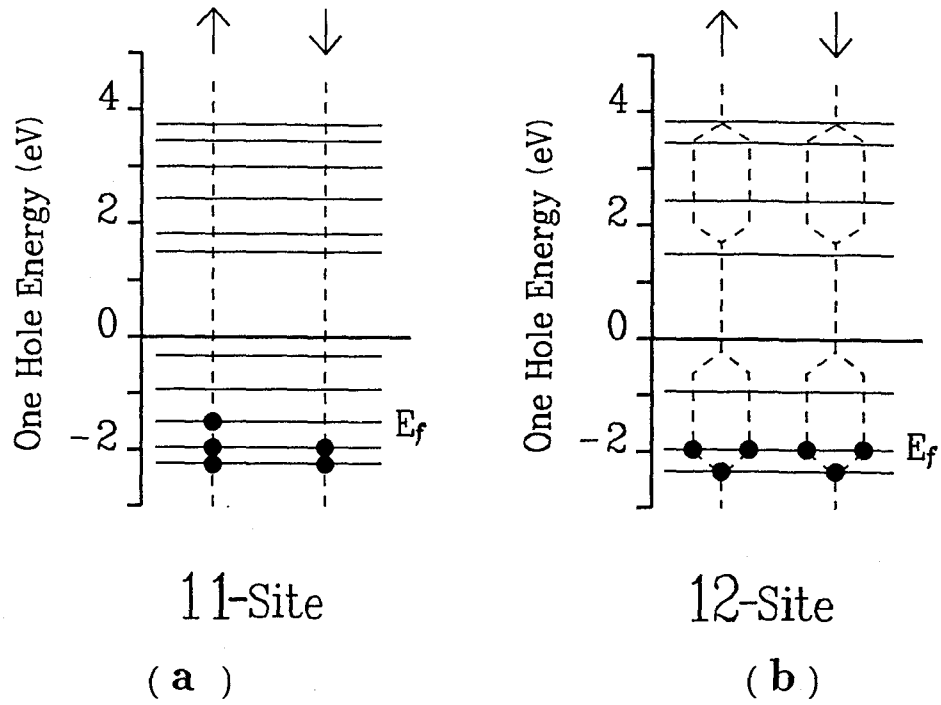

Fig. 4.8. One hole energy levels of 11- and 12-site system when there is no Coulomb interaction. If there is a hole per Cu atom, the 11-site cluster have open shell structure,(**b**) while the 12-site cluster have the closed one.(**a**)

§4.5 Valence Band XPS and BIS Spectra

The valence band X-ray photo-emission spectroscopy (valence band XPS) and the Bremsstrahlung isochromat spectroscopies (BIS) directly yield the DOS of empty and filled bands in the hole picture.[7] As was mentioned in §4.1, the valence band XPS of the Cu_4O_{12} cluster has been investigated by Balseiro, Avignon and Gagliano[5] and Kuramoto and Schmidt.[7] Since the linear dimension of the cluster adopted in their calculation is rather small, we calculated the spectra of one-dimensional systems with more than 7 atoms (Fig. 4.2b) to investigate the size dependence of the spectra. Here we present results for 7-, 8-, 11-, 12- and 15-site cases. The same values of the parameters t ,U_p and U_d as before, $t = 1.5\text{eV}$, $U_p = 3.0\text{eV}$ and $U_d = 6.0\text{eV}$ are assumed here, as far as we do not refer the values explicitly. We take a slightly large charge transfer energy, $\Delta = 1.5\text{eV}$ compared with the value used in previous sections in order to observe the charge transfer gap clearly.

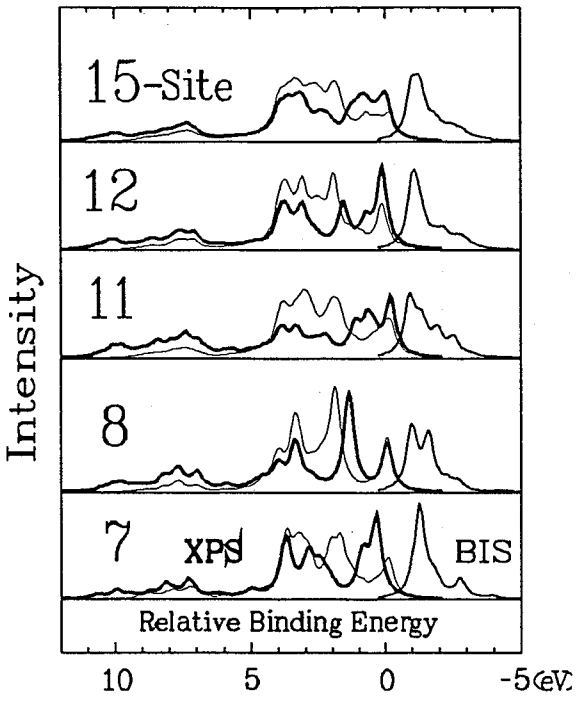

Fig. 4.9. Valence band XPS and BIS spectra of the one-dimensional systems when there is one hole per Cu atom. The thick and fine lines on the left hand side are the valence band XPS spectra by a hole creation at Cu $3d$ and O $p\sigma$, respectively. The right hand side shows the BIS spectra by a Cu hole removal.

Note that the degeneracy of the initial state depends on both the cluster size and the hole number in the clusters. Figure 4.8 shows the one-particle energy level of 11- and 12-site clusters when there is no Coulomb repulsion. If there is a hole per Cu atom, the 11-site cluster has open shell structure, while the 12-site cluster the closed one. Such a finite size effect is always present as far as we adopt the finite size systems even when there is finite Coulomb interaction and therefore we have to pay attention to the size effect.

Figure 4.9 shows BIS and valence band XPS spectra of the systems when there is one hole per Cu atom. The thick and fine lines on the left hand side are the valence band XPS spectra by a copper and oxygen hole creation, respectively. The right hand side shows the BIS spectra by a Cu hole removal. The separation between the Fermi edges of the XPS and BIS spectra is of the order of the charge transfer energy Δ, which indicates that these systems may be classified as the charge transfer insulator.

It is not clear that what part of the spectra in Fig. 4.9 represents the electron correlation effect that comes from the intra-atomic Coulomb repulsion. We therefore observe the spectra by gradually imposing the Coulomb interaction. Fig. 4.10 shows the spectra of 11- and 12-site systems when there is a hole per Cu atom (a, b) and when there are two additional holes.(c) The relation $U_p = U_d/2$ is always assumed. It should be noted that the spectra are not modified so much within the range $5\text{eV} > E_b > -2\text{eV}$ except for the

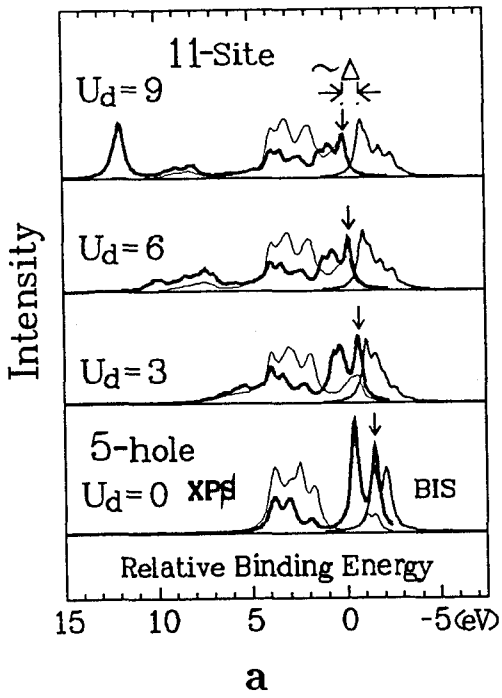

a

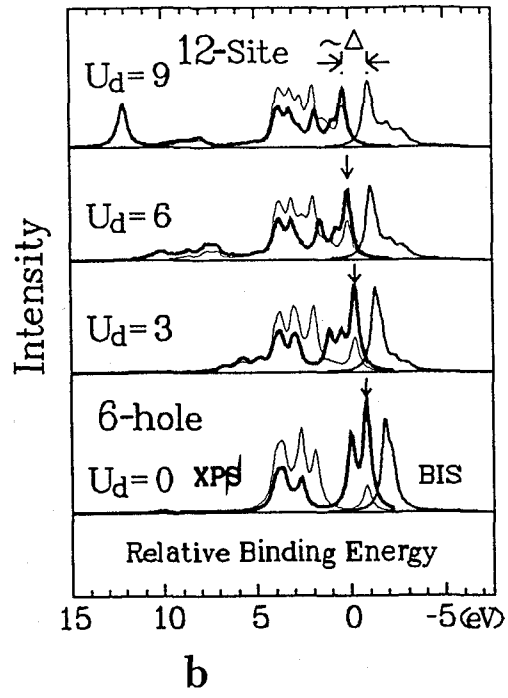

b

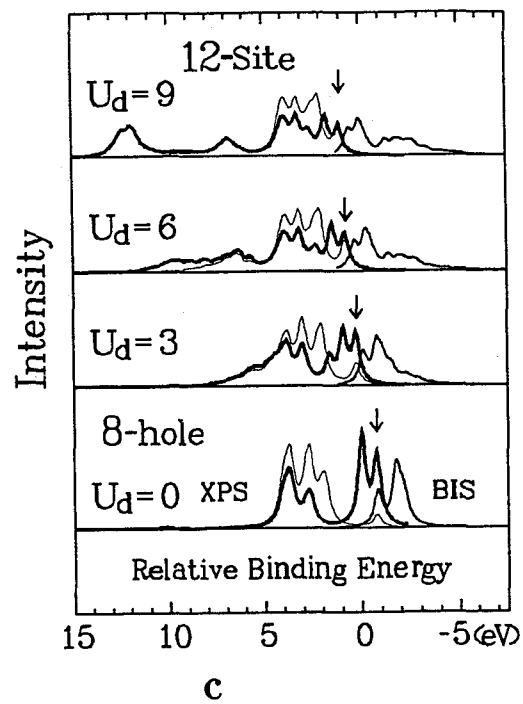

c

Fig. 4.10. Valence Band XPS and BIS spectra of 11- and 12 site systems for various U_d's when there is a hole per Cu atom (**a**, **b**) and when there are two additional holes.(**c**) The relation $U_p = U_d/2$ are always assumed. If additional holes are present, the charge excitation gap does not present any more.

neighborhood of the Fermi surface; the one-body energy levels are still present even when there is the strong Coulomb interaction. Outside the region, the correlation effect appears chiefly as the growth of a peak with the Coulomb interaction, where the peak corresponds

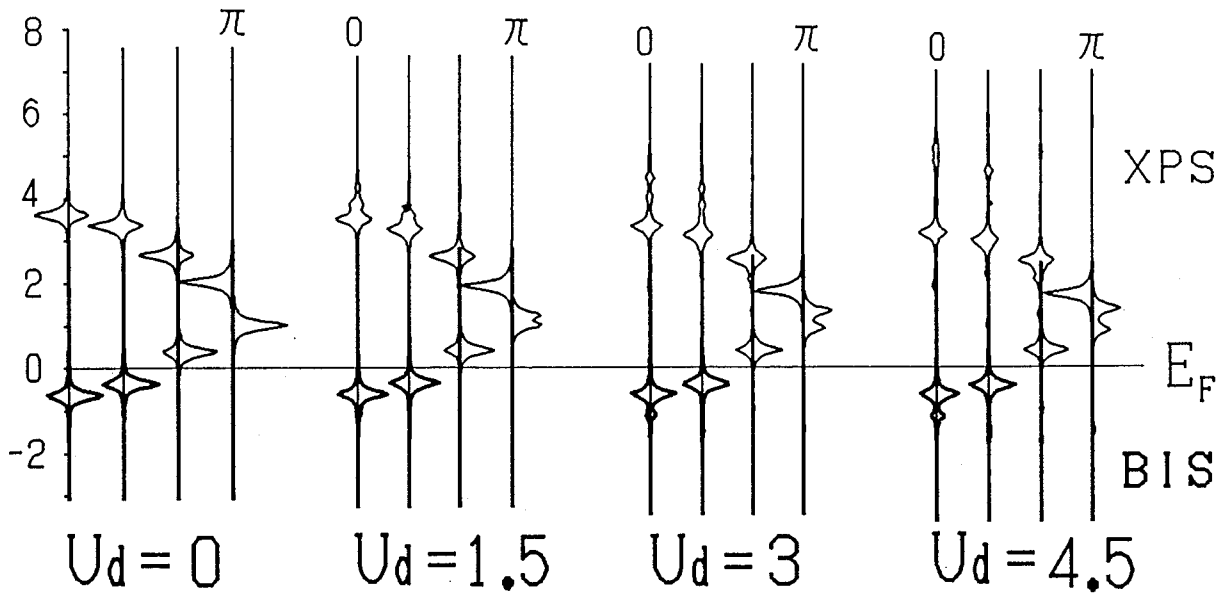

Fig. 4.11. Angle resolved XPS and BIS spectra of the 12-site system with 6 holes. We here take the Fermi-energy as a reference of the relative binding energy. The relative binding energy is shown on the vertical axis. The spectra above/below the horizontal line denote the XPS/BIS spectra, where the right/left-hand side of each vertical line corresponds to the d/p hole removal or additional cases.

to a local two-hole bound state. If there are additional holes, the charge excitation gap is not present any more.(Fig. 4.10c)

If we analyze the spectra more carefully, we will find the correlation effect within the range $5\text{eV} > E_b > -2\text{eV}$. Figure 4.11 shows the angle resolved XPS and BIS spectra[7] of the 12-site system with 6 holes when $U_d = 2U_p = 0.0, 1.5, 3.0$ and 4.5. The d-hole removal spectra for $k = \pi$ splits with increasing the Coulomb repulsion. The origin of the splitting is not clear, since it cannot be explained by the anti-ferromagnetic correlation between d orbitals. Such a splitting is not observed for p-hole removal case.

We finally compare the XPS spectra of each cluster with its energy levels obtained by the HF approximation assuming either the antiferromagnetic or nonmagnetic state. Figure 4.12 shows the 12-site case, where the energy levels obtained by the antiferromagnetic and nonmagnetic HF approximations are shown by short bars. Most of the peaks within the ranges $4\text{eV} > E_b > 1.5\text{eV}$ and $1.5\text{eV} > E_b > 0\text{eV}$ are identified by the HF energy levels of oxygen and Cu band, apart from the splitting of the d-hole removal spectra discussed above. The peaks, whose binding energies are more than 6eV, may correspond to

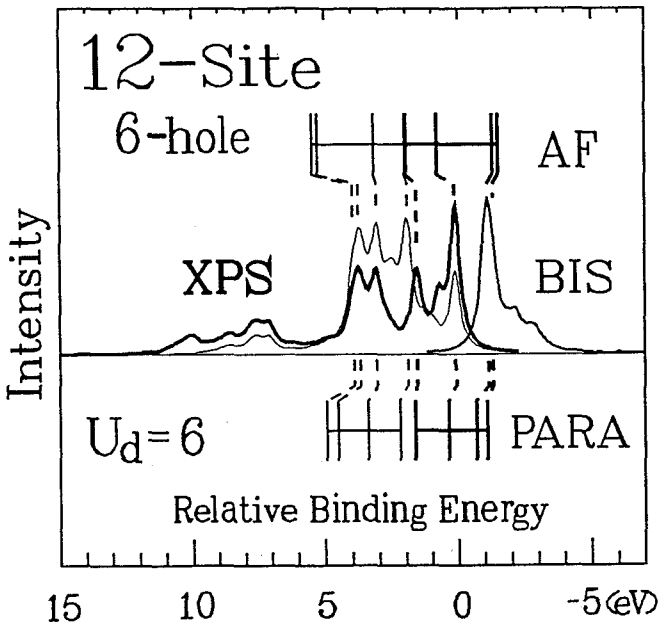

Fig. 4.12. Valence band XPS and BIS spectra of the 12-site system when there are 6 holes. Energy levels obtained by para-magnetic and anti-ferromagnetic Hartree Fock equations are shown by short bars. The thick and fine bars denote the levels of oxygen and Cu band, respectively.

local 2-hole bound states formed by the Coulomb energy U_p or U_d.[15] In this case, the valence band width obtained from the calculated XPS spectra is 17% and 15% reduced compared with that of the antiferro- and nonmagnetic HF solution, respectively.

The reduction of the band width is common to all system, but it depends on the system size, where the minimum is 13% of the 15-site system and the maximum is 21% of the 7-site system.(Table IV.I) A systematic dependence of the reduction ratio on the boundary condition and the linear dimension of the clusters is not obtained. The shape of the XPS spectra is also size dependent. For example the XPS spectra of 12-site system have a large peak at the Fermi level but those of the 15-site system do not. We conclude that the size dependence of the valence band XPS spectra is rather large, which indicates the need of the analysis of larger systems to obtain quantitative estimates of the reduction of the band width due to the correlation.

—Table IV.I. —

Reduction of occupied valence band width obtained from the calculated XPS spectra compared with anti-ferromagnetic (paramagnetic*) HF solution.

System size	Valence band width (eV) a. Hartree Fock	b. Present calculation	Reduction ratio b/a (%)
7	4.8	3.8	79%
8	4.9 (4.9*)	4.1	83% (83%*)
11	4.8	4.1	86%
12	4.7 (4.5*)	3.9	83% (85%*)
15	4.9	4.2	87%

§4.6 Conclusion

We have studied the Cu $2p$ XPS, XAS valence band XPS and BIS spectra of the Cu_nO_m clusters, taking into account the intra-atomic Coulomb interactions. In conclusion we have obtained the following properties of these spectra.

a) The main peak of the Cu $2p$ XAS and XPS spectra have a multiple peak structure on the high energy side. The structure arises from the fact that there are various valence hole distributions of the final states.

b) There appears a $|\underline{c}d^{10}\underline{L}^2\rangle$ peak between main and satellite peaks of the Cu $2p$ XPS spectra, which arises from the $|d^{10}\underline{L}^2\rangle$ component of the initial state produced by the hole itinerancy.

c) The main peak of the Cu $2p$ XPS spectra shifts to high energy side with additional hole density.

These are the properties of the core level spectra of larger clusters ($n \geq 3$), and have not been obtained in the previous calculations using the single Cu atom cluster. Size dependence of both core level and valence band photo-emission spectra are also investigated, and the next two conclusions are drawn.

d) The interval between the main peak $|\underline{c}d^{10}\underline{L}\rangle$ and the satellite one $|\underline{c}d^{9}\rangle$ of the Cu $2p$ XPS spectra of the single Cu atom cluster is smaller than that of the larger clusters. This means that the kinetic energy of a valence hole is reduced by the boundary effect in the case of the single Cu atom cluster.

e) The angle resolved photo-emission spectra for d-hole removal at $k = \pi$ splits when there is strong intra-atomic Coulomb repulsion.

f) The valence band XPS and BIS spectra of the Cu_nO_{n+1} chain or the Cu_nO_n rings depend on the system size within the cluster sizes adopted in the present investigation. The reduction of the valence band width by the correlational effect, for example, ranges from 13% (n=7) to 21% (n=3) which are of the same order as the value 20% concluded by Kuramoto and Schmidt.[7]

References

1) J. Ghijsen, L. H. Tjeng, J. van Elp, H. Eskes, J. Westerink, G. A. Sawatzky and M. T. Czyzyk: Phys. Rev. **B38** (1988) 11322.
2) A. Bianconi, M. De Santis, A. Di Cicco, A. M. Flank, A. Fontaine, P. Lagarde, H. Katayama-Yoshida, A. Kotani and A. Marcelli: Phys. Rev. **B38** (1988) 7196.
3) W. R. Flavell and R. G. egdell: Phys. Rev. **B39** (1989) 231.
4) T. Nishino and J. Kanamori: J. Phys. Soc. Jpn. **59** (1990) 253.
5) C. A. Balseiro, M. Avignon and E. R. Gagliano: Solid State Commun. **72** (1989) 763.
6) E. R. Gagliano and C. A. Balseiro: Phys. Rev. Lett. **28** (1989) 2999.
7) Y. Kuramoto and H. J. Schmidt:*Strong Correlation and Superconductivity,* eds. H. Fukuyama, S. Maekawa and A. P. Malozemoff (springer, Berlin, 1989) p. 88.
8) K. Okada and A. Kotani: J. Phys. Soc. Jpn. **58** (1989) 1095.
9) A. Fujimori:*High T_c Superconductors,* eds. A. Bianconi and A. Marcelli (Pergamon, 1989) p. 3.
10) V. J. Emery: Phys. Rev. Lett. **58** (1987) 2794.
11) C. Lanczos: J. Res. Nat. Bur. Standards **45** (1950) 255.
12) V. Heine:*Solid State Physics,* eds. H. Ehrenreich, F. Seitz and D. Turnbull (Academic Press, New York, 1980) Vol. 35, p. 87.
13) A. Fujimori: Phys. Rev. **B39** (1988) 793.
14) V. Barnole, J. -M. Mariot, C. F. Hague, C. Michel and B. Raveau: Phys. Rev. **B41** (1990) 4262.
15) J. Kanamori: Prog. Theor. Phys. **30** (1963) 275.

Chapter V

Charge Excitation Gap of the One-Dimensional d-p Model as a Function of Inter-Atomic Coulomb Repulsion

§5.1 Introduction

When the d-p model was proposed by Emery as a conduction model of the CuO_2 plane,[1] the model did not contain any inter-atomic Coulomb repulsion U_{pd} between Cu-3d and oxygen-$2p$ orbitals. Soon after that, they modified the model so that it had finite U_{pd} based on both experimental results[2] and band theories.[3,4] Since U_{pd} works between neighboring sites, it is different from intra-atomic Coulomb interactions U_p and U_d in the following points:

(i) The intra-atomic Coulomb repulsion is present only between up- and down-spin electrons as far as we do not consider the degeneracy of d or p orbitals, while the inter-atomic one is present among any kind of electrons, regardless of their spin. Thus, even the electronic structure of complete ferromagnetic band is not trivial any more if there is finite inter-atomic Coulomb repulsion.

(ii) The intra-atomic Coulomb repulsion enhances the local moment (the Cu spin) while the inter-atomic one does not enhance it. The latter enhances the charge correlation between neighboring sites.

(iii) The inter-atomic Coulomb repulsion becomes dominant as the coordination number of neighboring sites increases.

A naive consideration leads us to a result that the U_{pd} works only if there are additional holes in oxygen-p orbitals, and that it enhances the charge excitation gap, which is either the charge transfer gap or the Mott-Hubbard gap. Thus we examine in this chapter how

the inter-atomic Coulomb repulsion enhances the charge excitation gap. We should adopt a relatively large cluster in numerical calculation when there is finite U_{pd}, because the interaction itself is finite ranged and it directly causes inter-site correlation. We therefore confine ourselves here to the one-dimensional d-p model in order to gain the linear dimension of the system. The Hamiltonian of the system is

$$\begin{aligned} H_{d-p} = & -t_{pd}\sum_{i\sigma}\left(p^{\dagger}_{(i-1)\sigma}d_{i\sigma}+d^{\dagger}_{i\sigma}p_{(i-1)\sigma}+d^{\dagger}_{i\sigma}p_{i\sigma}+p^{\dagger}_{i\sigma}d_{i\sigma}\right)+\Delta\sum_{i\sigma}p^{\dagger}_{i\sigma}p_{i\sigma} \\ & +U_p\sum_i p^{\dagger}_{i\uparrow}p_{i\uparrow}p^{\dagger}_{i\downarrow}p_{i\downarrow}+U_d\sum_i d^{\dagger}_{i\uparrow}d_{i\uparrow}d^{\dagger}_{i\downarrow}d_{i\downarrow} \\ & +U_{pd}\sum_{i\sigma\sigma'}\left(p^{\dagger}_{(i-1)\sigma}p_{(i-1)\sigma}d^{\dagger}_{i\sigma'}d_{i\sigma'}+d^{\dagger}_{i\sigma}d_{i\sigma}p^{\dagger}_{i\sigma'}p_{i\sigma'}\right), \end{aligned} \tag{5.1}$$

where $p_i^{(\dagger)}$ and $d_i^{(\dagger)}$ denote annihilation (creation) operators of p and d holes, respectively. We set t_{pd} as unity for convenience, for most of the cases in the following studies.† In the preceding chapters we put $U_{pd}=0$, partly because it is hard to handle more than three parameters in the Hamiltonian — Δ, U_p, U_d and U_{pd} — simultaneously and to trace a role of each parameter. Thereby the numerical calculation here is performed only for several typical parameter sets with finite U_{pd}.

Before we work out the numerical calculation, we examine two special parameter cases. First we consider the atomic limit ($t_{pd}=0$) in the next section. It is shown there that we should not adopt an open boundary system if there is finite inter-atomic Coulomb repulsion. In §5.3 we discuss the charge excitation gap at $U_p=U_d=\infty$, where we can map the one-dimensional d-p model into the $S=1/2$ XXZ-spin chain under staggered magnetic field; the charge excitation gap of the original d-p model corresponds to the excitation gap in the spin wave of the chain. If $\Delta=0$, then the system is gapless unless U_{pd} exceeds $2|t_{pd}|$. Numerical result for Cu_4O_4 cluster is shown in §5.4. It is concluded that the intra-atomic Coulomb repulsion enhances the Charge excitation gap, while it cannot be the origin of the gap by itself.(§5.5)

† Sign of t_{pd} is arbitrary, as far as the one-dimensional d-p model is concerned.

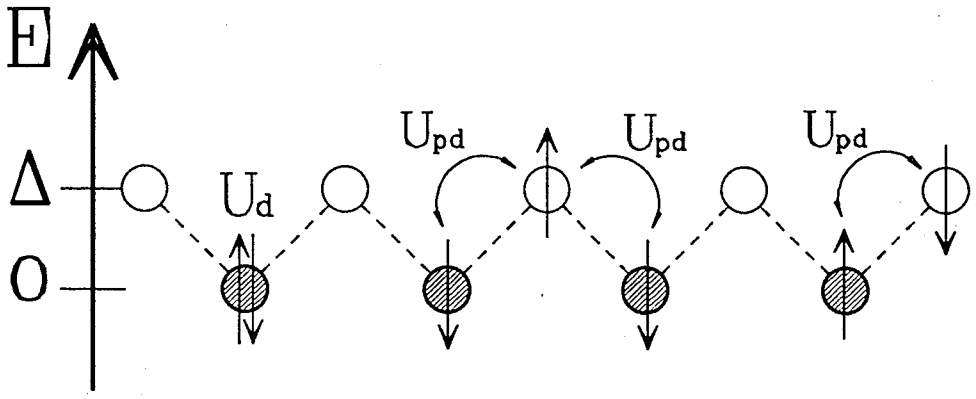

Fig. 5.1. The charge excitation gap of the d-p chain when $t_{pd} = 0$. Open and shaded circles represent p and d orbitals, respectively. The vertical axis shows the one hole energy level. The charge transfer gap is $\Delta + 2U_{pd}$ except at the boundary site, and is $\Delta + U_{pd}$ at the boundary.

§5.2 Atomic Limit

When t_{pd} is zero, the d-p Hamiltonian is diagonal in the configuration space, and we easily obtain the charge excitation gap E_{gap}. If $U_d > \Delta + 2U_{pd}$, the elementary excitation is the one hole transfer from a d orbital to the neighboring p orbital, and the E_{gap} is the same as $\Delta + 2U_{pd}$. (Fig. 5.1) Boundary effect is present because of the inter-atomic Coulomb repulsion; at the boundary site, E_{gap} is $\Delta + U_{pd}$. The consideration here suggests us to use a finite size cluster with periodic boundary condition in the following numerical calculation. Otherwise we under-estimate the charge transfer gap because of the boundary effect.

The atomic limit is not realistic in a sence, because the charge transfer gap $\Delta + 2U_{pd}$ is finite for infinitesimal $\Delta > 0$ when there is finite U_{pd}; if we leave the limit by substituting a finite value into t_{pd}, the gap would be greatly reduced by the itinerancy of holes. For example, the second order process in t_{pd} shown in Fig. 5.2 decreases E_{gap} by amount of $-(t_{pd})^2/\Delta$. The term dominates the E_{gap} if Δ is sufficiently small. We would not refer the second order perturbation any further, since we would get a non-trivial effective Hamiltonian after a systematic but lengthy calculation.

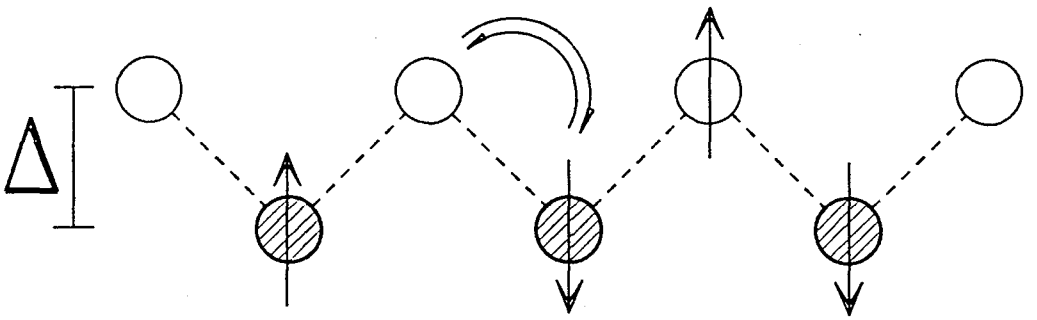

Fig. 5.2. A process of second order perturbation in t_{pd} when there is an additional hole: a d-hole which is by an additional p hole moves empty p orbital, and it comes back again. The E_{gap} decreases by amount of $-(t_{pd})^2/\Delta$ through the process.

§5.3 Large U Limit

We next consider another limit where $U_p = U_d = \infty$. The condition is not totally unphysical, since U_d and $\Delta + U_p$ is relatively larger than t_{pd} and Δ. The system is charge transfer insulator when the band is quarter filled, i.e., when there is a hole per d orbital. We discuss the limit because the electronic structure is less complicated there; only three states $|0\rangle$, $|\uparrow\rangle$ and $|\downarrow\rangle$ are allowed for each site instead of four. Electrons will never exchange their order, for double occupancy is prohibited, thereby we can map the one-dimensional d-p model into $S = 1/2$ XXZ spin chain. The mapping is done through the assignment

$$S_i^z = n_i^{\uparrow} + n_i^{\downarrow} - \frac{1}{2}, \tag{5.2}$$

where we lose the information on the electron spin through the assignment. The d-p Hamiltonian is then transformed to the XXZ-spin Hamiltonian under both uniform and staggered magnetic field:

$$H_{XXZ} = \pm t_{pd} \sum_i (S_i^+ S_{i+1}^- + S_{i+1}^+ S_i^-) + U_{pd} \sum_i S_i^z S_{i+1}^z$$
$$+ \frac{\Delta}{2} \sum_i (-1)^i S_i^z + h \sum_i S_i^z \,. \tag{5.3}$$

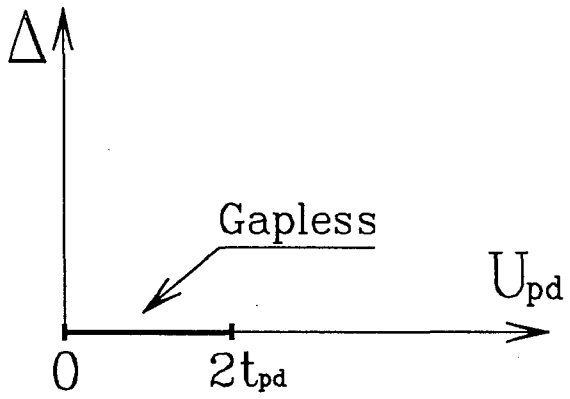

Fig. 5.3. Gapless region of the spin Hamiltonian H_{XXZ} given by eq. 5.3. The spin model is solvable on both vertical and horizontal axes, and the spin wave excitation is gapless if $h = \Delta = 0$ and $0 \leq U_{pd} \leq 2t_{pd}$.

The uniform magnetic field h in the right hand side is connected with the chemical potential of the d-p Hamiltonian. If $h = 0$, total magnetization of the spin chain is zero, the situation which corresponds to the quarter-filled d-p model. The E_{gap} of the d-p model corresponds to the lowest spin wave excitation energy of the spin chain.

The spin model has been solved under $h = 0$ if (i) $U_{pd} = 0$ or (ii)$\Delta = 0$. When $U_{pd} = 0$ the spin Hamiltonian H_{XXZ} can be mapped into a spin-less free Fermion system, and we get $E_{gap} = \Delta$. The case $\Delta = 0$ and $U_{pd} > 0$ is rather complicated. According to Yang and Yang,[5] the spin chain does not have any anti-ferromagnetic order and gapless unless U_{pd} exceeds $2t_{pd}$.(Fig. 5.3) The result means that the inter-atomic Coulomb repulsion enhances the charge transfer gap, while it cannot be the origin of the gap alone if U_{pd} is smaller than $2t_{pd}$.

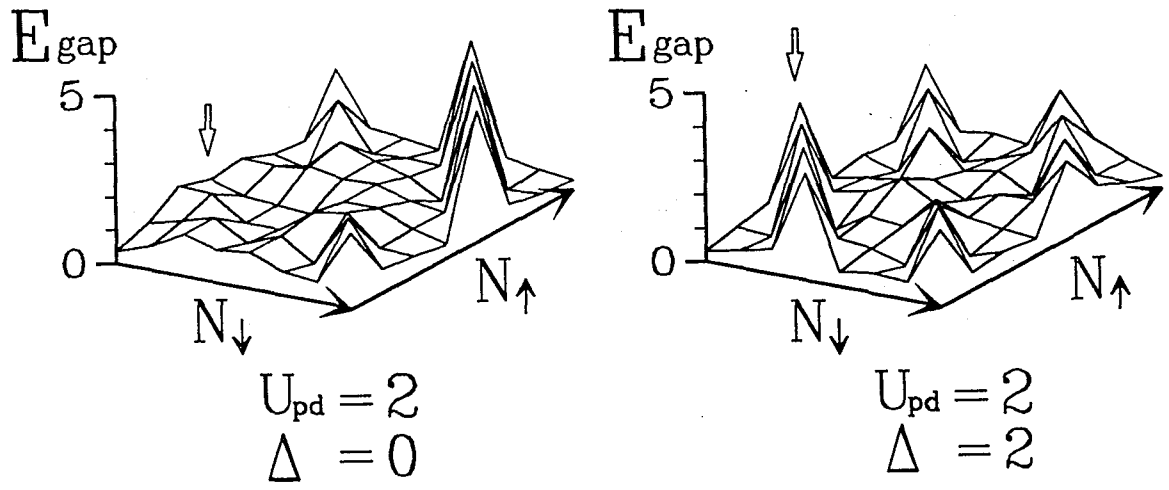

Fig. 5.4. Charge excitation gap of Cu_4O_4 ring obtained by eq. 5.4 when $t_{pd} = 1, U_d = 2U_p = 6, U_{pd} = 2$ and $\Delta = 0$ or 2. If the charge transfer energy Δ is zero, there is no remarkable peak at quarter-filling, (see where the white down arrow points) while a sharp peak is present when there is finite Δ. The charge transfer gap is enhanced by U_{pd} in the latter case.

§5.4 Charge Excitation Gap of Cu_4O_4 Ring

Now we calculate the E_{gap} numerically outside the previous two parameter sets. We adopt one-dimensional Cu_4O_4 ring. We use a definition of E_{gap} for finite size systems of the form†

$$\begin{aligned} E_{gap}[N_\uparrow + 1/2, N_\downarrow + 1/2] = &- E_0[N_\uparrow + 1, N_\downarrow] + E_0[N_\uparrow + 1, N_\downarrow + 1] \\ &+ E_0[N_\uparrow \quad , N_\downarrow] - E_0[N_\uparrow \quad , N_\downarrow + 1], \end{aligned} \tag{5.4}$$

where the $E_0[N_\uparrow, N_\downarrow]$ is the lowest energy when there are N_σ electrons in the Cu_4O_4 cluster.

Figure 5.4 shows the E_{gap} of the cluster when $t_{pd} = 1, U_d = 2U_p = 6, U_{pd} = 2$ and $\Delta = 0$ and 2. The white arrow indicates the quarter-filling point where $N_\uparrow + N_\downarrow = 4$. If the charge transfer energy Δ is zero, there is no remarkable peak at quarter-filling as shown in the left hand side of the figure, while there is a sharp peak if there is finite Δ.(The right

† Details of background for the definition on E_{gap} is given in the Appendix.

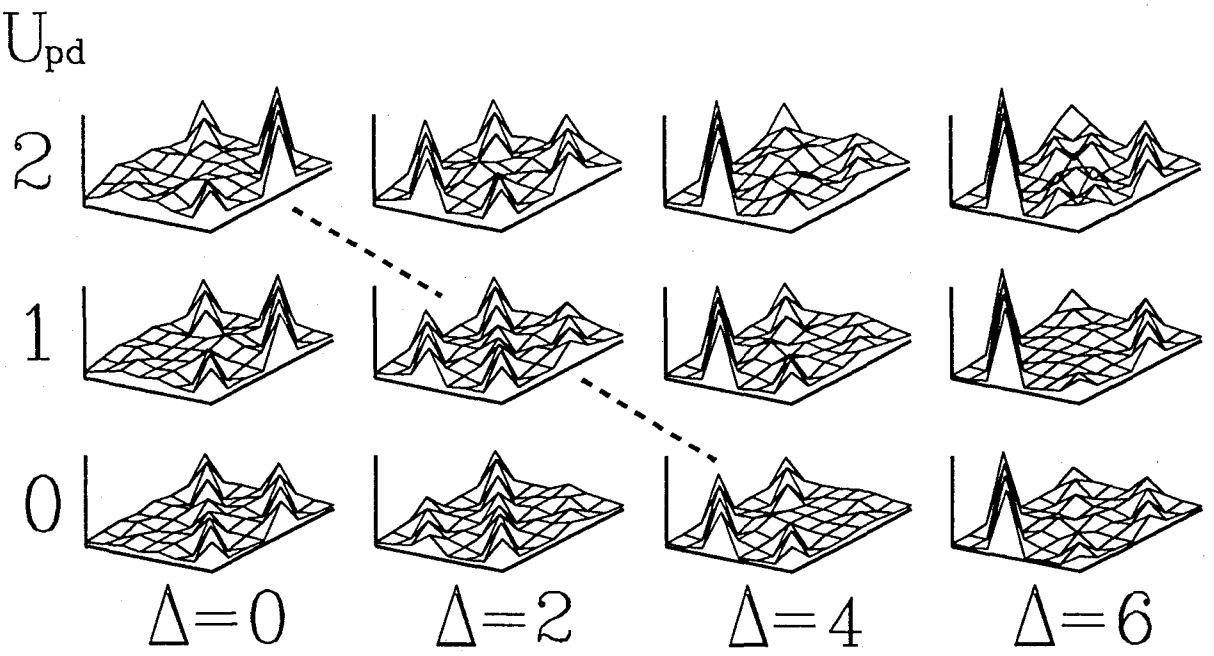

Fig. 5.5. The E_{gap} of Cu_4O_4 cluster for various Δ's and U_{pd}'s when $t_{pd} = 1, U_d = 2$ and $U_p = 6$. The dotted line connects the cases where $\Delta + 2U_{pd} = 4$.

hand side.) The charge transfer gap is enhanced by the inter-atomic Coulomb repulsion U_{pd} in the latter case so that $E_{gap} > \Delta$. There are also sharp peaks at half-filling and 3/4-filling, the peaks which come from on-site Coulomb repulsions. We would not discuss these peaks here, since the hole density that corresponds to these peaks is unrealistic for the Copper oxides.†

Figure 5.5 shows E_{gap} for several Δ's and U_{pd}'s when $t_{pd} = 1, U_d = 2$ and $U_p = 6$. The dotted line in the figure connects the cases where $\Delta + 2U_{pd} = 4$. One can easily see that the charge excitation gap at quarter filling increases with Δ under constant $\Delta + 2U_{pd}$. After the surveillance of E_{gap} on the parameter space,(Δ-U_{pd} plane) we get the result in Fig. 5.6 which shows the gap at quarter filling. As we have studied for the infinite on-site Coulomb repulsion limit, no apprecable E_{gap} is obtained when $\Delta = 0$.

† Half-filled case will be discussed in the next chapter, only for the case where $\Delta = 0$.

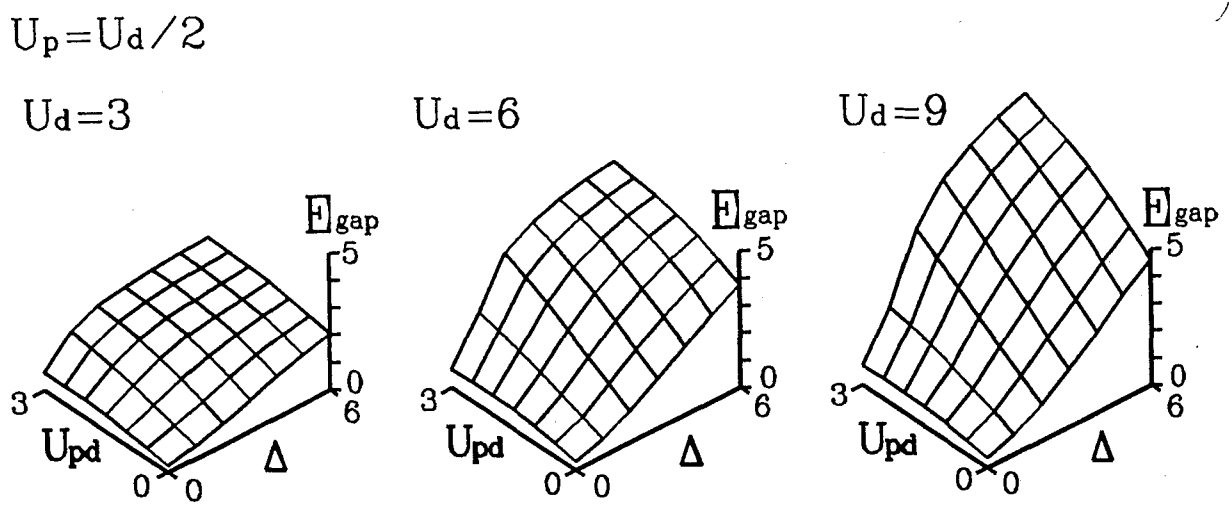

Fig. 5.6. The charge excitation gap of Cu_4O_4 cluster at quarter-filling obtained by eq. 5.4, when $U_d = 3, 6, 9$ and $t_{pd} = 1$. The E_{gap} is much less than $\Delta + 2U_{pd}$, which is the gap for the atomic limit, if Δ is not large enough.

§5.5 Conclusion

In conclusion we have calculated the charge excitation gap of one-dimensional d-p model with inter-site Coulomb repulsion U_{pd}. In conclusion the U_{pd} cannot be the origin of the charge transfer gap by itself, since $E_{gap} \sim 0$ if $\Delta = 0$ for these cases: (i) when $U_p = U_d = \infty$ and $\Delta = 0$, the E_{gap} is zero unless U_{pd} exceeds $2t_{pd}$. (ii) If U_p and U_d are comparable with t, the E_{gap} is very small even when $U_{pd} > 2t_{pd}$.

We have confirmed ourselves to the study on the one-dimensional d-p model. Dimensionality of a system is usually relevant to most of the low-dimensional systems and therefore we should examine two dimensional systems in order to analyze the CuO_2 plane, in future studies.

References

1. V. J. Emery: Phys. Rev. Lett. **58** (1987) 2794.
2. H. Eskes and G. A. Sawatzky: to be published in Phys. Rev. **B**.
3. A. K. McMahan, R. M. Martin, and S. Satpathy: Phys. Rev. **B38** (1988) 6550.
4. M. S. Hyberstein, M. Schlüter, and N. E. Christensen: Phys. Rev. **B39** (1989) 9028.
5. C. N. Yang and C. P. Yang: Phys. Rev. **150** (1966) 321; **150** (1966) 327; **151** 258.

Chapter VI

Charge Excitation Gap of the Extended Hubbard Model

§6.1 Introduction

The Hubbard model[1-3] is a simple model which describes several non-trivial effects of intra-atomic Coulomb interaction in narrow band. When the narrow band is half-filled, there is a finite excitation gap which is known as the 'Mott-Hubbard gap'.[2,3] In real materials, there are also inter-atomic Coulomb interactions between neighboring atoms. Beni and Pincus modified the Hubbard model so that it contained the inter-atomic Coulomb interaction, and discussed the possibility of the charge density wave (CDW) at half-filling.[4] Today their model is called 'the extended Hubbard model', where the Hamiltonian has the form

$$H = -t \sum_{<i,j>\sigma} (c^{\dagger}_{i\sigma} c_{j\sigma} + c^{\dagger}_{j\sigma} c_{i\sigma}) + U \sum_{i} n_{i\uparrow} n_{i\downarrow} + V \sum_{<i,j>} (n_{i\uparrow} + n_{i\downarrow})(n_{j\uparrow} + n_{j\downarrow}) - \mu \sum_{i} (n_{i\uparrow} + n_{i\downarrow}). \tag{6.1}$$

The first two terms in the right hand side represent the Hubbard Hamiltonian. The third term is the Coulomb repulsion between neighboring sites. The chemical potential $\mu = 2V + U/2$ corresponds to the half-filled band.

The ratio of these parameters t, U and V determines the character of the ground state of the half-filled band: the cases (i) $t >> U, V$, (ii) $U >> t, V$ and (iii) $V >> t, U$ correspond to the free-Fermionic, the Mott-Hubbard and the CDW states, respectively.† If these parameters are at the same order, the ground state phase is not trivial. The

† The 'Tomonaga-Luttinger liquid state' is also a candidate for correlated one-dimensional systems. [S.Tomonaga: Prog. Theor. Phys. 5 (1950) 544.]

phase diagram has been investigated by the Hartree-Fock (HF) approximation,[5] the functional integral formalism[6] and the quantum Monte Carlo simulation.[7] Recently van Dongen has analyzed the thermodynamic property of the model by using the perturbation expansion around the Hartree solution.[8] He showed that in high-dimension, $(d > 1)$ the line $U/V = 1/2$ is the phase boundary between the Mott-Hubbard and the CDW phases for both strong correlation limit $(U, V >> t)$ and the weak limit.$(U, V << t)$ Quite recently the ground state phase diagram has been carefully determined numerically for one-dimensional extended Hubbard model by Cannon et al.[9] They confirm the presence of the tricritical point. So far, the charge excitation gap of the one-dimensional extended Hubbard model has not been examined quantitatively.

The purpose of this chapter is to survey the charge excitation gap of the one-dimensional extend Hubbard model on $U - V$ plane, and to observe how the gap reflects the itinerancy of electrons. In the next section, we examine a reduction of the charge excitation gap by the electron itinerancy in the large V region ($U < 2V$) by use of the second order stationary perturbation in t. The perturbation study is, however, inapplicable near the phase boundary. Thus, in §6.3 we calculate the gap numerically and estimate the gap for the infinite size system through the extrapolation with respect to the system size. We compare the numerical result with that of the perturbation study and the Hartee-Fock approximation. In §6.4, conclusions are summarized.

§6.2. Perturbation Study in the Large V region

We calculate the charge excitation gap of the one-dimensional extended Hubbard model at half-filling via the stationary perturbation theory[10] in the large V region. ($U < 2V$) The result obtained here will be compared with the numerical results later.

We regard the kinetic energy term in the extended Hubbard Hamiltonian as a perturbation:

$$H = H_I + H_0 \tag{6.2}$$

$$H_I = -t \sum_{i\sigma} (c^\dagger_{i\sigma} c_{i+1\sigma} + c^\dagger_{i+1\sigma} c_{i\sigma}) \tag{6.3}$$

$$H_0 = U \sum_i n_{i\uparrow} n_{i\downarrow} + V \sum_i (n_{i\uparrow} + n_{i\downarrow})(n_{i+1\uparrow} + n_{i+1\downarrow}) - (2V + \frac{U}{2}) \sum_i (n_{i\uparrow} + n_{i\downarrow}). \tag{6.4}$$

The charge excitation gap E_{gap} is usually defined as

$$E_{gap} = \lim_{N\to\infty} E^N_{gap}$$
$$E^N_{gap} = E^N(N+1) - 2E^N(N) + E^N(N-1), \tag{6.5}$$

where $E^N(M)$ is the ground state energy of N-site system when there are M electrons in the lattice. In fact, there is a less complicated formula of E^N_{gap} at half-filling for even N ,

$$E^N_{gap} = 2\{E^N(N+1) - E^N(N)\}, \tag{6.6}$$

since we choose the chemical potential $\mu = 2V + U/2$ so that the Hamiltonian is invariant under the particle-hole transformation.

We first consider the half-filled band — the N electron case. There are two non-perturbed states $|0\rangle$ and $|0'\rangle$, where doubly occupied sites and empty sites appear alternatingly, as shown in Fig. 6.1a. They have the same eigenvalues for H_0, i.e. $E^N_0(N) \equiv \langle 0|H_0|0\rangle = -2NV$. It is sufficient to treat one of them in the perturbation study, because they do not have any overlap

$$\langle 0|H^n_I|0'\rangle = 0\,, \quad \text{if } n < 2N\,. \tag{6.7}$$

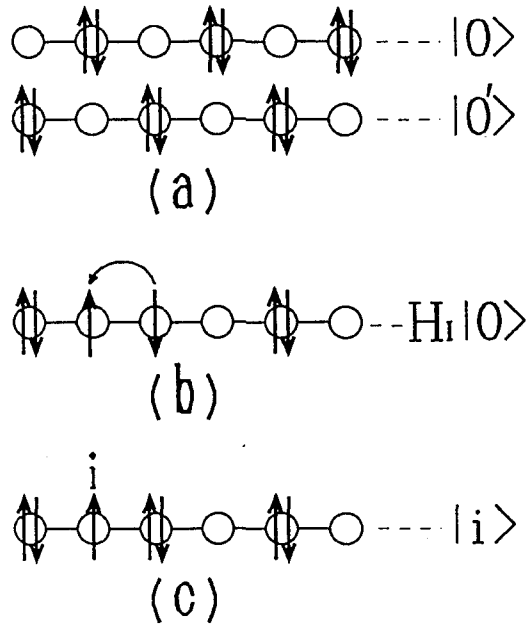

Fig. 6.1. Electron configurations that appear as the initial and intermediate states in the second order perturbation for $U > 2V$: (**a**) Two equivalent non-perturbed states $|0\rangle$ and $|0'\rangle$ at half-filling. (**b**) An intermediate state in $H_I|0\rangle$. There are $2N$ intermediate states. (**c**) A non-perturbed state $|i\rangle = c^\dagger_{i\sigma}|0\rangle$ where one additional electron is created at the half-filled band.

There are $2N$ intermediate states which we have to take into account for the second order perturbation.(Fig. 6.1**b**) The eigenvalue of H_0 for these intermediate states is $E_0^N(N) + 3V - U$, thus the energy correction for the second order is

$$\varepsilon^N(N) \equiv \langle 0|H_I \frac{1}{E_0^N(N) - H_0} H_I|0\rangle = -2N\frac{t^2}{3V-U}. \tag{6.8}$$

We next consider the $N+1$ electron case. A non-perturbed state $|i\rangle$ is given by putting an electron on the empty site i of the state $|0\rangle$.(Fig. 6.1**c**) The eigenvalue $E_0^N(N+1) \equiv \langle i|H_0|i\rangle$ is $E_0^N(N) + 2V - U/2$. The state $|i\rangle$ is hybridized with $|i \pm 2\rangle$. Therefore we obtain two different kins of energy corrections as a result of the second order perturbation: one is the diagonal term

$$\begin{aligned}\varepsilon^N_{diag}(N+1) &\equiv \langle i|H_I \frac{1}{E_0^N(N+1) - H_0} H_I|i\rangle \\ &= \varepsilon^N(N) + \frac{8t^2}{3V-U} - \frac{4t^2}{2V-U} - \frac{2t^2}{V}\end{aligned} \tag{6.9}$$

and the other is the off-diagonal term

$$\begin{aligned}\varepsilon^N_{off}(N+1) &= \langle i|H_I \frac{1}{E_0^N(N+1) - H_0} H_I|i \pm 2\rangle \\ &= -\frac{t^2}{2V-U}.\end{aligned} \tag{6.10}$$

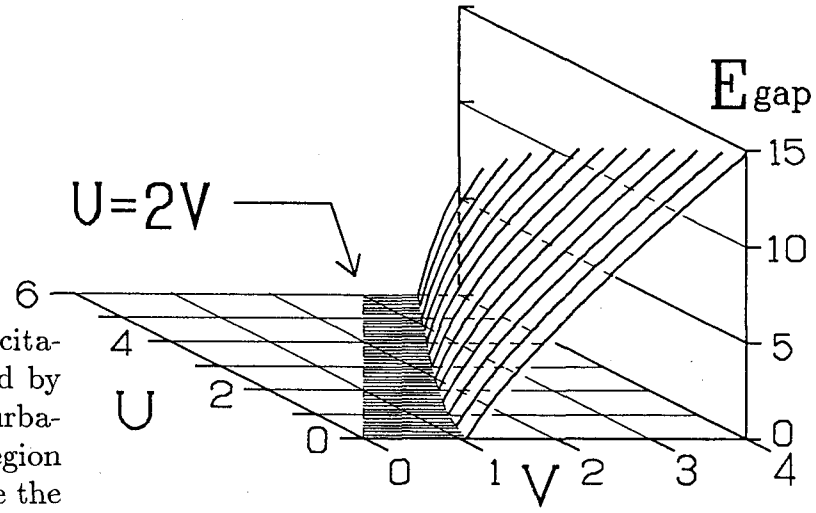

Fig. 6.2. The charge excitation gap E_{gap} obtained by the second order perturbation. In the shaded region E_{gap} is negative, where the perturbation study does not work any more.

The latter is merely the hopping amplitude of the additional electron; the 'band width' of this additional electron is $4|\varepsilon^N_{off}(N+1)|$. Thereby the second order energy correction $\varepsilon^N(N+1)$ is between $\varepsilon^N_{diag}(N+1)+2\varepsilon^N_{off}(N+1)$ and $\varepsilon^N_{diag}(N+1)-2\varepsilon^N_{off}(N+1)$.

Now we can obtain the charge excitation gap. The E_{gap} is $2\{E^N_0(N+1)-E^N_0(N)\} = 4V-U$ when $t=0$, the value which is finite $(=2V)$ at the phase boundary $U=2V$. The second order process in t reduces the gap by amount of $\varepsilon^N_{diag}(N+1)+2\varepsilon^N_{off}(N+1)-\varepsilon^N(N)$ and the gap for the finite t is

$$E_{gap} = 4V - U + \frac{16t^2}{3V-U} - \frac{12t^2}{2V-U} - \frac{4t^2}{V}. \tag{6.11}$$

Figure 6.2 shows the gap E_{gap} in eq. 6.11. In the shaded region the value is negative, where the second order perturbation does not work any more; the perturbation study suggests that no CDW order is present in the region.

Let us briefly see how the perturbation study works in the large U side.$(U > 2V)$ At half-filling, there are 2^N non-perturbed states that have any double occupancy. According to the degeneracy of these non-perturbed states, the second order perturbation at half-filling leads the antiferromagnetic Heisenberg Hamiltonian with coupling constant $J =$

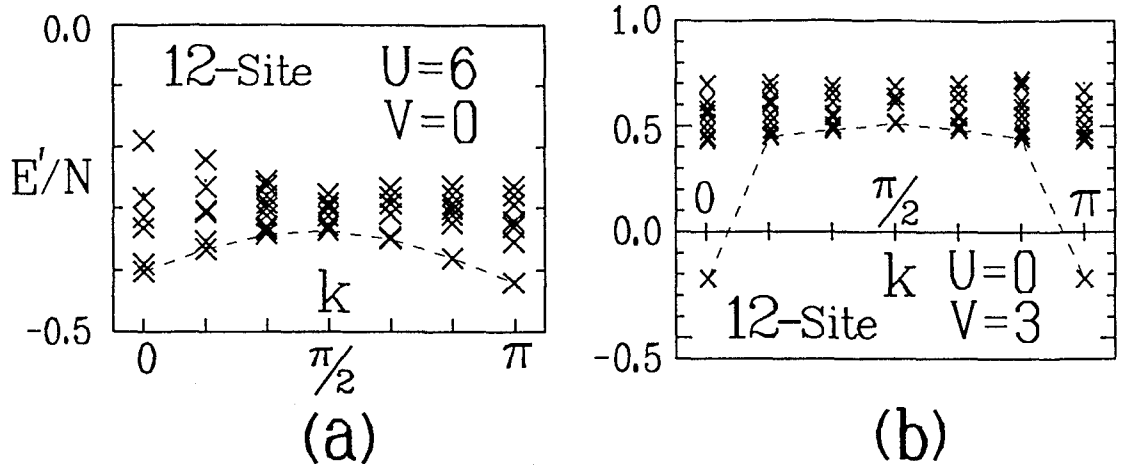

Fig. 6.3. Low-lying eigenstates of 12-site extended Hubbard ring at half-filling for each k. The vertical axis shows the energy per site $E'/N = \langle H + \mu \sum_i (n_i^{\uparrow} + n_i^{\downarrow}) \rangle / N$. (**a**) When U is much larger than V, $(U = 6, V = 0)$ the system has the Mott-Hubbard character. The dotted line connects the lowest energy in each subspace, where the line reflects the dispersion of the spin wave. (**b**) When V is much larger than U, $(U = 0, V = 3)$ the CDW order is present. There are two low energy states in the subspaces with $k = 0$ and $k = \pi$, and there is finite excitation gap above these two.

$t^2/(U - V)$.[11] In the same manner as we have obtained the Heisenberg model, we get the t-J model for non half-filled band.[12] The one-dimensional t-J model have not been solved except for a special parameter set[13] and the parameter set does not coincide with our model; we cannot obtain the charge excitation gap of the extended Hubbard model without performing the numerical calculation on the t-J model. We would better perform the numerical calculation on the original Hamiltonian (eqs. 6.2∼6.4) rather than on the effective Hamiltonian obtained by the perturbation study.

§6.3. Numerical Result

We calculate the ground state energies of 4,6,8,10,12 and 14-site extended Hubbard rings by diagonalizing the Hamiltonian (eqs. 6.2∼6.4) via the numerical method which we have studied in Chap. II; we use the rotational symmetry of the system and obtain the ground state for each lattice momentum k. It takes about a hundred-second of the CPU time to get the ground state energy of 14-site system for every parameter set, and

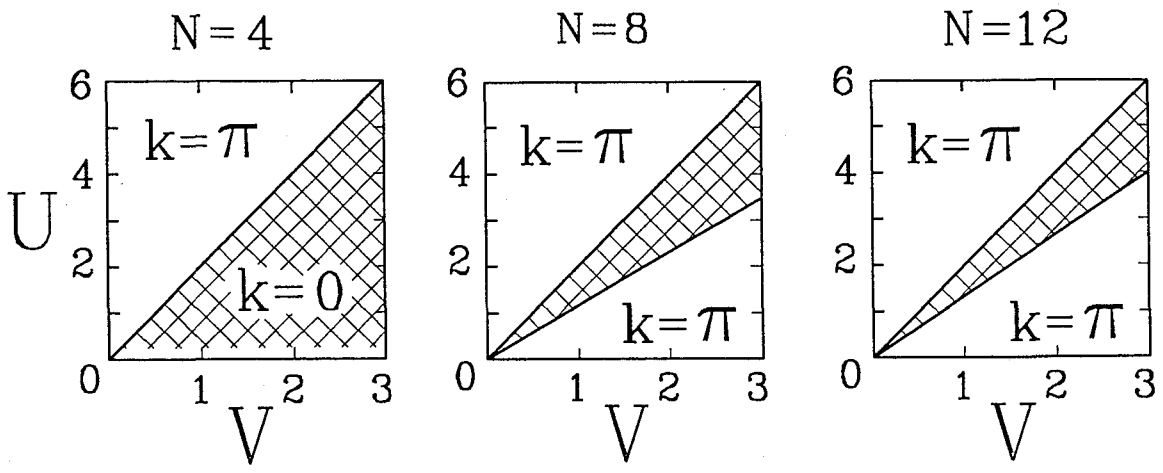

Fig. 6.4. Momentum of the ground state of 4,8 and 12-site rings. Inside the meshed region the momentum is zero. The region gets narrow with the system size N.

it is hard to survey the whole parameter range for both U and V. Therefore most of the numerical calculations are worked out up to $N = 12$.

A trial numerical calculation shows that the ground state has a definite lattice momentum. Figures 6.3 (a) and (b) show the energy distribution of 12-site system at half-filling for each momentum k. The vertical axis shows the energy per site $E'/N = \langle H + \mu \sum_i (n_i^{\uparrow} + n_i^{\downarrow}) \rangle / N$. In the large U region,$(U = 6, V = 0)$ there are many eigenstates just above the ground state.(Fig. 6.3 a) The dotted line connects the lowest energy in each sub space, where the line reflects the dispersion of the spin wave excitation. On the other hand, in the large V region $(U = 0, V = 3)$ there are two low energy states at $k = 0$ and $k = \pi$, and there is finite excitation gap above these two.(Fig. 6.3 b) For both cases, the ground states have the momentum $k = \pi$. The lattice momentum of the ground state is determined by such a way for every system size and parameter set. At half-filling, the ground state momentum is always zero for 6, 10 and 14-site systems, while it depends on the parameters U and V for 4, 8 and 12-site systems.(Fig. 6.4) When an additional electron is introduced to the half-filled band, the momentum is always the same as the Fermi momentum when $U = V = 0$.

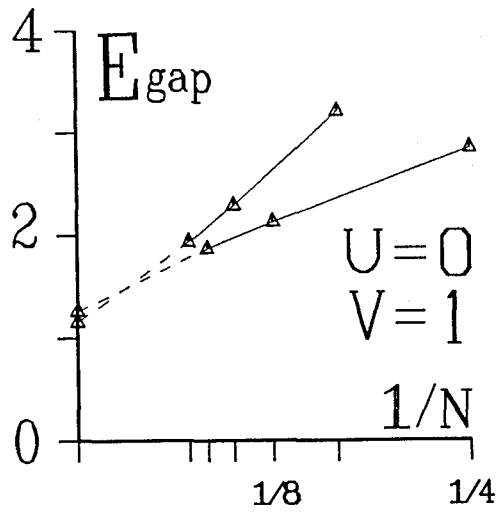

Fig. 6.5. The charge excitation gap $E^{4n}_{gap,\pi}$ and E^{4n+2}_{gap} when $U = 0$ and $V = 1$. We obtain the large N limits $E_{gap} = 0.66$ and 0.58 by connecting $\{E^{6}_{gap}, E^{10}_{gap}, E^{14}_{gap}\}$ and $\{E^{4}_{gap,\pi}, E^{8}_{gap,\pi}, E^{12}_{gap,\pi}\}$ with curves of second degree.

After we have obtained the ground state energy for both half-filled and non-half-filled bands, we calculate the charge excitation gap for each system size and parameter set. We then perform an extrapolation in $1/N$ to reduce the size effect. We evaluate the gap $E_{gap} = \lim_{N\to\infty} E^{N}_{gap}$ from three different groups of data. The first group consists of $E^{N=4n+2}_{gap}$ for $N = 6, 10$ and 12 defined by eq. 6.6. The second and third groups consist of the gap for 4, 8 and 12-site systems defined as

$$E^{N=4n}_{gap,k=0} = 2\{E^{N}(N+1) - E^{N}_{k=0}(N)\}, \tag{6.12}$$

and

$$E^{N=4n}_{gap,k=\pi} = 2\{E^{N}(N+1) - E^{N}_{k=\pi}(N)\}, \tag{6.13}$$

where $E^{N}_{k}(N)$ is the lowest energy at half-filling with the momentum k. (Either $E^{4n}_{gap,0}$ or $E^{4n}_{gap,\pi}$ is the same as E^{4n}_{gap} in eq. 6.6.) Figure 6.5 shows these gaps when $U = 0$ and $V = 1$. The value $E^{4n}_{gap,0}$ does not differ from $E^{4n}_{gap,\pi}$ for more than ± 0.03 for all n, and therefore only $E^{4n}_{gap,\pi}$ and E^{4n+2}_{gap} are plotted. The gap E^{4n+2}_{gap} is greater than $E^{4n}_{gap,0(\pi)}$ for each n, because the former reflects the 'closed shell structure' of the ground state at half-filling.[14] Since we have only three points in each group of data, and have no guiding principle for extrapolation, we connect these three points by a curve of second degree to obtain E_{gap} at large N limit: the data E^{4n+2}_{gap}, $E^{4n}_{gap,0}$ and $E^{4n}_{gap,\pi}$ give $E_{gap} = 0.58$,

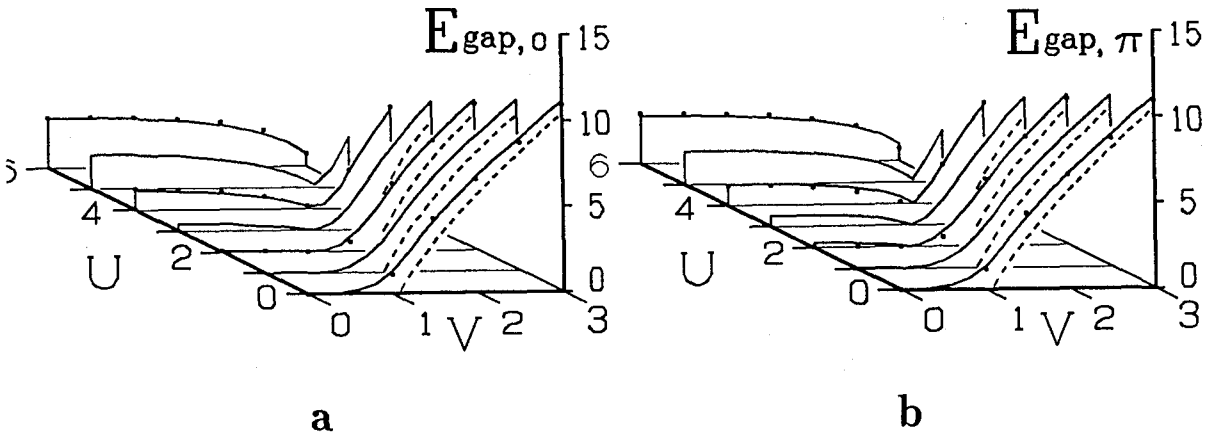

a **b**

Fig. 6.6. The charge excitation gap at large N limit. In both figures the dot denotes the gap E_{gap} obtained from E_{gap}^{4n+2}, and the dotted line denotes the result of the second order perturbation. The real line is the gap (**a**) $E_{gap,0}$ and (**b**) $E_{gap,\pi}$ obtained from $E_{gap,0}^{4n}$ and $E_{gap,\pi}^{4n}$, respectively.

0.65 and 0.66, respectively. We should regard their difference (=0.08) as the error in the extrapolation.

Figures 6.6 (**a**) and (**b**) show the E_{gap} on the U-V plane. The dots in the figures represent the gap obtained from E_{gap}^{4n+2}. The real line shows E_{gap} that comes from $E_{gap,0}^{4n}$ (Fig. 6.6**a**) or $E_{gap,\pi}^{N=4n}$.(Fig. 6.6**b**) After all, the gaps obtained by three different ways do not differ so much. The result of the second order perturbation study is shown by the dotted line for comparison. The perturbation study always under estimates the gap; the numerical data shows the presence of finite gap in the shaded region in Fig. 6.2, except at the phase boundary.

The numerical result is also compared with that of the Hartree-Fock (HF) approximation.[5] (Fig. 6.7) We assume the CDW or the anti-ferromagnetic (AF) order for the approximation; the CDW and AF orders are stabilized within the parameter range $U < 2V$ and $U > 2V$, respectively. In the large V region, the approximation deduces the gap that is a constant of V. Thus the approximation gives finite charge excitation gap at the phase boundary $U = 2V$. The numerical result, however, shows that the gap is greatly reduced near the phase boundary; the HF approximation always overestimates the E_{gap}.

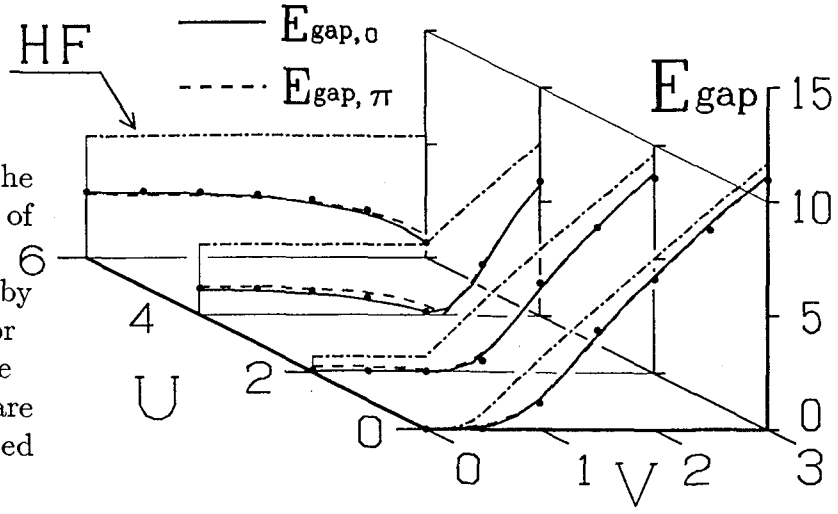

Fig. 6.7. The same as the Figure 6.6. The result of the Hartree Fock approximation is shown by the dash-dotted lines for comparison. Here, the $E_{gap,0}$ and the $E_{gap,\pi}$ are shown by real and dotted line, respectively.

The phase boundary is near the line $U = 2V$, but slightly shifted to the large-V side by the quantum effect. This result agrees with that Cannon et al. have obtained through the analyses of the CDW order parameter. They further confirm the presence of a tricritical point above $U = 3.5$. It is, however, difficult to observe the tricritical point from the E_{gap} alone. There is at least a qualitative change in the shape of the gap at the phase boundary; the gap tangentially touches the U-V plane at the origin ($U = V = 0$) whereas it has a kink at the phase boundary for modest U and V.

Finally, let us see how the CDW order is suppressed near the phase boundary. We adopt the definition of S which does not contain the self correlation term:

$$S = \frac{1}{N-1}\sum_{i=2}^{N}(-1)^i(n_{1\uparrow}+n_{1\downarrow}-1)(n_{i\uparrow}+n_{i\downarrow}-1). \tag{6.14}$$

Figure 6.8 shows the CDW order parameter S in the large V region. The parameter S is greatly reduced near the phase boundary by the itinerancy of the electrons, especially at the neighborhood of the origin.

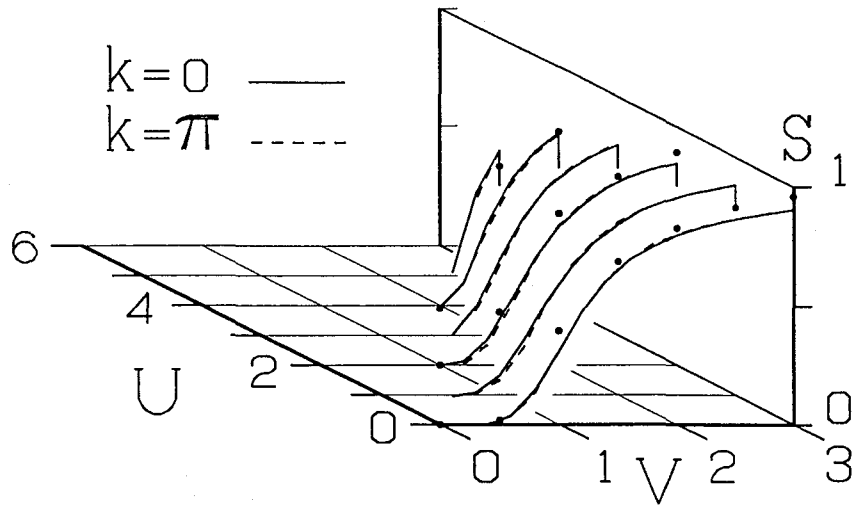

Fig. 6.8. The CDW order parameter S on the $U-V$ plane. The real and dotted lines are the S extrapolated from the data for $N=4,8,12$ with $k=0$ and π, respectively. The dott denotes represent S for $N=6,10,14$ and $k=0$. The extrapolation for S is performed as we have done for E_{gap} in Fig. 6.5

§6.4. Conclusion and discussion

We have evaluated the charge excitation gap of the one-dimensional extended Hubbard model at half-filling by use of the diagonalization method. We use the rotational symmetry of the system to reduce the size of the matrix. The calculation up to 14-site system enables us to perform the finite size scaling, and to get a quantitative result on the charge excitation gap E_{gap}. At the phase boundary, the E_{gap} is almost zero within the parameter range that we had survayed, $0 \leq U \leq 6$ and $0 \leq V \leq 3$.

The numerical result is compared with the results of the second order perturbation study and the Hartree-Fock approximation. The second order perturbation always underestimates the gap E_{gap} and the method is inapplicable near the phase boundary. On the other hand, the HF approximation always over estimates the gap; the gap obtained by the approximation is a constant of V in the large V region. Actually, the calculated gap gradually decreases to zero with increasing V in the large V side.

The one-component lattice Fermion model with nearest neighbor repulsion V does not have CDW order and the finite charge excitation gap as far as the repulsion is smaller

than $2t$, which is the half of the band width.[15] We have studied here the two component lattice Fermion model — the extended Hubbard model — and observed the presence of finite gap for fairly small V compared with t. Does the generalized m-component Fermion system have the gap for infinitesimal V? It would be one of the problem on one-dimensional lattice fermion models to future.

References

1) J. Kanamori: Prog. Theor. Phys. **30** (1963) 275.
2) J. Hubbard: Proc. Roy. Soc **A281**(1964) 401.
3) M. C. Gutzwiller: Phys. Rev. Lett. **10** (1963) 275; Phys. Rev. **134** (1965) A1726.
4) G. Beni and P. Pincus: Phys. Rev. **B9** (1974) 2963.
5) D. Cabib and E. Callen: Phys. Rev. **B12** (1975) 5249.
6) U. Wolff: Nulc. Phys. **B255** (1983) 391.
7) J. E.Hirsch: Phys. Rev. **B31** (1985) 6022.
8) P. G. J. van Dongen: Phys. Rev. Lett. **67** (1991) 757.
9) J. W. Cannon, R. T. Scalettar, and E. Fradkin: Phys. Rev. **B44** (1991) 5995.
10) L. I.Schiff: *Quantum Mechanics* (McGraw-Hill,1963) p. 245.
11) A. E. Ruckenstein, P. J. Hirschfeld, and J.Appel: Phys. Rev. **B36**(1987) 857.
12) G. Baskaran, Z. Zou and P. W. Anderson: Solid State Commun. **63** (1987) 973.
13) P. A. Bares and G. Blatter: Phys. Rev. Lett. **64** (1990) 2567.
14) J. Wagner, W. Hanke and D. J. Scalapino: Phys. Rev. **B43** (1990) 10517.
15) C. N. Yang and C. P. Yang: Phys. Rev. **150** (1966) 321; **150** (1966) 327; **151** (1966) 258.

Chapter VII

Summary

The author has studied electron correlation effects, which originate in short range Coulomb interactions, in one- and two-dimensional periodic systems. Since there is no general analytic method for these systems, most of the analyses were done through numerical calculations on finite size clusters. Ground state properties and excitation spectra of the periodic systems were examined when intra- and inter-atomic Coulomb energies are present, as it is summarized here.

Several numerical methods are integrated in chapter II in order to study the finite systems via the Lanczos and the recursion methods. We developed efficient technique of computations without which we cannot draw meaningful conclusions from the computation. The systematic numerical method enables us to draw maximum ability of computers and also physical information from the study in finite-size systems.

Ground state properties of the Cu_4O_{12} cluster, was studied in chapter III, where the cluster is the smallest reproduction of the CuO_2 plane of high-Tc compounds. Hole density for each site and spin correlation between atomic orbitals are chiefly examined. In consequence no ferromagnetic coupling between apical oxygens and Cu atoms are observed, even though there are one tenth of the additional holes in the apical oxygens; the Hund rule coupling, which originates in the off-diagonal Coulomb interaction in Cu-$3d$, is not dominant. The fact is that the periodicity of the cluster prevents a sub-cluster in it — *the CuO_5 sub-cluster* — to have local $^3B_1$ hole configuration; point group at each sub-cluster is not a good quantum number any more, since inter-cluster hole transfer generates off-diagonal matrix elements between different representations of the group.

The result in chapter III was one of the motivation of the following study in chapter IV on XPS and XAS spectra of the d-p model. The subject was that how the spectra of the highly correlated system would be modified by the inter-cluster hole transfer. As a result of the valence hole relaxation, the main-peak of core-level spectrum is modified so that it has multiple peak structure on its high-energy side. The presence of $\left|\underline{c}d^{10}\underline{L}^2\right\rangle$ peak in Cu $2p$ XPS reflects the presence of the $\left|d^{10}\underline{L}^2\right\rangle$ local hole configuration in the initial state. A shift of the main peak with an increase of the valence hole density is observed,

which coincides with the experimental results. The valence band XPS and BIS spectra show that the free-Fermion like dispersion relation is still present although there is strong intra-atomic Coulomb repulsion. The position of each level is, however, different from that of the HF result.

The last two chapters were on the charge excitation gap of one-dimensional systems, which are described by Hubbard like Hamiltonians with inter-atomic Coulomb repulsion. We first calculated the gap of the d-p chain at quarter-filling as a function of intra- and inter-atomic Coulomb repulsion, and the charge transfer energy Δ. A new formula for E_{gap} was employed to reduce the size effect, and to clearly observe the gap as a function of intra- and inter-atomic Coulomb repulsion. It was shown that the inter-atomic repulsion enhances the charge excitation gap if there is finite Δ, but it cannot be the origin of the gap by itself; E_{gap} is very small when $\Delta \sim 0$. We next surveyed the gap of the extended Hubbard model in the parameter space, i.e., the $U - V$ plane. The inter-atomic Coulomb energy V directly creates the density fluctuation — the charge density wave — at half-filling. Finite size scaling was employed this time, to estimate the gap at thermodynamic limit. As a result, we obtain the gap which is nearly equal to zero at the phase boundary, unlike the classical limit or the Hartree-Fock result.

As we have studied through previous chapters, the diagonalization study gives us direct information about ground state energy, the ground state wave function, excitation spectrum, and also those of several low-lying states. There is, however, a major problem in the diagonalization study, i.e., the restriction of the system size in numerical diagonalization: the maximum size is about $N = 10 \sim 20$, as far as the lattice electron systems are concerned. The restriction chiefly comes from the capacity of contemporary computers. We have therefore block-diagonalized the Hamiltonian by hand before putting the Hamiltonian matrix into the computer as we have discussed in §2.4. Recently, applications of permutation group or quantum group are tried to reduce the matrix size for one-dimensional lattice electron or spin systems.[1,2] The limitation would be eased gradually with both the development in the programing and that in the computer architecture.

References

1. M. Ogata and H. Shiba: Phys. Rev. **B41** (1989) 2326.
2. R. Fye, M. Martins, D. J. Scalapino, J. Wagner, and W. Hanke (unpublished)

Acknowledgement

The author would like to express his sincere thanks to Prof. J. Kanamori for valuable suggestions and continuous encouragement throughout the study in Ph. D course, and the collaboration in early step of this work. He is also thankful to Dr. M. Kikuch for instructions on the art of computation in statistical physics and fruitful discussions. The author is happy to acknowledge Drs. Y. Akutsu, T. Jo, H. Akai and K. Hirai for precious comments on this manuscript. The author is grateful to Computation Center, Osaka University for their service on ACOS-S2020 and SX-2N. The present research was partially supported by Grants-in-Aid for Scientific Research of the Ministry of Education, Science and Culture.

Appendix

Charge Excitation Gap of Finite Size Systems

The charge excitation gap is the energy cost to add/remove an electron to/from the valence band. It is an essential quantity for the metal-insulator transition, since a system is insulating if the gap is finite. We discuss here about the details in definition of the gap that are used in chapter V.

The charge excitation gap E_{gap} of a macroscopic system is usually defined by a discontinuity in first derivatives of the ground state energy per site $\epsilon(n)$ with respect to electron density n†

$$E_{gap}(n) = \left.\frac{d\epsilon(x)}{dn}\right|_{x=n^+} - \left.\frac{d\epsilon(x)}{dn}\right|_{x=n^-}. \qquad (i)$$

The subject is how to discretize this formula to obtain E_{gap} of finite systems. The conventional definition of E_{gap}, when there are M electrons in a N-site system, is given by a naive discretization of eq. i,*

$$\begin{aligned} E_{gap} &\equiv (E_0[M+1] - E_0[M]) - (E_0[M] - E_0[M-1]) \\ &= E_0[M+1] - 2E_0[M] + E_0[M-1], \end{aligned} \qquad (ii)$$

where $E_0[M]$ is the ground state energy when there are M-electrons in the system. This definition has been widely used because of its simplicity.

The definition in eq. ii , however, has two problems. One is the ambiguity of the equation. If the number of up-spin electrons $N_\uparrow$ in the system is not the same as that of down-spin ones $N_\downarrow$, the $E_{gap}[M = N_\uparrow + N_\downarrow]$ depends on the spin of the added/removed electron. There are at least three plausible formula for the gap: (a) the E_{gap} which is obtained through adding or removing an up-spin electron as

$$E_{gap}[N_\uparrow, N_\downarrow] = E_0[N_\uparrow - 1, N_\downarrow] - 2E_0[N_\uparrow, N_\downarrow] + E_0[N_\uparrow + 1, N_\downarrow], \qquad (iii)$$

where $E_0[N_\uparrow, N_\downarrow]$ is the ground state energy when there are $M = N_\uparrow + N_\downarrow$ electrons in the system, (b) the E_{gap} which is defined by

$$\begin{aligned} E_{gap}[N_\uparrow, N_\downarrow] = &-2E_0[N_\uparrow, N_\downarrow] \\ &+ \frac{1}{2}E_0[N_\uparrow - 1, N_\downarrow] + \frac{1}{2}E_0[N_\uparrow + 1, N_\downarrow] \\ &+ \frac{1}{2}E_0[N_\uparrow, N_\downarrow - 1] + \frac{1}{2}E_0[N_\uparrow, N_\downarrow + 1], \end{aligned} \qquad (iv)$$

† for example, P. W. Anderson: Science **235** (1987) 1196.

* E. Lieb and F. Y. Wu: Phys. Rev. Lett. **20** (1968) 1445.

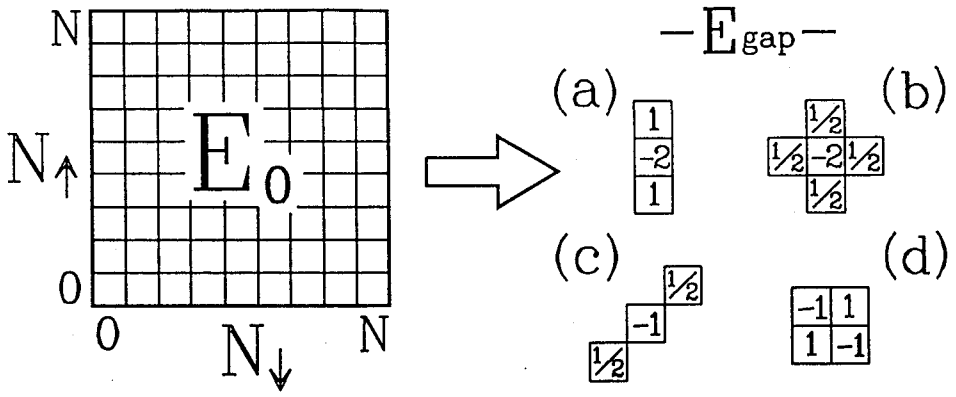

Fig. i. Two dimensional filters on the particle number space that give the charge excitation gap E_{gap} of N-site system. The cases **a**, **b**, **c** and **d** correspond to eqs. *iii*, *iv*, *v* and *vii*, respectively.

and (**c**) the E_{gap} which is defined by

$$E_{gap}[N_\uparrow, N_\downarrow] = \frac{1}{2}E_0[N_\uparrow - 1, N_\downarrow - 1] - E_0[N_\uparrow, N_\downarrow] + \frac{1}{2}E_0[N_\uparrow + 1, N_\downarrow + 1]. \qquad (v)$$

(Figs. 7.1 **a**, **b**, **c**) The other problem comes from the discreteness in energy level of finite size systems. Since both eqs. $iii \sim v$ also represent discretizations of

$$\frac{1}{N}\left.\frac{d^2\epsilon(x)}{dx^2}\right|_{x=n}, \qquad (vi)$$

they give finite values for E_{gap} as far as the one-particle density of state $\rho(n)$ of the system is not a constant of n, even though there is no Coulomb interaction. We cannot tell whether E_{gap} obtained by eq. $iii \sim v$ represent the charge excitation gap in eq. i, or the value vi. Since the term (vi) is not extensive, its contribution decreases with N. The contribution, however, is not negligible in actual calculations, where N is of the order of ten.

To avoid these problems and purely observe E_{gap} that comes from the electron correlations in a finite size system, the author proposes a new formula for the charge excitation gap

$$\begin{aligned} E_{gap}[N_\uparrow + 1/2, N_\downarrow + 1/2] = &- E_0[N_\uparrow + 1, N_\downarrow] + E_0[N_\uparrow + 1, N_\downarrow + 1] \\ &+ E_0[N_\uparrow \quad , N_\downarrow] - E_0[N_\uparrow \quad , N_\downarrow + 1]. \end{aligned} \qquad (vii)$$

The right hand side is, so to speak, a two-dimensional filter to $E_0[N_\uparrow, N_\downarrow]$ on the particle number space.(Fig. i **d**) *It is easy to show that* $E_{gap}[N_\uparrow + 1/2, N_\downarrow + 1/2]$ *is always zero if*

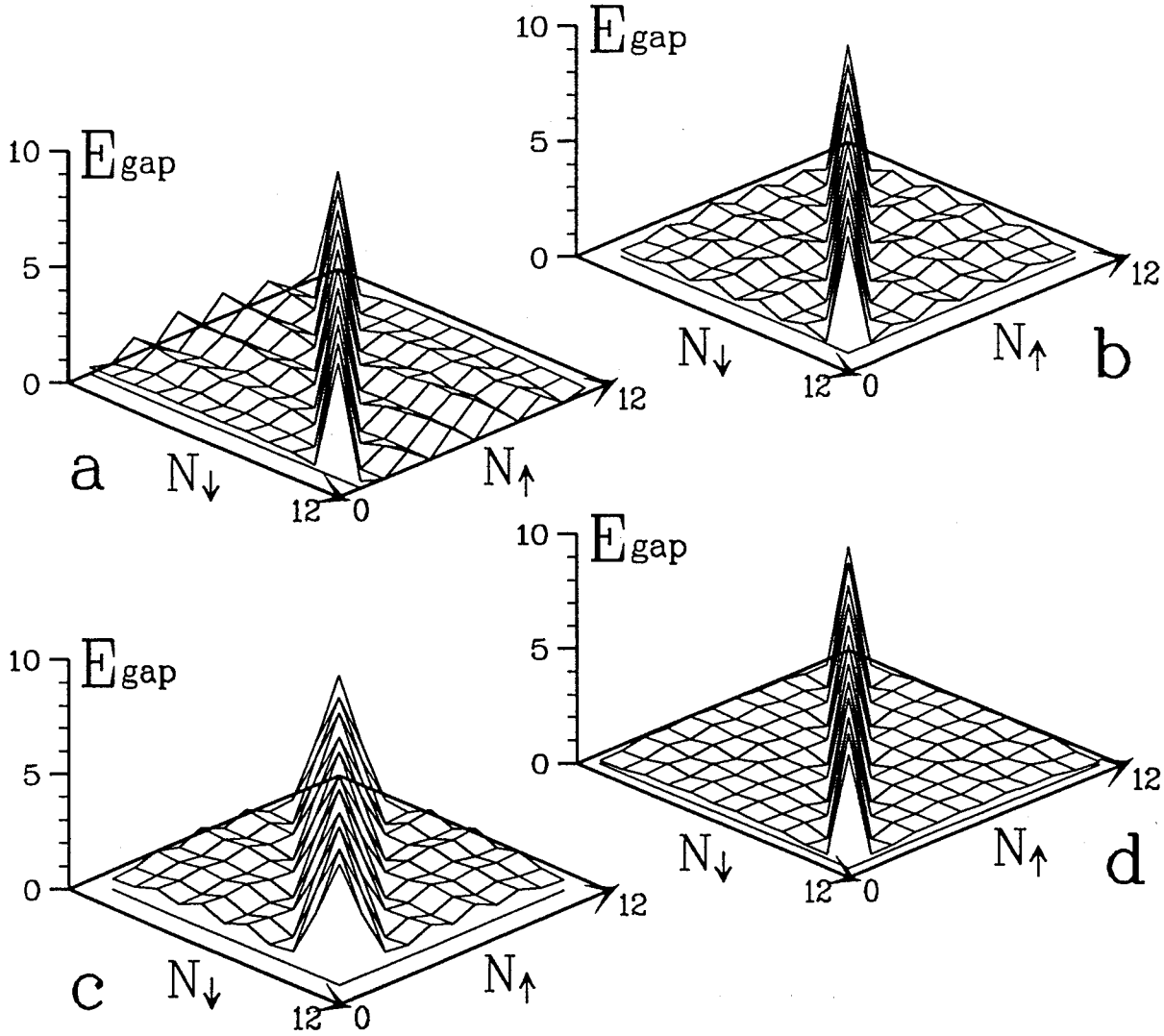

Fig. ii. The charge excitation gap of the 12-site Hubbard ring at $t = 1$ and $U = 8$ obtained by the filters **a** $\sim$ **d** in Fig. i. The case **d** shows the Hubbard gap most clearly.

there is no Coulomb interaction ($U_{ij} \equiv 0$); we can catch the effect of electron correlation from the 'noise' that purely comes from the discreteness of one-particle energy levels. Note that the filter (eq. vii) catches the charge excitation gap that originates in interactions between electrons, such as the Mott-Hubbard gap, the charge transfer gap and the BCS gap, etc., while it misses the band gap that comes from one-body potential. (The latter is of no interest, as far as the highly correlated system is concerned.) Many modifications of eq. vii are possible, but we would better use eq. vii, because it is the smallest filter for E_{gap} on the particle number space.

Now, let us examine how the *two-dimensional filter* (eq. vii) works for a typical model. Figure ii shows the E_{gap} of 12-site one-dimensional Hubbard model with periodic boundary

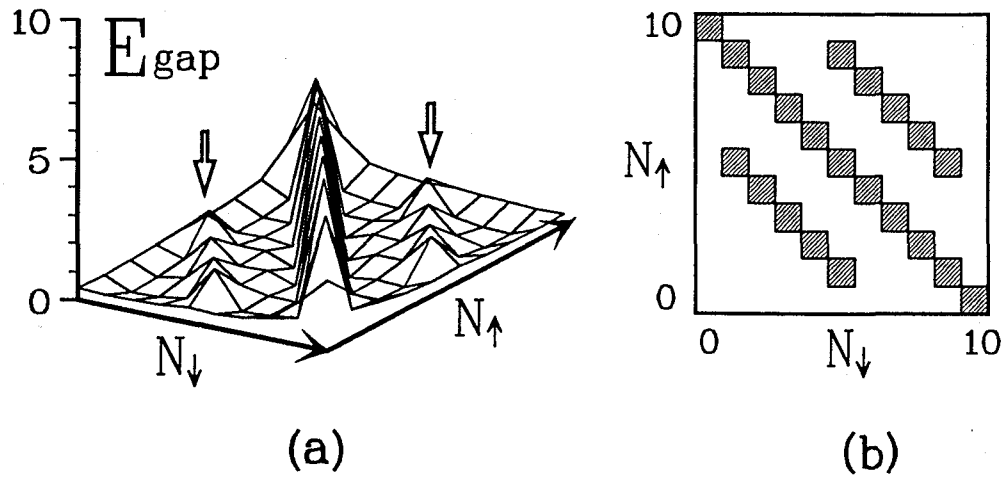

Fig. iii. The charge excitation gap of a two-dimensional 10-site Hubbard cluster at $t = 1$ and $U = 8$. (**a**) The E_{gap} obtained by eq. *vii*. (**b**) The E_{gap} is finite at the shaded position in the particle number space. There are rows of weak charge excitation gap at $N_\uparrow + N_\downarrow = 6$ and 14.

condition at $t = 1$ and $U = 8$ obtained by eqs. *iii*(**a**), *iv*(**b**), *v*(**c**) and *vii*.(**d**) It is obvious that the E_{gap} defined by eq. *vii* is free from the 'noise' away from half-filling compared with the cases **a** $\sim$ **c**. Since eq. *vii* gives zero as long as there is no electron correlation effect, it sometimes catches a weak charge excitation gap away from half-filling, the gap which originates in electron correlation effect in finite size systems. Figure vii **a** shows $E_{gap}[N_\uparrow + 1/2, N_\downarrow + 1/2]$ of the two-dimensional 10-site Hubbard model at $t = 1$ and $U = 8$. The Mott-Hubbard gap is present at $N_\uparrow + N_\downarrow = 10$. We also observe two weak rows of peaks at $N_\uparrow + N_\downarrow = 6$ and 14.(Fig. iii **b**) These two rows of the weak charge excitation gap come from the generalized Kondo coupling which have been proposed by Kusakabe and Aoki;† the electrons at the Fermi surface align its spin so as to reduce the intra-atomic Coulomb energy. The generalized Kondo coupling works most efficiently when there are 5, 14, 22, ..., electrons in the two dimensional lattice, thereby we observe the weak peaks at $N_\uparrow + N_\downarrow = 6$ and 14. (The weak singularity vanishes at the thermodynamic limit, $N \to \infty$.)

The expression in eq. *vii* is an example of the data processing for numerical data in multi-dimensional parameter space; we define the E_{gap} in two-dimensional particle number space, unlike the 'one-dimensional' analysis in eq. *ii*. Applications of such a multi-dimensional filter would be efficient for other physical observables, such as the spin susceptibility and the compressibility of the periodic systems.

† K. Kusakabe and H. Aoki: Phys. Rev. **B44** (1991) 7863.